Radiative Transfer and Chemistry in Spheroidal Interstellar Clouds

Philip Thomas O'neill

2001

Thesis submitted for the degree of PhD in Astronomy at
University College London.

(Supervisor: Professor D. A. Williams)

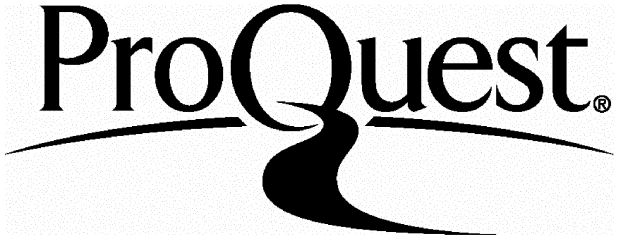

Abstract

The thesis begins by describing the way in which gas phase chemistry of the interstellar medium can be modelled, and demonstrating the potential significance of chemical reactions on the surfaces of dust grains present in the gas.

The dust also serves as the main shield against the interstellar ultraviolet continuum which influences the chemistry through photoionization and photodissociation reactions. The main part of this work involves the development of a method to evaluate radiative transfer into clumps in the diffuse interstellar medium and make use of such data for theoretical chemical models. The method handles clouds with axisymmetric shapes and therefore represents an improvement on previous techniques which model only plane-parallel clouds.

The radiation field within diffuse clouds with spheroidal shapes is calculated and used to model the gas phase chemistry which would occur in such clouds. These results are of interest partly by comparison with previous results for slab-shaped clouds: they demonstrate the viability and value of 2D models of the interstellar medium, particularly with regard to examining the dynamical collapse of gas clouds.

Finally, the possible influence of cloud shape on dust surface reaction rates is examined by calculating the grain charge distribution in the cloud models.

Contents

List of Tables

List of Figures

Introduction

Interstellar molecular clouds appear to be the main sites for star formation. From observations of CO emission—thought to trace the density of the interstellar medium (ISM)—Giant Molecular Clouds, which have masses ranging up to $\sim 10^6\,\mathrm{M}_\odot$, appear to consist of clumps of mass 10^3–$10^4\,\mathrm{M}_\odot$, and mean gas number density $n_\mathrm{H} \approx 10^2$–$10^3\,\mathrm{cm}^{-3}$. These clumps contain denser cores with $n_\mathrm{H} > 10^4\,\mathrm{cm}^{-3}$, mass $\sim 10\,\mathrm{M}_\odot$ and radius $\sim 0.1\,\mathrm{pc}$. The cores have temperatures around 10 K and can be mapped in rotational lines of species such as NH_3 or HC_3N, H_2CO or CS. They, in turn, are often seen to have further density structure, such as even more dense inner cores, and seem to be the formation sites of protostars.

For a typical clump, the Jeans Mass is only a few tens of $\mathrm{M}_\odot$. Above this mass, thermal pressure alone is insufficient to support the cloud against gravitational collapse. But if the clumps were collapsing on free-fall timescales then a rate of star formation much higher than observed would occur. There must therefore be some support mechanism other than thermal pressure. Turbulence and magnetic support have been suggested.

Maps of interstellar polarisation show that the directions of magnetic fields in the interstellar medium are well ordered over the size of the clouds. Magnetic fields provide a possible support mechanism through their influence on the charged components of the gas, and the level of order suggests that the support is not isotropic.

One popular view of how stars form is that, initially, the gravitationally unstable clouds collapse to form clumps which can be supported by the influence of magnetic fields. The clumps then evolve by ambipolar diffusion until they become magnetically supercritical and can collapse rapidly again.

Ambipolar diffusion is the process of neutral components slipping past the ions (atomic, molecular or charged grains) across the magnetic fields. The motion of ions and electrons across the field lines is resisted by the Lorentz force. Along the direction of the field lines it has been suggested that Alfvén waves can provide support to the gas.

Under these conditions the collapse of the clumps would be expected to occur axisymmetrically, and, as we will show later, the shape of the cloud as it collapses is likely to affect the chemistry within. We are interested in the gas phase chemistry of such clouds not only because of its importance in understanding observations, but also because it can itself affect the collapse process: both the rate of ambipolar diffusion and the level of support provided by Alfvén waves are partly determined by the ionization fraction of the gas.

Since the source of energy that maintains the ionization in clouds—at least in the early phases of collapse—is the interstellar UV radiation field we need to determine the transfer of radiation into such clouds. The spherical case is well known but we require a two-dimensional axisymmetric solution. In this study we will assume the general shape to be spheroidal, representative of a spherical cloud which collapses predominantly along one axis. A radiative transfer method for this purpose is the central tool that is developed in this thesis; it is intended to be sufficiently accurate to determine levels of ionization and other photochemistry in a complex chemical network, and yet not to be too time-consuming to implement alongside a major chemical calculation.

Chapter 1 contains a brief discussion of interstellar chemistry and several applications of conventional techniques (based on three original publications) that illustrate aspects of the chemistry in the interstellar medium; particularly the gas/dust interaction. The conventional methods of dealing with photochemistry are described, together with a more general technique for use in the new models, and the importance of the cloud shape is briefly discussed. The radiative transfer method developed here is described in Chapter 2 and the effects of dust and chemistry in spherical and slab clouds are described. In Chapter 3 we investigate the chemistry of clouds of spheroidal shape using the techniques developed in Chapter 2. Chapter 4 returns to the topic of the interstellar dust grains, briefly analysing the electronic charge of the grains in one and

two-dimensional clouds with the radiation transport and chemistry models developed here. Finally, the general conclusions of the work are summarized at the end of the thesis.

In brief, we will demonstrate: that a more general method of radiative transfer than is conventionally used is needed to determine the chemistry and ionization fraction in interstellar clouds (even in the case of 1D models); that appropriate methods of reasonable efficiency can be devised for the 2D case; and that the calculations reported here demonstrate the viability of comprehensive chemical/dynamical models of axisymmetric cloud collapse, though these are beyond the intended scope of the current work.

Chapter 1

Chemistry

In which the gas phase chemistry is introduced, with an example of how models can be used to test the limits of the chemistry. The possible role of dust grains in the chemistry is described, with a demonstration of the potential significance of surface reactions. The radiation-driven chemistry is discussed, and the shortcomings of current treatments with a description of a more general approach. Finally the influence of large scale structure is mentioned, highlighting the importance of a global approach to cloud modelling.

1.1 Introduction

One of the best ways we have of examining the conditions in the interstellar medium is through observations of gas phase species. The chemistry in a collapsing cloud is quite dynamic, the abundances of species varying as their environment changes, and the better we understand the chemistry which goes on in the cloud, the better we will be able to interpret our observations in terms of the actual physical conditions.

However, the chemistry is not just an innocent bystander in the process of star formation: molecules in the gas provide one of the major cooling mechanisms for the interstellar medium; and the ionization fraction of the gas helps determine its motion whenever magnetic fields are present.

In this work we will be concentrating on diffuse and translucent clouds in the interstellar medium. These are optically thin clouds, with at most a few magnitudes of visual extinction. The density of the regions is low, not more than a few thousand hydrogen-nuclei per cubic centimetre and they have low temperatures, around 10 K.

Mixed in with the gas is a population of dust grains. The dust is the major extinguisher of light in the medium and also acts as a heat source through ejection of electrons released by the photoelectric effect. Much about the dust is uncertain: its composition, the size distribution of the grains. Yet it may play a critical role in the chemistry of the medium.

1.1.1 Chemical models

The gas phase of clouds in the diffuse interstellar medium is characterized by very low densities and temperatures coupled with exposure to quite harsh radiation: ultraviolet and cosmic rays. Collisions between gas phase species may lead to chemical reaction, as can the absorption of radiation. Because of the low density we can ignore reactions involving more than two reactants since they will be extremely rare. Nonetheless, even the chemistry possible with only very small molecules requires knowledge of many different reactions before it can be modelled. There are several databases of astrochemical reactions in existence, such as the 'New Standard Model' and others of Bettens et al. (1995). The work here is based on the UMIST Astrochemistry Database (Millar et al. 1991, 1997) which provides a large set of several thousand one and two-body reactions with the parameters necessary to calculate their rates.

1.1.1.1 Types of reaction

Two-body reactions Most of the reactions in the UMIST database are for collisions between two atoms, molecules or ions. The rates of these reactions often have a temperature dependence which may be quite strong; for example, if there is an energy barrier for the reaction. Otherwise, the only dependence on the conditions in the cloud for these reactions comes through the densities of the reactants.

Radiation driven reactions There are three kinds of reactions where some kind of radiation impinges on an atom or molecule.

Firstly, there is ionization or dissociation by incident ultraviolet radiation from the interstellar radiation field. The rate of these reactions depend on the penetration of UV through the cloud and the cross-section of the affected species. These reactions are discussed in detail in Section 1.3.

Secondly, there is direct cosmic-ray ionization when an atom is struck directly by a cosmic ray. Cosmic rays penetrate easily through several magnitudes of visual extinction in the interstellar medium and so, for the clouds mentioned in the introduction, the rate for each reaction can be taken to be constant throughout the cloud. The reaction rate therefore depends only on the species cross-section and the external cosmic-ray incidence.

Finally, when H or H_2 is ionized by cosmic rays, energetic electrons can be released. These electrons mainly lose their energy by further interaction with hydrogen and release ultraviolet photons (800–1800Å) which can induce the same reactions as the interstellar UV mentioned above. However, in this case the radiation is generated from within the cloud, and because of the high penetration of cosmic rays is approximately equal throughout.

Interaction with dust grains If an interstellar cloud contains dust then the atoms and molecules in the gas will collide with grains.

The rate of collision will depend on the size and density distribution of the dust grains, which is unknown in general. However, there are constraints which can be used to test any assumed dust model. For example, the dust is supposed to be largely responsible for interstellar extinction so any viable dust model should reproduce the shape of the interstellar extinction curve (see Section 2.2).

The results of collision with dust are less certain. Most models assume that any molecule which collides with a dust grain has a probability of sticking near to unity. This means that, at the least, the dust component of the interstellar medium is gradually accreting species from the gas phase. Given a suitable dust model the rate of this process, known as *freeze out*, can be calculated. The UMIST97 database does not include

interactions with dust but it can be easily supplemented with a freeze-out reaction for each species (see Section 1.2.1).

But what happens to species that have frozen out onto the surface of dust grains? They may be released by some mechanisms, such as perhaps ultraviolet irradiation or cosmic-ray impacts. Or they may react with other frozen out species, particularly if they have any mobility over the grain surfaces. In particular, this is thought to be the main production method for H_2 in the interstellar medium (see below).

Unfortunately, very little is yet known about actual processes on the surface of interstellar dust grains; and any modelling of this aspect of the chemistry in interstellar clouds can only be tentative.

Formation of H_2 Gas phase reactions such as those listed in the UMIST rate file fall well short of producing the levels of molecular hydrogen observed in the interstellar medium. Given the importance of this molecule in any chemical model we include a special mechanism in all our models to convert atomic hydrogen into molecular form at a rate consistent with observations (Jura 1976). This addition represents the formation of H_2 by some unspecified mechanism on the surface of dust grains.

1.1.1.2 Computer models

The gas-phase reactions described above all have a rate which can be written in the form $k \cdot n(A)$ or $k \cdot n(A) \cdot n(B)$ for one or two body reactions, where $n(S)$ is the number density of species S, and the coefficient k depends on the reaction and local environmental conditions such as temperature.

The reaction rates only depend on each other through the abundances of their reactants, so we can represent the chemistry at a point in the interstellar medium as a set of ordinary differential equations in $n(S)$, which can then be solved numerically.

The computer models used in this work make use of the GEAR ODE-solving code developed by Hindmarsh (1972) to evaluate the chemistry at the point. The technique used is a time-dependent iterative model which, given the initial conditions (i.e. gas phase abundances), calculates the resulting abundances of the species at later times.

1.1.2 Environmental factors

We can, therefore, easily model the chemistry at a point in the interstellar medium provided we have a description of the physical conditions of the cloud at that point.

Let us recap the important local properties of the interstellar medium and how they affect reactions.

1.1.2.1 Density and Temperature

The gas density in the medium determines the absolute rate of all reactions. However, the density is of most significance for the two-body reactions because number density appears twice in the rate equation. The rate of a reaction between species A and B is

$$rate(A+B) = k_{AB} \cdot n(A) \cdot n(B) = k_{AB}[A][B] \cdot n_H^2, \tag{1.1}$$

where $[S]$ is the fractional abundance of species S, and n_H is the hydrogen nuclei number density. The rate coefficient, k_{AB}, for the reaction $A+B$ depends on the other properties of the environment, such as temperature. Thus an increase in density will 'speed up' the collisional chemistry relative to other reactions.

The temperature of the gas only affects the two-body reactions, however, the effect can be very strong. At low temperatures (say, $\lessapprox 100$ K) many reactions are irrelevant because their energy-barriers cannot be overcome.

1.1.2.2 Cosmic ray rate

The overall rate of cosmic-ray incidence to which the cloud is exposed determines the rate of direct atomic ionization by cosmic rays, and the rate of photoreactions caused by photons produced within the cloud as a result of cosmic ray absorption. Except at high optical depths the internal cosmic ray rate is approximately the same as that external to the cloud.

1.1.2.3 Background ultraviolet radiation

At any point within the cloud there will be a continuum UV field present originating from distant stars. The strength of this field determines the basic rate of photoreactions

within the cloud. In normal use of the UMIST database this factor is represented by the level of visual extinction (A_V) at the point.

1.1.2.4 Dust

Optical properties Dust grains within the cloud absorb and scatter ultraviolet light. At the local level, they affect the propagation of UV radiation produced within the cloud from cosmic-ray events. If there is a great deal of extinguishing dust then the generated photons will not affect gas chemistry so much as if dust is rare or has high albedo. To reflect this, the UMIST database recommends a scale factor of $1/(1-\omega)$ for cosmic-ray induced photoreactions, where ω is the albedo of the dust in the far ultraviolet where the induced emission spectrum is dominant.

Size distribution The size distribution of dust grains determines both the average cross-sectional area appropriate for calculating the gas-dust collision rate, and the grain surface area, which will be a major factor in any reactions between frozen-out species.

In addition, the size of a dust grain (along with its optical properties) determines the overall electric charge it is likely to have. This is discussed more fully in Section 4.1.3, and Chapter 4 generally. Here we merely note that the charge on the dust grain influences the rate of freeze-out for ions.

1.1.3 Water formation in dark interstellar clouds

This section provides a demonstration of how the chemical models may be used to test theories about conditions within the interstellar medium. The work reported in this section has already been published (O'neill & Williams 1999).

1.1.3.1 Water ice observations

Gas phase H_2O has been detected in a variety of warm circumstellar environments (van Dishoeck & Helmich 1996), but identification of gas-phase water in cold, dark interstellar clouds has been achieved only through maser emission, and abundance estimates remain unclear. Alternative observational approaches include studying the related species H_3O^+ and HDO. But neither method is without difficulty (Helmich et al.

1996). Observations made by the SWAS satellite indicate that the abundance of gas-phase H_2O is generally low. Typical upper limits for the H_2O fractional abundance in starless dark clouds are $< 10^{-7}$ (Bergin et al. 2000).

Therefore, the oxygen budget within dark interstellar clouds is not well understood. It seems likely from theoretical studies that the main carriers of oxygen in these regions are O, O_2, H_2O and CO.

Water in dark interstellar clouds can, however, be directly detected in the form of ice: there is an absorption feature at 3 μm which can be seen against an infrared source (Léger et al. 1979, Willner et al. 1982). On lines of sight through a dark cloud, the optical depth at 3 μm increases linearly with visual extinction (A_V) (Whittet et al. 1988, Chen & Graham 1993), and has a critical A_V below which the feature vanishes. In the case of the Taurus Molecular Cloud, the critical A_V is about 2.3 magnitudes (Smith et al. 1993).

1.1.3.2 Formation and destruction

Jones & Williams (1984) considered the formation of H_2O ice in the Taurus region. From the chemical abundances believed to be present in the gas phase, they inferred that the water ice was not deposited from water formed in the gas phase; the abundance of H_2O in the gas phase was much too low for direct freeze-out to form the observed ice within the lifetime of the cloud. They interpreted the existence of interstellar ice as evidence for surface chemistry, proposing that the ice must form directly on the surface of the dust by the hydrogenation of incident O-atoms. The hydrogenation process is required to have high efficiency, if the ice is to be deposited within a reasonable timescale.

Wagenblast & Williams (1996) inferred that below the critical A_V for ice onset this reaction may be injecting H_2O molecules into the gas phase where they contribute to the general interstellar chemical network.

Neglecting the possibility that the water or ice is produced elsewhere in the cloud and somehow transported into the line of sight: a possibility that requires very much more knowledge of the cloud to test; these conclusions seem reasonable. However, Bergin et al. (1998) have shown that repeated shocks within dark clouds may produce

enough H_2O in the gas phase to form the water ice mantles observed. This development warrants a re-examination of the case.

Cold gas phase production The main production route for H_2O at low temperatures is thought to be through the ion-molecule chemistry shown below:

$$\begin{aligned} H_2 \xrightarrow{crp} H_2^+ \xrightarrow{H_2} H_3^+ \xrightarrow{O} OH^+ \xrightarrow{H_2} H_2O^+ \xrightarrow{H_2} H_3O^+ \xrightarrow{e^-} \quad & H_2O + H, \\ \text{or} \quad & OH + H_2, \\ \text{or} \quad & OH + 2H, \\ \text{or} \quad & O + H + H_2. \end{aligned} \tag{1.2}$$

However, in recent years there has been some uncertainty over the branching fraction of the last step. Jones and Williams assumed that the fraction producing H_2O was 35%, the figure used in the 1996 version of the UMIST Astrochemistry Database (Millar et al. 1991, 1997). But two experimental studies of the branching ratios found conflicting results. Williams et al. (1996), using a flowing afterglow method, found the H_2O fraction to be only 0.05, so that the significance of gas-phase H_2O production would be much reduced. However, Vejby-Christensen et al. (1997), using a storage ring method, determined the H_2O fraction to be 0.33. The most recent version of the UMIST database (Le Teuff et al. 2000) now uses the 33% fraction reported by Vejby-Christensen et al. (1997). However, it may be worthwhile examining the difference in a chemical model.

Destruction of H_2O occurs mainly through reaction with ions, particularly C^+. Note that the ionization level and the C^+ abundance are most affected by the depth of the cloud.

Gas phase destruction reactions The limiting factors on the abundance of water in the gas phase are destruction in reactions with ions and photodestruction by ultraviolet radiation. Both these effects drop with increasing optical depth, so the region where H_2O will be most difficult to produce in the gas phase is that close to the critical A_V.

Formation on dust The possibility of formation of H_2O on dust is plausible. The efficiency of such a process is unknown, but, given the expected abundance of hydrogen on the grain surfaces it can certainly be imagined that an oxygen atom freezing-out might have a very high probability of reaction.

Shock enhancement The low-temperature chemistry does not appear to produce enough water in the gas phase to form observed ice mantles within the lifetime of the clouds. However, there are high temperature reactions which can help. In particular, the neutral reactions

$$O + H_2 \longrightarrow OH + H \quad \text{and} \quad OH + H_2 \longrightarrow H_2O + H, \tag{1.3}$$

have activation energies equivalent to 3160 K and 1660 K respectively. The passage of a shock through the gas can raise the temperature high enough to make these significant. Bergin et al. (1998) have shown that repeated shocks within dark clouds can maintain the H_2O abundance at a high enough level to allow ice deposition to arise from freeze-out on a timescale within the age of the clouds; thus the surface reactions invoked by Jones and Williams would not be needed.

However, Bergin et al. modelled the effect in a cloud with 20 mag of visual extinction. Will the shock method be sufficient at lower extinction levels, for example, close to the critical A_V?

1.1.3.3 Modelling the chemistry

Chemical models We model the gas chemistry in dark clouds using a single-point, chemical simulation. The reactions and rates used were those of the UMIST rate file (Millar et al. 1997) except where modified or supplemented. The rate file contains over 3800 reactions, for 394 molecular species, all of which were used. The effect of self-shielding on the photodissociation rate of CO was accounted for using software developed by Wagenblast (1992) according to the specification of van Dishoeck & Black (1988).

The models can be divided into classes according to the modifications made to the rates to obtain the reaction set used.

Species	Abundance		
He	0.07	Mg	3.0(-9)
C	1.0(-4)	Si	7.0(-9)
O	2.0(-4)	P	1.0(-9)
N	2.0(-5)	Cl	2.0(-9)
Na	2.0(-7)	Fe	2.0(-9)
S	2.0(-8)		

Table 1.1: Elemental abundances for the water-production models. The values are the fractional abundances relative to hydrogen nuclei, given in the form $a(\pm b) \Rightarrow a \times 10^{\pm b}$. H_2 had initial relative abundance of $1/2$, and the number density of hydrogen nuclei was 10^4 cm^{-3} for all models.

G0 The simplest case is that of the unmodified rate file. This includes the H_3O^+ dissociative recombination reactions roughly corresponding to the values measured by Vejby-Christensen et al., that is, the branching fraction producing H_2O is at 35%.

G1 The rate file is then modified to represent the branching fractions measured by Williams et al.: the reaction $H_3O^+ \xrightarrow{e^-} H_2O + H$ has its rate coefficient reduced from $3.5 \times 10^{-7}(T/300)^{-0.5}\,s^{-1}$ down to $0.5 \times 10^{-7}(T/300)\,s^{-1}$, where T is the temperature in Kelvin. Thus only 5% of the $H_3O^+ + e^-$ reactions form water in this model. The difference is made up by a new branch to $O + H + H_2$.

Both the reaction sets above are purely gas-phase reactions. We want to examine whether gas-phase mechanisms are sufficient to produce H_2O so we do not attempt to model the effects of interaction with the dust.

Cloud conditions All the models used a constant gas density of 10^4 hydrogen nuclei cm^{-3}. At the start of each simulation the gas phase was taken to consist solely of atoms and H_2 molecules. The relative abundances of the elements was as described in Table 1.1.

First we examine a point at a high optical depth (10 mag) to verify that we can reproduce the results of Bergin et al. (who modelled the gas phase with 20 mag of visual extinction). We then repeat the simulations for much lower optical depths. The critical visual extinction for water ice observation of 2.3 mag in Taurus corresponds to a maximum optical depth to a point of just 1.15 mag, which is the lowest we examine.

A particular model will be represented by the reaction set label with the level of A_V as a superscript; e.g., $G0^{1.15}$.

Shock effects The normal gas phase temperature of the models was 10 K. A C-type shock passing through a cloud produces a large increase in the gas temperature. Following Bergin et al. we simulate the effect of such a shock by raising the temperature in the model to 1000 K for a period of 100 years. As a small extension we also raise the density by a factor of four, although this does not alter the results for the species under consideration here.

1.1.3.4 Model results

Figures 1.1 and 1.2 illustrate the results of the shock for model G1 at each optical depth. In both cloud cases the H_2O abundance rises to expected levels and then gradually returns to the normal level.

The steady-state fractional abundances for each model/cloud are also presented in Table 1.2.

High optical depth At the higher optical depth, $A_V = 10$, a significant amount of water is produced in the gas phase. The steady state abundance of H_2O for $G0^{10}$ is around 2.7×10^{-6} per H-nucleus. Using the revised H_3O^+ dissociation reaction rates of Williams et al. gives a steady state fractional abundance of 2.5×10^{-7} for $G1^{10}$.

Neither of the water abundances computed above is high enough to form sufficiently deep ice mantles within the expected lifetime of the cloud. However, as in Bergin et al.'s model the imposition of a shock raises the fractional abundance of H_2O in $G0^{10}$ and $G1^{10}$ to around 10^{-4}, using up all the available oxygen. The increased abundance persists for a time on the order of a few 10^6 years after the shock and then decays to the low-temperature level over a similar period.

Figure 1.1 shows the abundances for model $G1^{10}$ in a three part graph using an expanded scale for the central section to show more clearly the effect of the shock. Note that the period of raised temperature only occupies a tiny part of the second segment. The reactions 1.3 drive the abundances to their high temperature levels almost immediately.

If shocks were to occur repeatedly, separated by a few million years the abundance of water in the gas phase would be maintained at the high level and therefore ice mantles could be built simply by freezing out this water onto dust grain surfaces, on a timescale well within the age of the cloud. This confirms the conclusion of Bergin et al., for the high A_V case.

Low optical depth The limit on the abundance of water is set by destruction in reactions with ions and photo-destruction by UV radiation. In particular, the ion C^+ is highly abundant in our models and is active in two destruction reactions with water:

$$C^+ + H_2O \longrightarrow HOC^+ + H, \text{ and} \tag{1.4}$$

$$C^+ + H_2O \longrightarrow HCO^+ + H. \tag{1.5}$$

At a hydrogen nuclei number density, n_H, of 10^4 cm^{-3} these reactions have a combined rate of $2.7 \times 10^{-1}[C^+][H_2O]$ cm^{-3} s^{-1} for destruction of H_2O, where $[A]$ represents the fractional abundance of species A. The dominant photo-destruction reaction of H_2O has a rate given by $5.9 \times 10^{-6} e^{-1.7 A_V} [H_2O]$ cm^{-3} s^{-1}. When the abundance of C^+ is high, as it is at very early times or low optical depth, these rates are comparable. In order for the abundance of H_2O to be large both rates need to be kept low. High visual extinction not only lowers the photo-destruction rate but also allows most of the carbon to form CO, greatly reducing the level of C^+. When the shock occurs, the C^+ used up in the above reactions with the extra H_2O is only replaced slowly.

At low visual extinction photoreactions are very efficient, not only at destroying H_2O but also at producing C^+. The levels of both H_2O and H_3O^+ remain very low, with a steady state fractional abundance of H_2O at $A_V = 1.15$ of only around 10^{-10}. Immediately after the shock, because much of the C^+ is consumed, the photo-destruction of water is more significant, but with little optical shielding the level of C^+ recovers quickly. Because the abundance of H_3O^+ is also low the effect of varying the H_3O^+ recombination branching fractions, models $G0^{1.15}$ and $G1^{1.15}$, is less significant.

Figure 1.2 is the equivalent of Figure 1.1 for model $G1^{1.15}$. In this model, as at $A_V = 10$, the temperature increase causes the abundance of H_2O to rise to a level where most of the available oxygen is used up in water. But this level is not nearly

	$A_V = 10$		$A_V = 1.15$	
	G0	G1	G0	G1
C^+	2(-9)	5(-9)	2(-6)	2(-6)
H_2O	3(-6)	2(-7)	2(-9)	3(-10)
H_3O^+	2(-10)	2(-10)	8(-12)	7(-12)
OH	1(-7)	1(-7)	8(-9)	6(-9)
O	7(-5)	9(-5)	1(-4)	1(-4)

Table 1.2: Steady State Abundances. The abundances given are the values reached after 10^8 years. Values are written $a(-b)$, meaning $a \times 10^{-b}$.

as long lived as at high optical depth. The low temperature chemistry takes less than 4500 years to reassert itself. This is not nearly long enough for H_2O to accumulate on the dust grains. At $A_V = 1.15$ mag the shocks would need to be unreasonably frequent to maintain the high abundance.

1.1.3.5 Conclusion

The low temperature model most favourable for producing gas-phase water—$G0^{10}$—predicts a fractional abundance of 2.7×10^{-6}. This is approximately the value Jones and Williams took as their estimate for gas of density $10^4\,cm^{-3}$. Consequently their conclusion applies here. At these abundances the time for ice mantles of the observed amount to form by freeze-out is $\approx 10^8$ years: longer than the expected lifetime of the cloud. The ice mantles could not therefore have formed simply by accreting H_2O molecules from the gas. Jones and Williams' suggestion was that the ice is formed by capturing O and OH molecules on the dust and reacting them on the surface with H to form H_2O ice *in situ*. Unless the gas-phase water abundance is significantly higher this conclusion will hold.

Bergin et al. have shown that increasing the temperature intermittently by the imposition of C-type shocks can raise the level of water abundance in the gas phase. However, their models assumed a visual extinction of twenty magnitudes, under which conditions the abundances take 10^5–10^6 years to return to the low temperature level. The $A_V = 10$ models used here give similar results for the effect of a shock. In $G0^{10}$ the relative abundance of H_2O is increased by around three orders of magnitude to a peak value of 10^{-4} after the shock, and this level is sustained for the order of 10^6 years. If the cloud were to be subjected to repeated shocks at a frequency roughly matching

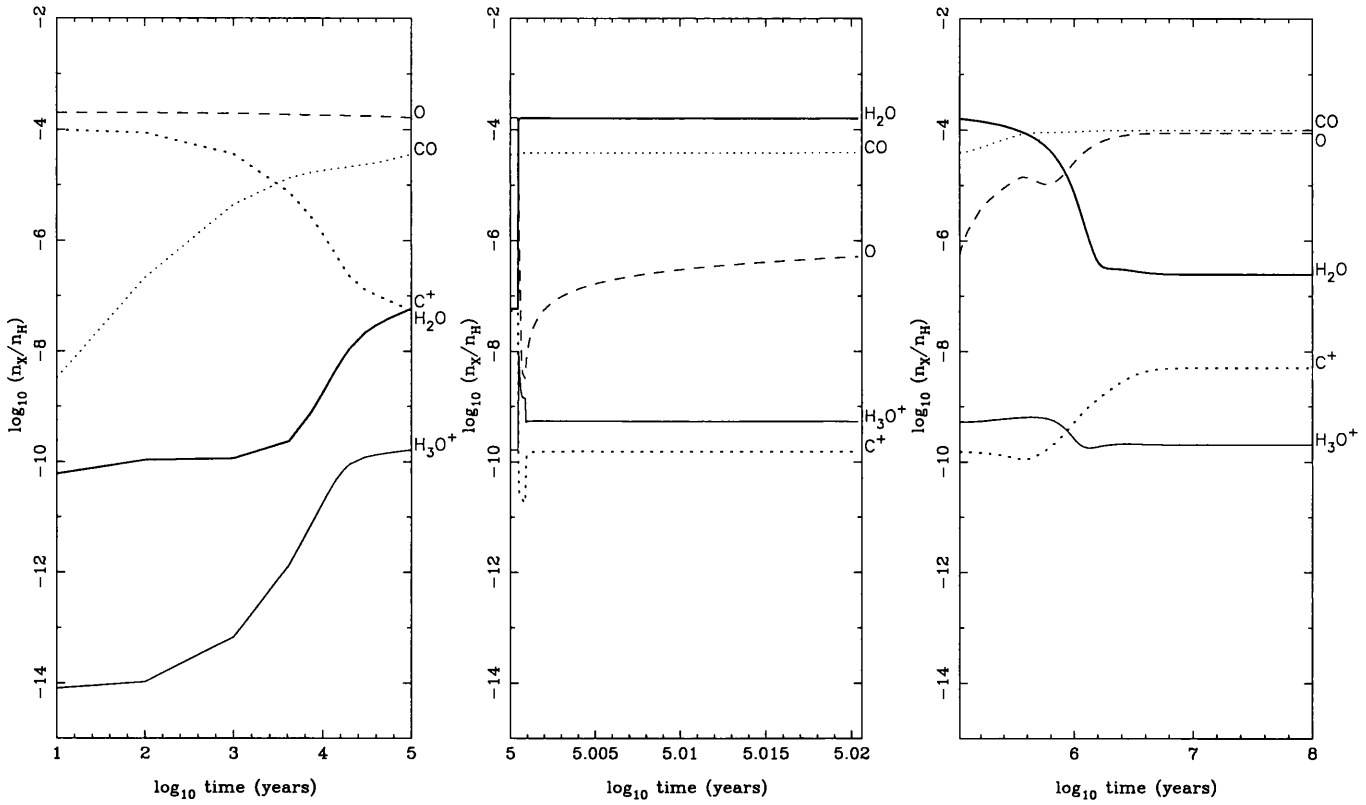

Figure 1.1: Model G1[10] with a 1000 K shock. The shock occurs just after 10^5 years and lasts for only 100 years. The high-temperature abundances persist for around a million years. The left-hand panel is the pre-shock phase, the centre panel shows the effect of the shock using an expanded scale for the x-axis, and the right-hand panel shows the post-shock development.

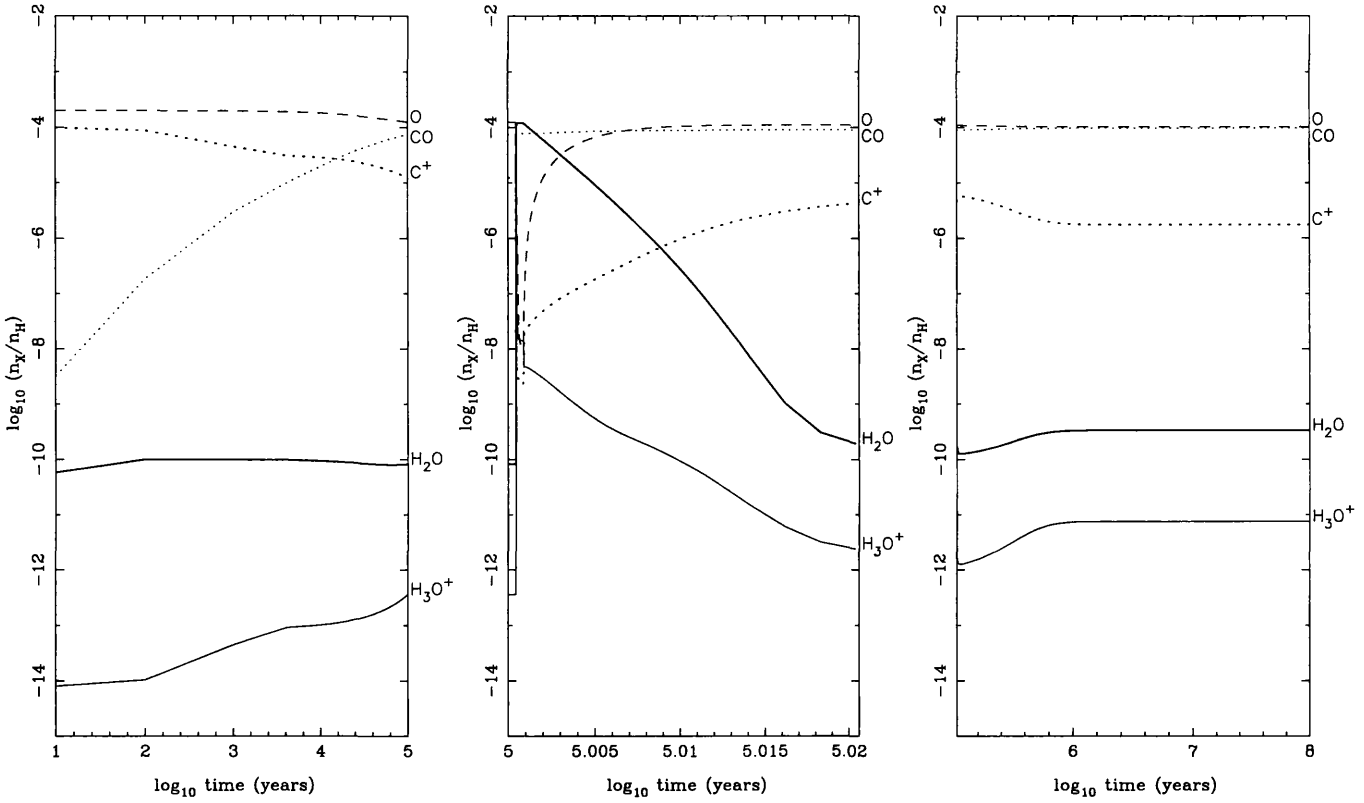

Figure 1.2: Model G1[1.15] with a 1000 K shock. With a low level of visual extinction the high-temperature abundances last for only a few thousand years. The left-hand panel is the pre-shock phase, the centre panel shows the effect of the shock using an expanded scale for the x-axis, and the right-hand panel shows the post-shock development.

the duration of their effects then the high gas-phase abundance of H_2O could be maintained. Bergin et al. also present estimates of shock distributions which indicate that this mechanism is plausible and thus could account for ice mantle formation in dark regions of clouds.

But there are two difficulties facing this as a general solution to the problem of water ice formation in molecular clouds. The first question is whether high optical depth regions with such as 20 mag of visual extinction are at all common. The interstellar medium appears to have density structure at all resolutions that have been observed. Clouds seem to be quite fragmented and have clumpy or filamentary structure. It has been suggested that molecular clouds may even have fractal structures (Dickman et al. 1990, Falgarone et al. 1991) and thus be highly irregular. It could be that regions with 20, or even 10 mag, of optical shielding are small or rare (Heyer et al. 1996, Alves et al. 1999) and the significance of their contribution to the chemistry of the interstellar medium needs to be carefully examined.

In any case water ice has been observed on lines of sight with low optical depth as well as high, and in this kind of environment shocks do not appear to be as effective in maintaining a high level of H_2O. Our models for $A_V = 1.15$ show that although a shock can convert most of the oxygen in the cloud to water the high ionization fraction in the gas returns the H_2O abundance to the low level in just a few thousand years. An A_V of 1.15 is supposed to correspond to a line of sight to a star with total optical depth 2.3 mag—the lowest level at which we might expect to detect the 3 μm water ice feature in Taurus. This is perhaps an extreme case but a model with $A_V = 2$—equivalent to the centre of a cloud with visual extinction 4 mag, well above the level at which water ice is observed—requires $\approx 10^4$ years for the post-shock abundances to return to the low temperature level. In fact, our models seem to indicate that an A_V of at least 6 is necessary before the high, post-shock, water abundance will last 10^6 years. That would imply a line of sight to a background source with 12 mag of visual extinction.

These results show that no reasonable frequency of shocks will maintain a high enough abundance of H_2O to form observed ice mantles at low visual extinctions. The conclusions of Jones and Williams still hold, therefore, for these regions at least:

the water ice on grain surfaces cannot be formed within the lifetime of clouds of A_V up to about 6 mag to an embedded object, or 12 mag to a background source, by the accretion of H_2O formed in the gas phase, either at low or high temperatures.

Circulation of material from high density cloud to lower density and lower extinction regions may, of course, provide a contribution to ice in such regions. This kind of dynamical model of interstellar clouds is outside the scope of the present work both in terms of modelling such chemistry, and in deducing what density structure and transport mechanisms would be appropriate.

1.2 Chemical effects of dust grains

1.2.1 Freeze-out rates

When particles in the gas phase collide with dust grains they can stick to the surface and be removed from the gas phase. The sticking efficiency is thought to be high (Leitch-Devlin & Williams (1985) suggest 0.1–1.0) for typical grain materials.

The rate of collision with a dust grain for a particle moving with velocity v is $\sigma v n_g$, where σ is the dust cross-section and n_g the dust grain number density. To find the overall rate of freeze-out for a species we should integrate over the range of velocities.

$$\dot{n} = -n n_g \int_0^\infty S \sigma v p(v)\, dv, \tag{1.6}$$

where n is the number density of the species under consideration, $p(v)$ is the velocity distribution, and S is the sticking efficiency. In general, S and σ can both depend on the velocity though S can generally be approximated to a constant.

We can estimate the rate more simply by replacing the integration with an expression in terms of the average particle velocity and average cross-section: $\dot{n} = -n n_g S \overline{\sigma} \overline{v}$. If $p(v)$ is the Maxwell distribution then $\overline{v} = \sqrt{8kT/\pi m}$, where m is the mass of the particle, k and T are the Boltzmann constant and gas temperature respectively.

From Spitzer (1978), and using again the approximation of considering an incident particle of average energy, we can take $\overline{\sigma} = \pi a^2 (1 - Ze U_g/kT)$ as the average cross-section for spherical grains with radius a and potential $U_g = Z_g e/a$. That expression holds when the unit charges of the ion and grain, Z and Z_g, have opposite sign. If the ion and grain charges have the same sign then the collision rate is very greatly reduced. We should then use, as Umebayashi & Nakano (1980), the expression: $\pi a^2 \exp(-ZeU_g/kT)$, which accounts for the proportion of ions with enough energy to overcome the electrostatic repulsion.

Evaluating constants in the appropriate units we obtain the equation quoted in

Rawlings et al. (1992). The rate per unit volume of freeze out of species x is:

$$\dot{n}(x) = 4.57 \times 10^4 \Gamma a^2 T^{1/2} C S_x m_x^{-1/2} n n(x) \quad \mathrm{cm^{-3}\,s^{-1}} \tag{1.7}$$

where m_x is now the mass in atomic mass units. The factor C, which represents electrostatic interaction between the species and the grain, is 1 for neutral species or grains. To summarize for ions with charge $+1$:

$$C = \begin{cases} 1 - \frac{Z_g e^2}{akT} = 1 - Z_g(16.71 \times 10^{-4}/aT) & \text{if } Z_g < 0, \\ \exp\left(-\frac{Z_g e^2}{akT}\right) = \exp(-16.71 \times 10^{-4} Z_g/aT) & \text{if } Z_g > 0. \end{cases} \tag{1.8}$$

Dust grains in a cloud are expected to have a distribution of charges with some grains positive and others neutral or negatively charged. However, we can simplify again and use the most common grain charge to determine the freeze-out rate. In cold, dark clouds the average grain charge is thought to be about -1 (Umebayashi & Nakano 1980) so C can be taken to be $1 + 16.71 \times 10^{-4}/aT$, resulting in a higher freeze-out rate for ions than for neutral species. In our models we assume a classical grain size of 10^{-5} cm and add freeze-out reactions for all species to our chemical models using the above prescription. Aside from the assumptions about the dust population the only environmental influences on the freeze-out rate for a species are the density and temperature.

The representation of the grain charge with a single average value seems a reasonable simplification; modelling freeze out would be very complex otherwise. But how generally valid is the choice of a charge of -1, and should it be constant throughout the model? In Chapter 4 we will test this assumption by examining the grain charge distribution in various cloud conditions. The efficiency of freeze out may prove to be very important in determining the gas phase chemistry, as we shall illustrate in the following sections.

1.2.2 Surface reactions

What happens to a molecule after it has frozen out onto the surface of a dust grain will depend on factors such as the nature of the dust material and the presence and mobility

of other molecules on the surface.

One molecule can come into contact with another on the surface of a dust grain either by direct collision on impact, where a molecule arrives on the surface at a point where another is situated, or by collision following sticking, where one or both molecules move over the surface until they come into contact with each other. Following a collision the molecules may react and one or more products may be ejected from the grain surface, or possibly be released later by some other mechanism. The surface reactions can thereby affect the gas phase chemistry to an extent determined by the efficiency of surface reactions and the likelihood of ejection.

Currently, the nature and efficiency of surface processes on interstellar dust is highly uncertain, as is the rate of release of frozen-out species. So proper modelling of chemistry on the dust is difficult. There are alternative grain models which extrapolate the traditional grain size distribution to include large numbers of very small grains. In such a case the small grains will dominate surface processes because they represent most of the available surface area. The effects could be quite different from the grain models used in this work, firstly because the smaller grains will tend to have a significantly different charge distribution (Weingartner & Draine 1999), altering not only the freeze-out rates but also possibly affecting the ionization balance between atoms and their corresponding ions (Lepp et al. 1988). And secondly, because the distribution of frozen-out species is less likely to be constant across all grains it may not be possible to model surface processes in a classical manner.

In the next section we present an example of how possible effects of surface chemistry may influence the gas phase. We examine the hypothesis that certain species colliding with grains undergo hydrogenation and are injected back into the gas phase. Thus the dust grains provide efficient hydrogenation channels for these species, which complement the gas phase chemistry. This is perhaps the simplest way in which gas phase chemical models can be expanded to incorporate surface chemistry. It illustrates how one can use models to explore the chemical reactivity of the dust.

1.2.3 Hydrogenation reactions on the surface of dust grains: a simple illustration

Diffuse and translucent clouds are the longest-studied of interstellar clouds, but their role in the evolution of matter in space is still unclear. Their relatively simple chemistry has led them to be identified as test-beds of chemical networks. This may be inappropriate, as they present difficulties (for example, the pathological case of CH^+; and the high observed abundance of CO) that have not currently been resolved. It seems evident that both the dynamics and the detailed pressure-density structure may be affecting the chemistry. In addition, uncertainties in some gas phase reactions remain, and the contribution of grain-surface reactions—indicated by both H_2 and NH—cannot yet be regarded as definitive, owing to limited experimental and theoretical support. However, this last point is being addressed in several studies (Vidali et al. 1999, Pirronello et al. 1999, Williams et al. 1999).

Recently, there has been a resurgence of interest in observations of diffuse and translucent clouds, and the list of identified molecular species has been significantly extended. Comprehensive lists of identified interstellar molecules are given in van Dishoeck (1998), Turner (2000) and Lucas & Liszt (1997). Even more recently, two new important species have been observed in the interstellar medium: CH_3 (Feuchtgruber et al. 2000) and C_3 (Maier et al. 2001, Haffner & Meyer 1995). Most of these new discoveries cannot be adequately accounted for on the basis of simple chemical models, and either more complex cloud structures (Nguyen et al. 2001) or additional chemical routes have been proposed.

In a paper already published (Viti et al. 2000) we explored the potential contribution of grain surface reactions to hydrocarbon formation in diffuse and translucent clouds as a supplement to the well-established gas phase networks. Hydrocarbons form in the gas phase via the following network (van Dishoeck 1998):

$$\begin{array}{ccccccc} C^+ & \xrightarrow{H_2} & CH_2^+ & \xrightarrow{H_2} & CH_3^+ & \xrightarrow{H_2} & CH_5^+ \\ & & \downarrow e^- & & \downarrow e^- & & \downarrow e^- \\ & & CH & & CH,\ CH_2 & & CH_3 \end{array} \qquad (1.9)$$

These routes involve two slow radiative associations of ions with H_2. The fractional abundance of carbon has been accurately determined (Snow & Witt 1996) to be 2×10^{-4} and for the network to reproduce the observed abundance of CH, nearly all of the carbon must be present in the gas as ions. Recent detailed models of the diffuse clouds towards ζ Oph and ξ Per (Wagenblast & Williams 1996) have been able to reproduce successfully many of the observed species on those lines of sight. But they require that the recombination coefficient of C^+ be lowered by at least a third from the canonical high temperature value. Nor do they include freeze out of carbon onto grains.

There may, however, be alternative routes for hydrocarbons to form, such as surface reactions. There is some evidence that surface reactions are important in producing the observed amount of NH; its observed abundance on several diffuse lines of sight can only be explained by assuming that some of the nitrogen that depletes onto grains is hydrogenated and released into the gas (Wagenblast et al. 1993, Crawford & Williams 1997). Models including oxygen hydrogenation on grain surfaces, forming OH or H_2O, have also been explored and shown to be viable (Wagenblast & Williams 1993, 1996). The question of the interaction of carbon with dust has not yet been addressed in this context. In diffuse clouds nearly all the available carbon at low visual extinction is photoionized, and chemical models of diffuse clouds have therefore generally assumed that carbon is not depleted on the dust. But there is also a class of grain models which assume that carbon is depleted in the form of hydrogenated amorphous carbon (HAC) mantles on silicate cores (Jones et al. 1990). In these models it is assumed that significant loss of carbon from the gas into HAC mantles occurs in diffuse clouds on a timescale of around 10 My. Thus extinction in these models becomes a time dependent property (Cecchi-Pestellini & Williams 1998). Diffuse cloud chemistry would also be, in this case, time-dependent on a similar timescale. On the other hand, it may be that carbon is fully hydrogenated on the surfaces of dust grains, and returned to the gas phase, as is implied by the NH observations. It is unclear, at present, which of these processes, if either, is occurring.

In Viti et al. (2000) we investigated the viability of diffuse and translucent cloud models in which carbon is either incorporated into HAC mantles or is returned to the gas phase as CH_4. The full discussion is not presented here but we include the corre-

sponding model results for comparison.

Another significant problem in diffuse cloud chemistry is the failure of models to account adequately for the abundant molecule CO (Wagenblast & Williams 1993). Gas phase formation routes to CO include C and C^+ with OH, O with CH, and HCO^+ with e^-. The formation route through the CH and O gas phase reaction is enhanced by the adoption of CH_4 injection from grains (Viti et al. 2000) but even in this case there still appears to be a shortfall in the computed CO abundance. Wagenblast & Williams (1996) suggested that an additional contribution from dust-formed OH and H_2O reacting with C^+ might resolve the difficulty. Hence it seems reasonable to extend the chemistry of Viti et al. (2000) to include the surface hydrogenation of other species on dust grains, and to explore the contribution of the product molecules to the gas phase network of reactions.

We have, therefore, included hydrogenation of O, N, S^+, CO to various products which then enter the gas phase network. These gas + grain chemistry models are explored for a variety of environments, ranging from rather low number density, low extinction clouds, to moderate density, moderate extinction clouds.

In the next section we describe the details of the models, including the adopted hydrogenation efficiency. The effects of the hydrogenation reactions are described in Section 1.2.3.2. The main results are given in the form of column densities integrated through the clouds in Sections 1.2.3.3 and 1.2.3.4 where we compare our models with some of the available observations. In Section 1.2.3.5 we briefly present our conclusions.

1.2.3.1 The Models

The basic chemical model which we use is the UMIST rate file (Millar et al. 1997). The initial elemental abundances by number density relative to hydrogen were taken to be as shown in Table 1.3. The values were taken from Snow & Witt (1996) though more recent estimates differ[1]. The adopted value of the cosmic ray ionization rate ζ, is $1.3\times10^{-17}\,s^{-1}$. For static slab model clouds with densities of each of 100, 300

[1]For example, Savage & Sembach (1996) gives abundances for Mg and Si more than two orders of magnitude different, although those changes in particular would not affect our results.

Species	Abundance		
He	0.07	S	1.3(-5)
C	1.1(-4)	Mg	3.0(-9)
N	6.0(-5)	Na	2.0(-7)
O	4.6(-4)	Si	7.0(-9)

Table 1.3: Elemental abundances relative to hydrogen nuclei for the chemical models including grain surface hydrogenation. Values are given in the form $a(\pm b)$ for $a \times 10^{\pm b}$.

and 1000 H-nuclei cm^{-3} we run time-dependent chemical multipoint calculations to find the gas phase abundances up to 10^7 years over a range of visual extinction from 0 to 4 mag. CO self-shielding is accounted for using codes developed by Wagenblast (1992).

We include freeze-out reactions for all species as described in Section 1.2.1 using a reduced grain surface area per unit volume such that about a third of heavy elements are depleted on to grains in a period of 10 My.

We compare results from eleven different chemistries: Models A and B are as mentioned in the previous section: Model A has no recovery of species from grains, and in Model B all positive carbon ions that meet the grain surfaces are re-injected into the gas phase as CH_4 molecules. The other chemical models that we used add extra hydrogenation reactions to Model B as described below. In all cases, the products of these surface reactions are assumed to be returned promptly to the gas phase.

Model C extends Model B by including the hydrogenation of oxygen and nitrogen: O forms H_2O on collision with a dust grain, and N forms NH_3.

Model D adds to Model C the hydrogenation of sulphur: S^+ is hydrogenated to H_2S on grains.

We also tested three models to examine consequences of the hydrogenation of CO. In Models E1 to E3 hydrogenation of CO into different species is added to the chemistry of Model C, that is, with C^+, O and N hydrogenation. In Model E1, CO forms H_2CO on grains, and in Model E2 the product is CH_3OH. Model E3 is a hybrid of E1 and E2 in which H_2CO and CH_3OH are formed equally. Models F1 to F3 are the same as E1 to E3 but with the hydrogenation of S^+ added as in Model D.

Finally, in addition to the above we have included results from a model using a chemistry identical to that of Model A (without any hydrogenation on grains) but in

Model	Surface Hydrogenation reactions
A	None (freeze-out of all species)
B	$C^+\downarrow \longrightarrow CH_4\uparrow$
C	As Model B but with $O\downarrow \longrightarrow H_2O\uparrow$, and $N\downarrow \longrightarrow NH_3\uparrow$ also
D	As C, with $S^+\downarrow \longrightarrow H_2S\uparrow$
E1	As C, with $CO\downarrow \longrightarrow H_2CO\uparrow$
E2	As C, with $CO\downarrow \longrightarrow CH_3OH\uparrow$
E3	As C, with 50% $CO\downarrow \longrightarrow H_2CO\uparrow$, 50% $CO\downarrow \longrightarrow CH_3OH\uparrow$
F1	As D, with $CO\downarrow \longrightarrow H_2CO\uparrow$
F2	As D, with $CO\downarrow \longrightarrow CH_3OH\uparrow$
F3	As D, with 50% $CO\downarrow \longrightarrow H_2CO\uparrow$, 50% $CO\downarrow \longrightarrow CH_3OH\uparrow$
Z	Purely gas-phase chemistry (as A) with no grain interaction

Table 1.4: Summary of hydrogenation reactions on grain surfaces included in each chemical model.

which species do not freeze out on to dust grains. We call this Model Z and it is provided as a reference to show the situation where dust grains do not interact chemically with the gas phase. The hydrogenation reactions added in each model are summarized in Table 1.4.

1.2.3.2 Effects of the hydrogenation reactions

The changes in computed abundances with the addition of new grain-surface reactions are essentially as expected. Release of molecules from grains to the gas phase will necessarily cause an increase in abundance for all species based on the elements released. This is simply because an element that was being removed from the gas phase in Model A is still present. If there is an ejection mechanism for one hydrogenated species (as in Model B), then it seems logical to expect ejection of some kind for other hydrogenated species; the real question is the form of the ejection reactions and their relative efficiencies. Unfortunately, not enough is yet known about activity on the grains to set accurate *a priori* rates; and current observational data are probably not extensive enough to make detailed studies of such complex systems. Hence, we introduce ejection reactions for only a few species at a time, each with 100% efficiency: this efficiency may be unrealistic, but at this stage we are only interested in studying the qualitative effects of surface grain chemistry on the evolution of diffuse and translucent clouds in order to answer the following question: would the abundances of hydrogenated species vary enough to produce a detectable difference? By introducing

a 100% efficiency of ejection, we are, of course, allowing for the largest possible effect.

We have calculated the abundances for visual extinctions from 0 to 4 mags for clouds of density 100, 300 and 1000 cm^{-3}. This enables us to consider the chemistry in several regimes including diffuse clouds with density $\leq 300\,cm^{-3}$ and $A_V \approx 1$ mag, and translucent clouds with higher density and $A_V \approx 3$ mag. Tables 1.5, 1.6 and 1.7 summarize our results; they contain column densities for the clouds after a time of 10^7 years—there is no steady state for models with freeze-out. The last column shows the observed column densities of ζ Per (in Table 1.5) and ζ Oph (in Table 1.6) taken from the literature; for some species these were not available in which cases we have listed the column densities derived along different lines of sight (more details can be found in the captions). Even when available, we have not included error bars in listing the observed values, as comparisons between observations and our model results should only be done in qualitative terms. Note that the column densities of Models A and B may differ from the ones listed in Viti et al. (2000) because we have incorporated a better treatment of CO self-shielding and a more accurate estimation of the integrated column densities.

Here we review in qualitative terms the consequences of introducing surface hydrogenation. Adding hydrogenation reactions for C^+ increases the abundances of many small hydrocarbons. The effect is most pronounced in the diffuse cloud case where most of the carbon is ionized and so most susceptible to freeze-out. In Model C, where we have added hydrogenation for oxygen and nitrogen, there is an equivalent set of changes for species containing these elements. Of particular interest are the H_2O and CO abundances which are related because H_2O and OH are thought to be part of a major formation route for CO. The introduction of surface hydrogenation for C^+ (Model B) increases the amount of CH_2 present, which reacts with oxygen to produce CO. The column density of CO is thereby greatly increased (compared to Model A), but the column densities of H_2O and OH in Model B fall compared to Model A: this is a consequence of the increase in carbon-bearing species in the gas. With the addition of surface hydrogenation of oxygen directly into H_2O the former C:O ratio is maintained and the column densities of H_2O and OH are recovered to approximately the levels of Model A.

The addition of surface hydrogenation of nitrogen to NH_3 in Model C affects directly the abundance of NH_3, increasing it well above the level of Models A and B.

With the inclusion of sulphur hydrogenation to H_2S in Model D, the column densities of S and S^+ are increased for all cloud densities. For the diffuse clouds these are the only significant effects. However, at the translucent cloud density of $1000\,cm^{-3}$ several species, including CS, SO and H_2S, have column densities increased by several orders of magnitude.

The differences between Models E1, E2 and E3 are negligible. The only species whose column density changes significantly between them is CH_3OH. It seems that H_2CO can be adequately produced from CH_3OH in the gas phase so there is no real need to consider these models (or F1–F3) separately. In the tables of results therefore we have only included Models E3 and F3 which both produce CH_3OH and H_2CO in equal amounts from CO. Probably the most interesting thing to observe with these models is that they do not decrease the column density of CO; indeed, in the translucent cloud case it is increased even further beyond that of Model C, probably a consequence of the increase of the carbon budget in the gas due to the ejection and dissociation of CH_3OH and H_2CO. Also in the translucent cloud models the amount of CO_2 is increased and we can see an increase in the column densities of H_2CO and CH_3OH themselves. The hydrogenation of CO makes no appreciable difference in the diffuse cloud regime.

Model Z, without freeze-out, naturally differs most from Model A in which all species suffer freeze-out with no ejection. One of the main effects of the postulated hydrogenation and ejection mechanism is simply avoiding depletion of elements from the gas phase. This restores to models other than A more of the characteristics of Model Z. However, it is thought that ions and molecules which meet the surface of a dust grain will stick to it, making Model Z seem unphysical. We hope that the differences between this model and others due to hydrogenation rather than the simple release of frozen species (notably CH_3 and NH at low densities and H_2S and NH_3 at $1000\,cm^{-3}$) may offer some support for ejection from grains as a result of chemical reactions on the surface.

1.2.3.3 Comparisons with observations: diffuse clouds

We choose to compare results of selected species from models of number densities of $100\,cm^{-3}$ (Table 1.5, close to the ζ Per number density) and $300\,cm^{-3}$ (Table 1.6, close to the ζ Oph number density) with observations of diffuse clouds. Many of the species in the tables have been selected because they have been observed towards the lines of sight of ζ Per, ζ Oph and other diffuse clouds. We have taken into consideration as many relevant observational studies as possible, although for a more comprehensive summary we refer the reader to several recent reviews: van Dishoeck (1998) where recent results on both diffuse and translucent clouds are presented; and Lucas & Liszt (1997) who present comprehensive observations of diffuse clouds. The relation of our results to observations is discussed below.

Hydrocarbons A full discussion of hydrocarbon chemistry and the effects of C^+ hydrogenation on grains was given in Viti et al. (2000). The main observation-related result is for CH. Wagenblast & Williams (1993) give the column density for diffuse clouds as $2.5 \times 10^{13}\,cm^{-2}$, which all our models except Model A match well. Without release of carbon from dust mantles the column density of CH falls short by at least two orders of magnitude. The introduction of hydrogenation reactions for oxygen and CO may also affect the abundances of hydrocarbons.

Lucas & Liszt (2000) have detected absorption lines of C_2H and C_3H_2 along many lines of sight. From Table 1.6 it is obvious that purely gas phase low temperature models cannot account for the detection of these species. Viti et al. (2000) concluded that surface hydrogenation and ejection of hydrogenated species from the grains may be necessary to account for hydrocarbon abundances. In fact, Model B fails to meet the Lucas & Liszt column densities by less than one order of magnitude in the case of C_2H and about one order of magnitude for C_3H_2. These discrepancies could easily be due to the low gas density adopted for models in Table 1.6. At a gas density of $1000\,cm^{-3}$ our column density matches extremely well with the abundances measured by Lucas & Liszt (2000) (Table 1.7). Model A, where no hydrogenation and ejection occurs is clearly inadequate, regardless of the cloud density; note that van Dishoeck & Black (1986) have succeeded in reproducing the lower limit of the observed column densities

Species	Model							Observation	
	A	B	C	D	E3	F3	Z	ζ Per	
H	1.7(20)	1.7(20)	1.7(20)	1.7(20)	1.7(20)	1.7(20)	1.7(20)	8.9(20)–1.4(21)[f]	–
H_2	7.2(20)	7.2(20)	7.2(20)	7.2(20)	7.2(20)	7.2(20)	7.2(20)	3.2(20)–7.1(20)[f]	–
S	6.4(11)	5.0(12)	5.0(12)	6.0(13)	5.0(12)	6.0(13)	5.9(13)	1.8(13)[a]	–
S^+	2.0(15)	2.0(15)	2.0(15)	2.1(16)	2.0(15)	2.1(16)	2.1(16)	1.6(16)[b]	–
CS	8.0(7)	5.3(9)	5.3(9)	6.7(10)	5.3(9)	6.7(10)	2.4(10)	–	1(12)–1(13)[c]
SO	1.5(7)	1.5(7)	1.9(7)	1.7(9)	1.9(7)	1.7(9)	2.0(8)	–	1(12)–1(13)[c]
CO	8.5(11)	1.5(13)	3.1(13)	3.0(13)	3.1(13)	3.0(13)	1.1(13)	6.1(14)[a]	2(14) – –1(16)[c]
C_2H	1.4(8)	8.3(11)	8.3(11)	8.0(11)	8.3(11)	8.0(11)	1.0(11)	–	–
C_3H_2	5.2(4)	2.0(9)	2.0(9)	1.7(9)	2.0(9)	1.7(9)	1.8(8)	–	–
C_2H_2	3.2(6)	3.2(10)	3.2(10)	3.2(10)	3.2(10)	3.2(10)	2.9(8)	–	–
CH	2.3(11)	1.3(13)	1.2(13)	1.2(13)	1.2(13)	1.2(13)	9.3(12)	–	–
CH_3	4.2(9)	1.4(12)	1.4(12)	1.4(12)	1.4(12)	1.4(12)	1.9(10)	–	–
CH_4	3.8(3)	5.3(12)	5.3(12)	5.3(12)	5.3(12)	5.3(12)	7.7(4)	–	–
H_2CO	5.2(7)	1.3(10)	1.6(10)	1.6(10)	1.6(10)	1.6(10)	2.4(8)	–	–
NH	1.4(10)	9.2(9)	3.1(11)	3.1(11)	3.1(11)	3.1(11)	1.1(10)	1(12)[d]	–
CN	3.1(8)	7.7(9)	6.8(10)	6.7(10)	6.8(10)	6.7(10)	5.2(9)	3.0(12)[e]	–
OH	1.0(13)	9.9(11)	3.9(12)	3.8(12)	3.9(12)	3.8(12)	1.1(12)	4.0(13)[e]	–
H_3^+	3.8(13)	4.5(12)	4.5(12)	4.1(12)	4.5(12)	4.1(12)	4.0(12)	–	–
C_3	2.5(4)	2.9(9)	2.9(9)	2.7(9)	2.9(9)	2.7(9)	2.9(8)	–	–

[a] Snow (1977)
[b] Snow et al. (1987)
[c] Lucas & Liszt (1997)
[d] Meyer & Roth (1991)
[e] Felenbok & Roueff (1996)
[f] Savage et al. (1977)

Table 1.5: Results of chemical models for 1 mag of visual extinction for clouds with number density of $100\,cm^{-3}$ after 10^7 years. The computed column densities (in cm^{-2}) of each species from seven models are compared to the observed column densities for ζ Per taken from the literature; when observations of this cloud were not available, we have taken the values for other clouds of similar densities (along various lines of sight). (Note, numbers in the form $a(b)$ above represent $a \times 10^b$.)

Species	Model							Observation			
	A	B	C	D	E3	F3	Z	ζ Oph	Extragalactic	Sag A*	Cyg OB2
H	5.5(19)	6.0(19)	6.1(19)	6.0(19)	6.1(19)	6.0(19)	5.9(19)	5.2(20)[n]	–	–	–
H_2	7.7(20)	7.7(20)	7.7(20)	7.7(20)	7.7(20)	7.7(20)	7.7(20)	2.9(20)[n]	–	6(22)[f]	–
S	6.8(9)	1.0(11)	1.0(11)	1.3(14)	1.0(11)	1.3(14)	1.3(14)	8.5(13)[a]	–	–	–
S^+	1.7(13)	1.8(13)	1.8(13)	2.1(16)	1.8(13)	2.1(16)	2.1(16)	1.2(16)[a]	–	–	–
CS	3.1(3)	5.1(8)	5.0(8)	6.1(11)	5.0(8)	6.1(11)	2.0(11)	7(11)–5(12)[b]	–	–	–
SO	7.1(5)	7.3(5)	1.3(6)	1.2(10)	1.3(6)	1.2(10)	1.4(9)	–	1(12)–1(13)[c]	–	–
CO	1.9(9)	6.0(13)	2.2(14)	2.1(14)	2.2(14)	2.1(14)	6.9(13)	1.72(15)[d]	–	–	3(16)[l]
C_2H	4.6(2)	5.0(12)	4.9(12)	4.6(12)	4.9(12)	4.6(12)	5.9(11)	–	7(12)[e]	–	–
C_3H_2	3.5(-4)	3.3(10)	3.2(10)	2.6(10)	3.2(10)	2.6(10)	2.7(9)	–	4.8(12)[e]	–	–
C_2H_2	1.8(1)	2.3(11)	2.3(11)	2.2(11)	2.3(11)	2.2(11)	2.1(9)	–	–	5.5(14)[f]	–
CH	3.3(8)	3.1(13)	3.1(13)	3.0(13)	3.1(13)	3.0(13)	2.4(13)	–	–	–	–
CH_3	1.6(7)	2.9(12)	2.8(12)	2.8(12)	2.8(12)	2.8(12)	4.6(10)	–	–	8(14)[f]	–
CH_4	4.3(1)	1.4(13)	1.4(13)	1.4(13)	1.4(13)	1.4(13)	6.0(5)	–	–	–	–
H_2CO	4.0(5)	4.7(10)	8.0(10)	7.9(10)	8.1(10)	8.0(10)	1.4(9)	–	–	–	–
NH	9.7(9)	5.3(9)	6.5(11)	6.5(11)	6.5(11)	6.5(11)	8.8(9)	8.8(11)[g]	–	–	–
CN	7.4(5)	3.9(10)	4.2(11)	4.0(11)	4.2(11)	4.0(11)	2.8(10)	3(12)[h]	–	–	–
OH	1.7(13)	6.8(11)	6.9(12)	6.7(12)	6.9(12)	6.7(12)	1.0(12)	4.8(13)[i]	–	–	–
H_3^+	3.3(13)	1.8(12)	1.8(12)	1.6(12)	1.8(12)	1.6(12)	1.5(12)	–	–	–	3.8(14)[l]
C_3	1.5(-4)	4.9(10)	4.8(10)	4.2(10)	4.8(10)	4.3(10)	4.5(9)	1.6(12)[m]	–	–	–

[a] Morton (1975)
[b] Drdla et al. (1989)
[c] Lucas & Liszt (1997)
[d] Lambert et al. (1994)
[e] Lucas & Liszt (2000)
[f] Feuchtgruber et al. (2000)
[g] Crawford & Williams (1997)
[h] Lambert et al. (1990)
[i] Chaffee & Lutz (1977)
[l] Geballe et al. (1999)
[m] Maier et al. (2001)
[n] Savage et al. (1977)

Table 1.6: Results of chemical models for 1 mag of visual extinction for clouds with density of $300\,cm^{-3}$ after 10^7 years. The computed column densities (in cm^{-2}) of each species from seven models are compared to the observed column density for ζ Oph taken from the literature. When observations of this cloud were not available, we have taken the values for other clouds of similar densities (lines of sight towards various extragalactic sources, Cygnus OB2 and the galactic centre—Sagittarius A*).

of C_2H and C_3H (and other hydrocarbons in general) without invoking grain surface reactions: however their models do not include depletion of gas phase species on to the grain, a process which is now believed to occur in some degree (Williams 1998).

CH_4 itself is not observable, but we could test the hypothesis that CH_4 is made and released on grains by detecting its products formed in the gas phase. CH_3 is the most direct product and, recently, Feuchtgruber et al. (2000) detected CH_3 towards the Galactic Centre and deduced a column density of $(8.0\pm2.4)\times10^{14}$ cm^{-2}. Our models fail to match the observed value by at least one order of magnitude (see Tables 1.5, 1.6 and 1.7). However, we note firstly that the gas density along the line of sight observed by Feuchtgruber et al. (2000) is believed to be $> 1000\,\mathrm{cm}^{-3}$: comparisons of Tables 1.5, 1.6 and 1.7 indicate that CH_3 column density increases proportionally to the gas density. Secondly, if no hydrogenation and ejection is included (i.e. Model A), the basic ion-molecule gas-phase chemistry networks cannot account for the formation of any of the CH_3 detected. Even without any freeze-out (Model Z) the predicted column density is nearly two orders of magnitude below those of models with hydrogenation of oxygen.

Carbon Monoxide Surface hydrogenation of C^+ in Model B indirectly yields an increase in CO over Model A of more than 30% but the computed column density is still more than one order of magnitude less than that observed for ζ Oph (note, however, that this line of sight has an unusually high CO column density, and may not be typical).

Table 1.6 shows a clear increase in column density from Model B to Model C, where oxygen and nitrogen can hydrogenate on grains. Although CO is still under-abundant by at least half an order of magnitude with respect to the CO observed in that line of sight, the results suggest that if freeze-out occurs some release from the surface must occur. A somewhat higher diffuse cloud density would improve the match between Model C values and that of ζ Oph.

Sulphur-bearing species Atomic and ionized sulphur have been observed along the line to sight of ζ Per (Snow 1977, Snow et al. 1987) and ξ Per (Smith et al. 1991). The column density of neutral sulphur is estimated to be approximately 1.8×10^{13} cm^{-2} by Snow (1977) and slightly lower (7.24–$9.55\times10^{12}\,\mathrm{cm}^{-2}$) by Smith et al. (1991). More

significant is the ratio of N(C)/N(S), given by the latter as $\sim$ 80, significantly larger than previous work (Gomez-Gonzalez & Lequeux 1975). As the number densities of ζ Per and ξ Per are close to 100 cm^{-3}(Wagenblast et al. 1993, Smith et al. 1991), we compare these observations with Table 1.5. Models B and C are close to the lower limit while Model D is above the upper limit by a factor of $\sim$ 4. However if we compare the N(C)/N(S) ratio, Models D and Z both give a ratio of 30, underestimating the observed value (Smith et al. 1991), though close to the older value $\sim$ 32 found by Gomez-Gonzalez & Lequeux (1975). By contrast, in models where ionized sulphur is frozen out the ratio is $\sim$ 340, much larger than observed, suggesting that sulphur is not being retained on the grains in these clouds.

Ionized sulphur is observed to be $\approx 1.6 \times 10^{16}$ cm^{-2} (Snow 1977, Snow et al. 1987), three orders of magnitude larger than neutral sulphur. This ratio is roughly consistent with our Models B, C and D. As expected, the S^+/S ratio does not vary among models, since grain hydrogenation and ejection of ionized sulphur would increase the total sulphur budget in the gas phase. However, the observed ionized sulphur column density is well matched by Model D as well as Model Z.

Drdla et al. (1989) have searched the CS J=2-1 emission line in 10 diffuse molecular clouds and successfully detected it in four of the clouds, including ζ Oph. They derive the total CS column densities from one line by means of statistical equilibrium calculations and they found that the CS column density varied from $\sim 2\times10^{12}$ to 3×10^{13} cm^{-2}. Turner (2000) reports an observed fractional abundance of 3.8×10^{-9} which corresponds to a column density of $\sim 10^{12}$ cm^{-2} (for $A_V \sim 1$ mag). Lucas & Liszt (1997) also detected molecular absorption of CS and SO, among other species, in front of extragalactic millimetre wavelength radio sources and find column densities for both species between 10^{12} and 10^{13} cm^{-2}. From Tables 1.5 and 1.6 one can see that CS is only formed in significant amounts when sulphur depletion occurs. In Model D for densities of at least of 300 cm^{-3}, CS reaches the lower limit of the observed abundances. In general we find that our models underestimate the abundance of CS in the diffuse medium although Model D is very close to the observed lower limit. A slightly higher density than that used for Table 1.6 would improve the agreement.

We conclude from the analysis of sulphur-bearing species that models with grain

surface reactions involving the hydrogenation of sulphur are favoured over those models with freeze-out. However, in the diffuse cloud case, there is little to distinguish them over a model without freeze-out.

Nitrogen-bearing species Among the nitrogen-bearing species, we discuss NH and CN. NH was first detected by Meyer & Roth (1991) towards ζ Per and HD 27778 and found to have a column density of $\sim 10^{12}\,\mathrm{cm}^{-2}$. More recently, Crawford & Williams (1997) estimated its column density towards ζ Oph from much higher resolution data to be $\sim 8.8 \times 10^{11}\,\mathrm{cm}^{-2}$. Lambert et al. (1990) reported a column density of CN towards ζ Oph of $\sim 3 \times 10^{12}\,\mathrm{cm}^{-2}$. NH is very well reproduced by models where nitrogen hydrogenation and ejection occur. CN, on the other hand, is under-produced by almost one order of magnitude, although, again, in the models where no hydrogenation occurs CN cannot be formed in the gas phase in detectable quantities. Note that previous models, such as the ones by Wagenblast & Williams (1993), produce much higher CN abundance than we do in Model A: this is because their models do not include depletion of the gas phase on to the grains. Our equivalent model without depletion (Model Z), though better than Model A, is still worse than models with hydrogenation at predicting NH and CN abundances in diffuse clouds.

OH and H_3^+ Chaffee & Lutz (1977) detected OH towards ζ Oph and report a column density of $\sim 4.8 \times 10^{13}\,\mathrm{cm}^{-2}$. Geballe et al. (1999) detected H_3^+ for the first time in diffuse interstellar clouds (towards Cygnus OB2) and they found a high column density of $\sim 3.8 \times 10^{14}\,\mathrm{cm}^{-2}$. Computed abundances for both species are greater (and closer to observations) in models where freeze-out without ejection of hydrogenated species occurs, i.e. in Model A, although in the case of OH from Table 1.5 (where the density is supposed to be representative of ζ Oph), there is less than half an order of magnitude difference between Model A (very close to observations) and Model C or E3. The fact that OH and H_3^+ are more abundant when freeze-out occurs without hydrogenation and ejection is not surprising as ions are extremely reactive and they are readily removed when hydrogenated species such as water are abundant in the gas. In fact, we note that in Model A more than 50% of the OH is produced via dissociative recombination of H_3O^+ while in the other models this route only accounts for $\sim$ 10% of the OH

present. This may be the cause for the difference between a model where only freeze-out occurs and one where freeze-out plus hydrogenation and ejection occurs. H_3O^+ is easily destroyed by species such as HCN and HNC: these are more than two orders of magnitude larger in models where hydrogenation occurs than in Model A.

Compared to the observed value, H_3^+ is under-abundant in all our models. Note however that the Geballe et al. (1999) detection of H_3^+ was towards Cygnus OB2, at a visual extinction of $\sim$ 10 mag: comparing Tables 1.6 and 1.7, we note that H_3^+ increases by over one order of magnitude when going from A_V of 1 to 3 mags: this should not be due to a density increase because comparison of Tables 1.5 and 1.6 (same A_V but different density) show that H_3^+ decreases with density (in fact Geballe et al. (1999) note that H_3^+ column density is not proportional to the column densities of other species). We infer that a model where the density is kept to $\sim 300\ cm^{-3}$ and $A_V = 10$ mags may give the observed column density even for models where hydrogenation and ejection occurs.

Another factor which may explain the discrepancy between the computed OH and H_3^+ abundances and the observed values is the cosmic ray ionization rate, ζ. The abundances of both these species are directly related to ζ through their dependence on H_2^+ which is formed by ionization of H_2 by cosmic rays. H_2^+ reacts with H_2 to form H_3^+ directly, and OH is formed by dissociative recombination of H_3O^+ which is the product of H_2^+ and H_2O. In our models ζ is taken to be $1.3 \times 10^{-17}\ s^{-1}$ but in diffuse clouds a value of ζ between $10^{-17}\ s^{-1}$ and $10^{-16}\ s^{-1}$ is plausible (van Dishoeck 1998). If ζ were increased by half an order of magnitude in our models the computed abundances could be brought close to those observed.

C_3 Haffner & Meyer (1995) reported a tentative detection of C_3 towards HD147889. More recently Maier et al. (2001) observed C_3 in diffuse interstellar clouds along the lines of sight towards three stars, including ζ Oph, and inferred a column density for C_3 of 1.0–2.0 $\times\ 10^{12}\ cm^{-2}$. C_3 is one of only two bare carbon species detected in diffuse clouds and it is a potential carrier for the Diffuse Interstellar Bands (Maier et al. 2001). Our diffuse clouds models (see Tables 1.5 and 1.6) do not reproduce the high column density observed. However, hydrogenation of C^+ (Models B–F) does offer

some improvement over models with no freeze-out or no ejection.

1.2.3.4 Comparisons with observations: translucent clouds

Many species have been observed in translucent clouds (Turner 2000, van Dishoeck 1998). Here, we select some observational results in order to compare with our models. The discussion on hydrocarbons below is brief because the main differences for such molecules are between Models A and B, and they were the subject of our earlier paper (Viti et al. 2000). For a more comprehensive summary of observations we refer the reader once again to the review of van Dishoeck (1998), and to Turner (2000), who summarizes the results of a large observational study of translucent clouds;

Hydrocarbons As in the diffuse cloud case, Model A cannot account for the column densities of CH, C_3H_2 or C_2H. Jannuzi et al. (1988) reported a column density of 4.6×10^{13} cm^{-2} for CH through a translucent cloud. All the models with hydrogenation produce columns slightly higher than this value. For C_3H_2 and C_2H, as shown in Table 1.7, the hydrogenation reactions raise column densities by over an order of magnitude (nearly two orders for C_2H) but there is still a significant shortfall for Models C–F which include hydrogenation reactions other than just C^+. A more detailed discussion for these species is given in Viti et al. (2000).

None of our Models A–D, nor Model Z, produce methanol in the quantities that are observed. Turner (1998) has suggested that methanol may form by energetic processing of CO ice (by UV and cosmic-rays) on grains, followed by photo-desorption. In addition there is some experimental work examining the conversion of CO to CH_3OH (Hudson & Moore 1999).

Models E2, E3, F2 and F3 include, at either 50 or 100% efficiency, a surface reaction producing methanol from CO sticking on grains. There is, of course, an increase in column density over other models. In fact, even Models E3 and F3, where only 50% of hydrogenated CO produces methanol, produce a column density which is an order of magnitude higher than observed. Thus if CO is indeed hydrogenated on grains the efficiency required would be only a few percent in order to reproduce observations.

Species	Model							Observation
	A	B	C	D	E3	F3	Z	
H	7.7(18)	1.8(19)	1.9(19)	1.8(19)	1.9(19)	1.8(19)	1.6(19)	–
H_2	2.4(21)	2.4(21)	2.4(21)	2.4(21)	2.4(21)	2.4(21)	2.4(21)	$\sim$ 3(21)
CS	1.4(5)	4.9(5)	2.1(7)	1.8(13)	2.7(7)	2.2(13)	2.7(13)	3.3(13)[a]
SO	2.7(5)	5.8(4)	3.1(8)	1.6(13)	1.8(8)	1.7(13)	2.0(12)	9.6(13)[a]
H_2S	1.0(3)	2.2(2)	1.6(5)	3.2(13)	1.1(5)	3.2(13)	4.7(9)	7.5(13)[a]
NH_3	5.3(11)	2.2(11)	2.3(13)	1.9(13)	2.1(13)	1.8(13)	9.8(9)	3–6(13)[a, b]
N_2H^+	5.9(10)	2.8(10)	4.1(11)	7.2(9)	2.3(11)	5.3(9)	8.7(8)	3(12)[a]
HCN	7.3(10)	1.0(11)	3.5(11)	3.3(11)	5.1(11)	5.2(11)	5.3(10)	1.1(14)[a]
HNC	1.0(11)	9.7(10)	1.5(12)	1.4(12)	1.5(12)	1.5(12)	3.5(10)	7.5(12)[a]
CH_3OH	4.4(9)	2.7(9)	1.1(10)	1.3(9)	3.2(13)	2.5(13)	1.6(8)	1.8(13)[c]
CO	8.3(15)	3.4(16)	8.0(16)	6.6(16)	2.9(17)	2.5(17)	2.2(17)	1(16)–1(17)[d]
H_3^+	1.6(14)	3.0(13)	3.4(13)	1.1(13)	2.8(13)	9.9(12)	5.7(12)	–
C_2H	4.1(11)	9.1(13)	2.8(13)	2.1(13)	3.0(13)	2.4(13)	6.2(12)	1.98(14)[e]
C_3H_2	9.3(9)	4.4(12)	6.0(11)	3.5(11)	6.3(11)	4.3(11)	1.1(11)	3(12)[f]
CH	2.2(12)	1.6(14)	9.5(13)	8.8(13)	9.7(13)	9.5(13)	1.3(14)	–
CH_3	1.6(12)	1.4(13)	6.6(12)	5.8(12)	1.1(13)	9.6(12)	3.4(11)	–
CH_4	8.2(10)	1.2(14)	5.6(13)	5.0(13)	5.7(13)	5.5(13)	2.8(9)	–
H_2CO	8.8(11)	1.8(12)	1.7(12)	9.5(11)	4.3(13)	2.8(13)	1.9(11)	–
C_3	4.1(9)	3.3(12)	6.4(11)	4.6(11)	7.4(11)	5.8(11)	1.8(11)	–

[a] Turner (2000)
[b] Turner (1995*a*)
[c] Turner (1998)
[d] van Dishoeck et al. (1991)
[e] Turner et al. (1999)
[f] Cox et al. (1988)

Table 1.7: Results of chemical models for 3 mag of visual extinction for clouds with density of $1000\,cm^{-3}$ after 10^7 years. The computed column densities (in cm^{-2}) of each species from seven models are compared to column densities for translucent clouds taken from the literature. With the exception of the column densities from van Dishoeck et al. (1991) the observational values presented are determined from fractional abundances averaged over a variety of translucent clouds, and assuming a gas column density around 3×10^{21}.

Sulphur-bearing species At densities of the order of $1000\,cm^{-3}$, the column density of many sulphur-bearing species increases when ionized sulphur is hydrogenated on the grains (Models D and F). The most significant feature of the results is that these species should not be detectable if sulphur freezes out as in Models A to C. But sulphur-bearing species have been observed extensively in translucent clouds. For example, Turner (1995*b*, 1996*b*,*a*) conducted a survey in a standard sample of 11 Cirrus cores and 27 Clement-Barvainis translucent objects. Table 6 in Turner (1996*a*) summarizes his sulphur studies by listing the ratios of sulphur-bearing species abundances in all the observed sources. He divides his objects between Cirrus and Clemens-Barvainis (CB) cores and finds CS/SO = 0.056–0.196, and H_2S/SO = 0.21–0.982 for the Cirrus cores; whereas CS/SO = 0.047–0.478, and H_2S/SO = 0.263–3.4 for the CB objects (note that the observed column densities listed in Table 1.7 for CS, SO and H_2S are taken from Table 1 in Turner (2000)). The H_2S/CS ratios vary between 1.10 and 34.5. From Model D we have: $CS/SO = 0.3$, $H_2S/SO = 0.65$ and $H_2S/CS = 2.1$. Our CS/SO ratio is within the observational values for the CB objects and H_2S/SO and H_2S/CS are between the (somewhat loose) limits given by the observations. Our conclusion for sulphur is that since these species are widely detected in translucent clouds, surface hydrogenation (or ejection of some kind) is occurring. Note that grain surface has been invoked by Turner (1996*a*) in order to explain observed sulphur bearing species (e.g H_2S). The improved match of Model D to observations of SO and especially H_2S over Model Z suggests that hydrogenation and ejection may be preferable to ejection without surface reaction.

Nitrogen-bearing species For translucent clouds, we find that all nitrogen-bearing species in Model C increase by 1–2 orders of magnitude compared to Model B. For example, the fractional abundance of NH_3 at $A_v = 3$ mag is 7.65×10^{-10} for Model B and 1×10^{-8} for Model C, and it slightly decreases in Model D. Turner (1995*a*) has found a fractional abundance of $\sim$ 1-2$\times 10^{-8}$ which, assuming $A_v = 3$ mag, corresponds to a column density $\sim$ 3-6$\times 10^{13}$ cm^{-2}. Model C results are in agreement with this measurement. Turner (2000) reports a fractional abundance for N_2H^+ of $\sim 10^{-9}$ which, assuming $A_V = 3$ mags, corresponds to a column density of $\sim 3\times 10^{12}$ cm^{-2}.

The model which predicts the closest match to the observations is Model C: in this model gas phase NH_3, and therefore most of the nitrogen-bearing species in the gas, are enhanced with respect to Models A and B; however Model D (where gas phase NH_3 is enhanced as well) predicts a much lower N_2H^+ column density than even Model A and B (where N freezes and remains on the grains); this is probably due to the fact that in Model D gas phase H_2S, and eventually neutral sulphur are enhanced and the reaction with sulphur is the main route of destruction for N_2H^+.

HCN column density is reported to be at least $\sim 6 \times 10^{11}$ cm^{-2} by Liszt & Lucas (1994). Models E3 and F3 are in very good agreement with this lower limit. These models have a rich chemistry due to the hydrogenation of nitrogen, carbon, oxygen and CO on grains. A puzzling result is, however, the variation of HNC/HCN ratio among models. In fact, the increase of this ratio may be misleading: HCN appears not to increase when nitrogen is hydrogenated on the grains and as a consequence, HCN/HNC in models where hydrogenation of nitrogen occurs is much less than unity, a result which is not supported by observations. Indeed, Turner et al. (1997) find the ratio HCN/HNC to be "significantly above unity in translucent clouds". Both HCN and HNC fractional abundances do indeed increase when nitrogen is hydrogenated and released from grains but while HCN is efficiently destroyed, HNC remains constant. The observational result of Turner et al. (1997) therefore suggests that the UMIST95 rate file, which we have used, may not contain all the possible destruction routes for HNC. Indeed the new UMIST99 database (Le Teuff et al. 2000) does add new reactions for HNC.

1.2.3.5 Conclusions

Models such as our Model A which include depletion of species onto grains but no ejection fall well short of reproducing observed column densities for several molecules. It is clear, for instance, that the incorporation of much of the C^+ arriving on grains into HAC mantles is not viable since insufficient amounts of CH can then be produced. If the C^+ is hydrogenated and released in some form then the effect may be tested through observations of species such as C_3H_2, C_2H and CH_3.

If C^+ can be hydrogenated and ejected from the surface of grains, then a similar

process may well exist for other elements such as nitrogen, oxygen and sulphur. In a hydrogen rich environment it seems likely that such elements, when frozen out, will become hydrogenated (Jones & Williams 1984).

Here we have explored the possible consequences of introducing dust-based hydrogenation mechanisms into our gas-phase chemical models. We have taken the view that atoms, atomic ions and CO may either be retained at the surface, or be hydrogenated and ejected into the gas phase. We have also briefly compared with results obtained assuming freeze-out does not occur (equivalent to immediate ejection without any surface reactions).

The results for both low density diffuse and translucent clouds show that hydrogenation and ejection from the surface of grains does improve the reproduction of observed values for some species. In particular, the re-release of oxygen into the gas phase does help bring the predicted CO column density of our models closer to the observed values in diffuse clouds. Models B-F can not predict H_3^+ high column density observed in diffuse clouds, although we believe that this is due to the low visual extinction adopted in the models.

For translucent clouds differences among models appear to be even more significant. Observations of sulphur-bearing species seem to suggest that this element must avoid depletion in some way, and ejection following a hydrogenation reaction matches observation better than simply avoiding freeze-out. Our models including hydrogenation of CO suggest that this may be a good formation route for methanol and a suitable choice of efficiency could easily match observation. These models (and indeed all others) still maintain the CO column density within observed limits. One contradictory result is the inversion of the HCN/HNC ratio when nitrogen is hydrogenated. This may have arisen because the UMIST95 rate file may not include all possible destruction routes for HNC.

Overall the outlook for these kinds of mechanisms is favourable. Given correct knowledge of rates and products they may help to explain some observed trends or features. Theoretical and experimental studies of surface processes and interactions are clearly needed in order to understand more fully the chemistry of diffuse and translucent clouds.

1.3 Chemical effects of radiation

If a molecule or atom absorbs an ultraviolet photon it enters an excited state and may then become ionized or dissociate. The probability that a species in a particular state will absorb a photon of a given energy is represented by the species *cross-section* which can be determined through a variety of laboratory techniques. However, values determined in the laboratory then need to be extrapolated to the very low temperatures and densities found in the interstellar medium. The number of photons of a given energy that will be incident is represented by the *intensity* of the UV field at that wavelength.

Thus the total rate, k, for a photoreaction (in s^{-1}) from absorption of continuum ultraviolet is given by:

$$k = \sum_i x_i \int \sigma_i(\lambda) I(\lambda)\, d\lambda. \tag{1.10}$$

Where $\sigma_i(\lambda)$ is the effective cross-section at wavelength λ for state i to result in the reaction, and x_i is the fractional abundance of the species which is currently in state i. $I(\lambda)$ is the mean (angle-averaged) intensity incident. If we measure cross-sections in cm^2 then intensity, I, is in photons cm^{-2} steradians^{-1} s^{-1}Å^{-1}.

We will simplify considerations by assuming that the cross-sections σ_i represent the sum over end states (from i) which lead to the reaction. Furthermore, in future discussions we will assume that the population distribution x_i can be combined with the cross-sections for each state to give the total cross-section, $\sigma = \sum_i x_i \sigma_i$. Thus we will consider that photoreactions in the regions of the interstellar medium under consideration follow the simplified rate equation:

$$k = \int \sigma(\lambda) I(\lambda)\, d\lambda. \tag{1.11}$$

1.3.1 Calculating photoreaction rates

As described above, the rate of photoreactions depends on the cross-sections of the species and the incident ultraviolet intensity. The cross-sections of many species can be measured or derived theoretically, but the ultraviolet intensity present within the interstellar medium is not precisely known.

1.3.1.1 Background radiation field

Near to a star, of course the overall field will be dominated by the output of that source. However, we consider the general case of a field immersed in an isotropic background field due to all stars. This field has a cut-off at 912Å because of absorption by atomic hydrogen, which puts a hard lower limit on the integral in Equation 1.11.

Several attempts have been made to estimate the background field, including Gondhalekar et al. (1980) and Draine (1978). These are based on observations made in various directions from the solar neighbourhood.

Using such an estimate the rate of a photoreaction can be calculated in the unshielded interstellar medium. But to know the rates within a gas cloud in the interstellar medium requires knowledge of how the background field propagates through the cloud.

1.3.1.2 Radiation field within a gas cloud

Line radiation Of the species in the UMIST database only CO and H_2 are dissociated through the absorption of line radiation. This means that they ought to be treated differently from all the other species whose photoreactions depend on the continuum UV field because a CO molecule near the surface of a cloud which absorbs a photon is protecting CO molecules deeper in the cloud. This ability of these species to 'self-shield' means they cannot accurately be modelled just using a single point in the cloud. We will discuss this problem more in Section 2.3.

Continuum radiation Although atoms and molecules may absorb particular lines, the attenuation of the continuum radiation field is performed by the dust which is present in the gas.

Dust grains in the interstellar medium absorb and scatter light as it passes through. The amount of attenuation on a line of sight depends on the size distribution of the dust grains, their composition (and shape) and the density. Since these may vary on different lines of sight, the calculation of the radiation field at even a single point in a cloud is, in general, a three-dimensional radiative-transfer problem involving many assumptions about the dust and the density structure of the cloud.

1.3.2 Photoreaction rates in the UMIST rate file

The UMIST rate file would not be nearly such a useful tool as it has been if the important photoreactions could only be handled by specifying and solving the general radiation problem every time.

Instead, the rates provided in the UMIST database are provided in the accessible form below, for rate coefficient, k:

$$k = \alpha e^{-\gamma \cdot A_V} \qquad (\mathrm{s}^{-1}), \tag{1.12}$$

where α is the rate in the unshielded interstellar UV field, A_V is the visual optical depth to the point under consideration, and γ represents the attenuation with depth. The coefficients α and γ are provided in the database and details of the radiative transfer are simplified to just the exponential factor. This is possible because the rates are precalculated using a fixed set of assumptions about the problem.

Firstly, the Draine estimate for the background radiation field is used. This is needed just to calculate the unshielded rate, α. If a different estimate is desired then the rate could be scaled; however, a simple scale factor would be inappropriate if the wavelength dependence varies from the Draine field.

Secondly, the problem is reduced to that for a plane-parallel slab-shaped cloud. Any point in such a cloud can be described by a single value: the optical depth to the surface; which greatly simplifies the modelling. However, the total optical depth of the cloud is also significant, since there is a difference of intensity between a point 1 mag into a cloud of 10 mag thickness and a point 1 mag into a cloud 100 mag thick. To perform the radiative transfer calculation for the cloud, a particular dust model also needs to be assumed (Roberge et al. 1991, for example).

For a slab-shaped cloud the radiative transfer problem can be solved analytically at any single wavelength, and so the photoreaction rate at depths through the cloud can be calculated. The exponential decay then provides a reasonable fit to the change of rate through the cloud. (van Dishoeck (1988) states that this fit is accurate to factors of a few for any slab thicker than about 5 mag in total.)

1.3.3 Photoreaction rates from radiative transfer

The main disadvantage of the approach described above is that it is linked to many assumptions about the medium. Firstly, it might be desirable to try other dust models and other estimates for the background UV field, both of which are imprecisely determined. And, perhaps more significantly, clouds with shapes other than the simple slab can only be roughly approximated.

If a radiative transfer method is used to calculate the penetration of UV into the cloud, then the photoreaction rates could be deduced from the cross-sections and substituted into the chemical model without affecting other reactions. In a single point model the only related consideration is for the cosmic ray induced photoreactions. These can be handled in the same manner as before since the rates only depend on local conditions at the point. However, for consistency the value used for the dust albedo (Section 1.1.2.4) should be related to the dust model used in the main radiative transfer. (There is another consideration for multi-point models which we will discuss in Section 2.3.)

1.3.3.1 Comparison between methods

Figures 1.3 to 1.6 show a comparison between the photoreaction rate coefficient (k) calculated using the UMIST database approximation and from the cross-sections and radiation field in a slab-shaped cloud. (The total reaction rate could be given by kN_s, where N_s is the number density of the species absorbing UV.)

Note that the UMIST-style rate coefficients have all been calculated using $k = (\alpha/2)e^{-\gamma \cdot A_V}$, where α is the unshielded rate quoted in the database. In this way the rate approaches half the unshielded value at the edge of the cloud; although, for clouds of finite total depth, the rate at the edge will actually be between 0.5 and 1.0 times the unshielded value.

The field intensity used to produce the cross-section based graphs was obtained using the radiative transfer model to be described in Chapter 2. We expect some variation in the rates due to differences in the cross-sections and dust/cloud models used, but it is also clear that the rate coefficient does not follow a simple exponential even in a plane-parallel slab, and that the differences between the simple exponential approxi-

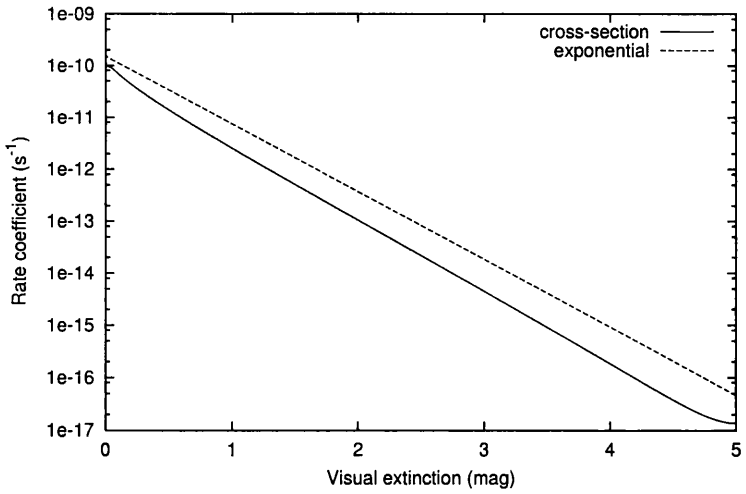

Figure 1.3: Rate coefficient for the reaction: C + Photon $\longrightarrow$ $C^+ + e^-$ showing variation with depth inside a semi-infinite slab-shaped cloud with total optical depth of 10.0 mag. The two lines shown are for the UMIST-style value $1.5 \times 10^{-10} e^{-3.0 \cdot Av}$ and the value obtained from the cross-section (Cantù et al. 1981) and UV-field directly.

mation and a more accurate treatment are likely to be significant in the determination of chemical abundances.

1.3.3.2 Obtaining cross-section information

One of the major problems associated with modelling photoreactions using the radiation field directly is obtaining cross-section information for the many photoionization and photodissociation reactions present in the UMIST database. Although many of the reactions are based on approximations or partial experimental or theoretical results, there is still an imposing number of actual cross-section data to accumulate.

The solution we propose is to obtain the cross-section data only for the reactions which are 'important' for the species under study in the particular case. It would not make sense to use the exponential approximation still for the others, but it is possible to construct a substitute cross-section based on the two parameters in the UMIST rate file.

Such a cross-section can be defined to reproduce the unshielded rate exactly, and to have an appropriate dependence on extinction. The actual rates obtained in a general radiation field will not be accurate, but they will, at least, reflect the shape of the radiation field within a cloud and therefore be more appropriate for non slab-shaped

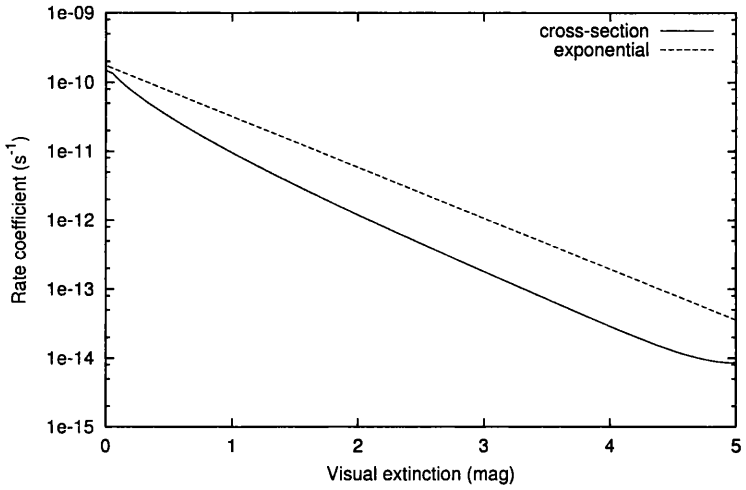

Figure 1.4: Rate coefficient for the reaction: OH + Photon $\longrightarrow$ O + H showing variation with depth inside a semi-infinite slab-shaped cloud with total optical depth of 10.0 mag. The two lines shown are for the UMIST database value $1.75 \times 10^{-10} e^{-1.7 \cdot Av}$ and the value obtained from the cross-section (van Dishoeck & Dalgarno 1984) and UV-field directly.

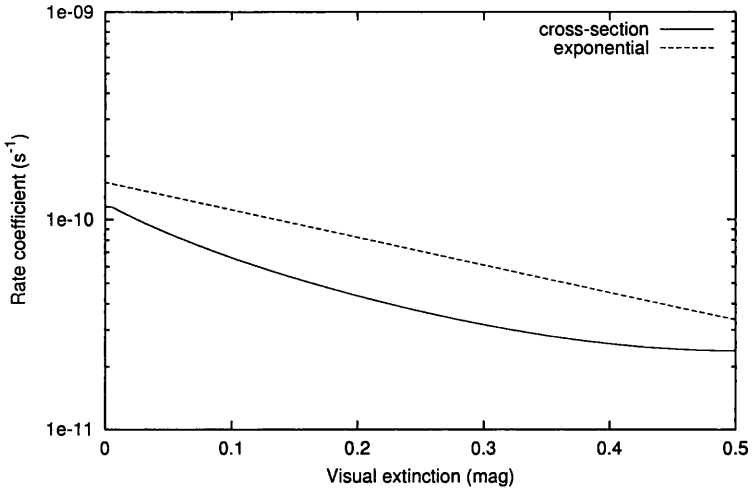

Figure 1.5: Rate coefficient for the reaction: C + Photon $\longrightarrow$ $C^+ + e^-$ showing variation with depth inside a semi-infinite slab-shaped cloud with total optical depth of 1.0 mag. The two lines shown are for the UMIST-style value $1.5 \times 10^{-10} e^{-3.0 \cdot Av}$ and the value obtained from the cross-section (Cantù et al. 1981) and UV-field directly.

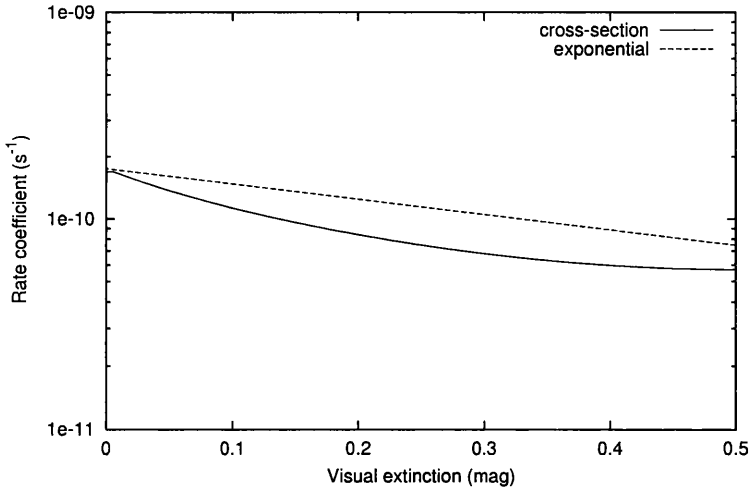

Figure 1.6: Rate coefficient for the reaction: OH + Photon $\longrightarrow$ O + H showing variation with depth inside a semi-infinite slab-shaped cloud with total optical depth of 1.0 mag. The two lines shown are for the UMIST database value $1.75 \times 10^{-10} e^{-1.7 \cdot A_V}$ and the value obtained from the cross-section (van Dishoeck & Dalgarno 1984) and UV-field directly.

models.

There are two possible approaches to constructing artificial cross-sections. (Bearing in mind that we only have two parameters: α, the rate coefficient for the unshielded reaction; and γ, which describes the exponential decay.)

Best fit to UMIST rate We could model the cross-section as a weighted sum of orthogonal pieces, a_i, such that: $\sigma(\lambda) = \sum_{i=1}^{n} w_i a_i(\lambda)$, where $\int a_i a_j \, d\lambda \equiv 0$, $\forall i \neq j$. Then we can calculate the weights w_i to reproduce the exponential rate coefficient $\alpha e^{-\gamma \cdot A_V}$ at n depths into a slab-shaped cloud. This technique will give us a cross-section that should reproduce the UMIST rates well in similar circumstances. But the behaviour of such rates in models with different background UV fields or wavelength dependence in the dust optical properties may be more influenced by the particular choice of $a_i(\lambda)$ than anything else. That is, the rate coefficient from such a cross-section may behave in an inappropriate way if the wavelength-dependence of the incident field is different from that assumed in the exponential approximation (rather than just the overall field strength).

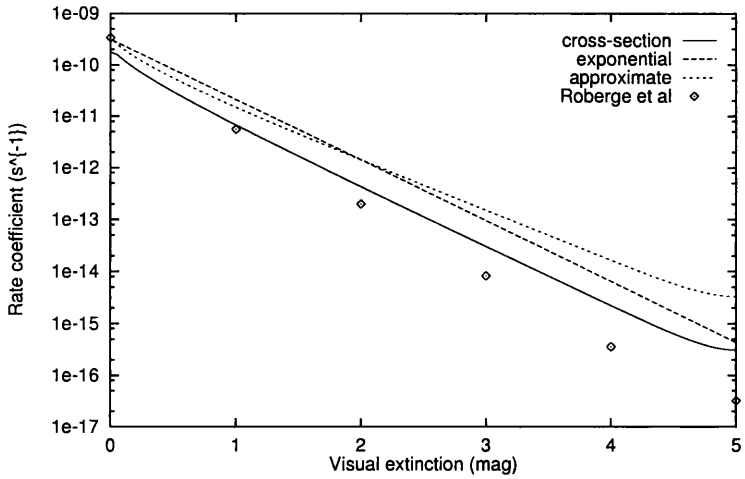

Figure 1.7: Rate coefficient for the reaction: H_2S + Photon $\longrightarrow$ $H_2S^+ + e^-$ showing variation with depth inside a semi-infinite slab-shaped cloud with total optical depth of 10.0 mag. The lines shown are: 'exponential', for the UMIST database value $3.15 \times 10^{-10} e^{-2.7 \cdot A_V}$; 'cross-section', for the values obtained from the measured cross-section (Watanabe & Jursa 1964); 'approximate', for an artificial cross section constant between 912Å and a cut-off determined from the UMIST γ coefficient. Finally we have added points corresponding to the rate calculated by Roberge et al. (1991) for this cloud.

Approximation from extinction curve For the general case we prefer the much cruder solution of cross-referencing the value of γ on the interstellar extinction curve to find a wavelength value which is associated with the depth dependence of the rate. We can use this wavelength as the peak position, or the low cut-off for a cross-section of fixed geometry. The size of the cross-section would be calculated to reproduce the unshielded reaction rate.

Figure 1.7 shows a comparison between the exponential approximation and the rate coefficients obtained from the actual and artificial cross-section for photoionization of H_2S. The artificial cross-section used has constant value between 912Å and a cut-off wavelength determined from the γ coefficient in the UMIST rate file.

The dust parameters used to calculate the radiation field for Figure 1.7 are the same as those used by Roberge et al. (1991). The rates calculated for the measured cross-section are the best match to Roberge et al.'s values; the discrepancy is probably mainly due to differences in the cross-sections used. The approximate cross-section is not everywhere closer to the proper rate value than the exponential approximation

but it does mimic the form of the real cross-section rate better, flattening off towards the cloud's centre. This gives us hope that the approximate cross-sections will behave more appropriately than an exponential in clouds of different shape.

1.3.3.3 Summary

In this section we have shown that the actual rates of photoreactions can differ substantially from the exponential approximation used in the UMIST rate file even in the plane-parallel slab-shaped cloud case. If different dust or radiation parameters are desired, or a differently shaped cloud is to be modelled, then the rates should be calculated from experimentally measured reaction cross-sections and the actual radiation field within the cloud.

To overcome the requirement for very large amounts of detailed cross-section information we have proposed a simple cross-section model based on the parameters used for the exponential approximation. Such approximate cross-sections will give rates of limited accuracy at any individual point, so are insufficient for accurate modelling of their associated species. However, the rates will change in proportion to the change in the radiation field throughout the cloud.

The combination of the approximate cross-sections with actual cross-section data for important reactions, when coupled with a suitable radiative transfer model, enables the modelling of chemistry under conditions other than those assumed for the UMIST database.

1.4 Chemical effects of cloud structure

In Section 1.1.2 the main physical properties which determine reaction rates inside a gas cloud were discussed. Some of those properties are closely related to the overall structure of the cloud, so the large-scale nature of the medium can help determine the chemistry within both directly and indirectly.

1.4.1 Gas density

It seems unlikely that a cloud in the interstellar medium would have constant gas density throughout. Because two-body reactions are more efficient at higher densities, there will be a direct dependence on the density structure through those reactions. The gas chemistry may well run at different speeds in different regions of the cloud. However, the relation between reaction rates and density is linear so a large difference in density is required to give any large increases in the rates.

As was mentioned in Section 1.1.3, if there is transport of material between different regions then the higher density regions may 'feed' the chemistry in the lower density regions. This produces an indirect effect on the chemistry. Modelling such an effect is complex and well beyond the scope of this work, even if appropriate density structures and dynamics were well known.

1.4.2 Optical depth

The concept of optical depth is defined with reference to a single line of sight. Unlike the case of gas density above, a small change in optical depth greatly affects the intensity of radiation received: the relation of received intensity to optical depth is exponential (received/incident intensity $I/I_0 = e^{-\tau}$, for optical depth τ). Moreover, insofar as the optical depth affects conditions at a point, the optical depths along all lines of sight are important.

The shape and density structure of a cloud will therefore have a strong effect in determining rates of reactions which depend on external radiation, namely: cosmic rays and interstellar UV. We might consider the 'average optical depth' as indicative of the overall level of shielding from external radiation, and the point below applies to

both cosmic rays and UV. However, the levels of optical depth at which cloud shape will make a difference for cosmic rays are substantially higher than for UV photons.

Overall levels of shielding The semi-infinite slab used to calculate rates for inclusion in the UMIST database offers more shielding than any other shape of cloud, though, for certain shapes/thicknesses, the difference may be negligible. The assumption is that the cloud is significantly larger along two axes than along a third. But there are many interesting shapes for which that is not true, including the other one-dimensional shapes: the sphere and the filament. In general, a point τ mag inside the surface of a cloud will have less overall shielding (lower average optical depth) than a point τ mag inside a slab.

In addition, scattering from dust grains can have a significant effect on the received ultraviolet flux. This means that the strength of the UV field at a point within the cloud can depend on more than just the average optical depth.

Scattering from high density regions The contribution of scattering to the radiation field inside a cloud is quite significant at low optical depths. An inhomogeneous density structure might therefore lead to interesting variations in the radiation field: not only will higher density regions be more shielded, but incident UV may reflect off these regions and add to the field in nearby regions elsewhere. However, any effect of this nature seems likely to be significant mainly in clouds subjected to a non-isotropic UV field.

Directional scattering from grains Even in a isotropic field, the scattering properties of the dust grains may lead to results peculiar to the shape of the cloud. If the grains are aligned in some way, perhaps by a strong magnetic field, then they may have different optical properties along different directions. In such a case the resulting field will certainly depend on the overall shape of the cloud.

But even with randomly oriented grains the cloud shape can be significant. Because grains may preferentially scatter forwards (or backwards) then incident light may effectively be 'focused' by a cloud of suitable shape. For example, Sandell & Mattila (1975) showed that a spherical cloud with forward scattering grains will have a central

intensity higher than the optical depth would suggest.

1.4.3 Modelling the effects of cloud shape

We have suggested above that the most interesting, and most important, effect of cloud shape may be on the ultraviolet field (and hence photoreaction rates). Certainly it seems this is one aspect where simple variations may lead to quite significant changes in the overall outcome.

In the next chapter we will describe a simple radiative transfer method designed to let us change one or more of the assumptions used in the UMIST photoreaction model.

Bibliography

Alves, J., Lada, C. J. & Lada, E. A. (1999), 'Correlation between gas and dust in molecular clouds: L977', *Astrophys. J.* **515**, 265–274.

Bergin, E. A., Lellouch, E., Harwit, M., Gurwell, M. A., Melnick, G. J., Ashby, M. L. N., Chin, G., Erickson, N. R., Goldsmith, P. F., Howe, J. E., Kleiner, S. C., Koch, D. G., Neufeld, D. A., Patten, B. M., Plume, R., Schieder, R., Snell, R. L., Stauffer, J. R., Tolls, V., Wang, Z., Winnewisser, G. & Zhang, Y. F. (2000), 'Submillimeter Wave Astronomy Satellite observations of Jupiter and Saturn: Detection of 557 GHZ water emission from the upper atmosphere', *Astrophys. J.* **539**, L147.

Bergin, E. A., Melnick, G. J. & Neufeld, D. A. (1998), 'The post-shock chemical lifetimes of outflow tracers and a possible new mechanism to produce water ice mantles.', *Astrophys. J.* **499**, 777–792.

Bettens, R. P. A., Lee, H. H. & Herbst, E. (1995), 'The importance of classes of neutral-neutral reactions in the production of complex interstellar molecules', *Astrophys. J.* **443**, 664.

Cantù, A. M., Mazzoni, M. & Tozzi, G. P. (1981), 'Photoionization spectrum of the ^3P ground state of neutral carbon', *Phys. Rev. A* **23**(3), 1223–1228.

Cecchi-Pestellini, C. & Williams, D. A. (1998), 'Evolving interstellar extinction', *Mon. Not. Roy. Astron. Soc.* **296**, 414–418.

Chaffee, F. H. J. & Lutz, B. L. (1977), 'Line spectra in interstellar clouds. III - weak lines below 3400 a in Zeta Persei', *Astrophys. J.* **213**, 394.

Chen, W. & Graham, J. (1993), 'Ice grains in the Corona Australis molecular cloud.', *Astrophys. J.* **409**, 319–326.

Cox, P., Gusten, R. & Henkel, C. (1988), 'Observations of C_3H_2 in the diffuse interstellar medium', *Astron. & Astrophys.* **206**, 108.

Crawford, I. A. & Williams, D. A. (1997), 'Detection of interstellar NH towards Zeta Ophiuchi by means of ultra-high-resolution spectroscopy', *Mon. Not. Roy. Astron. Soc.* **291**, L53.

Dickman, R. L., Horvath, M. A. & Margulis, M. (1990), 'A search for scale-dependent morphology in five molecular cloud complexes', *Astrophys. J.* **365**, 586–601.

Draine, B. T. (1978), 'Photoelectric heating of interstellar gas.', *Astrophys. J. Sup.* **36**, 595–619.

Drdla, K., Knapp, G. R. & van Dishoeck, E. F. (1989), 'The CS molecule in diffuse interstellar clouds', *Astrophys. J.* **345**, 815–827.

Falgarone, Phillips & Walker (1991), 'The edges of molecular clouds: fractal boundaries and density structure', *Astrophys. J.* **378**, 186–201.

Felenbok, P. & Roueff, E. (1996), 'OH in the line of sight to HD 27778 and Zeta Persei', *Astrophys. J.*

Feuchtgruber, H., Helmich, F. P., van Dishoeck, E. F. & Wrigth, C. M. (2000), 'Detection of interstellar CH_3', *Astrophys. J.* **535**, 111L–114L.

Geballe, T. R., McCall, B. J., Hinkle, K. H. & T, O. (1999), 'Detection of H_3^+ in the diffuse interstellar medium: The galactic center and Cygnus OB2 number 12', *Astrophys. J.* **510**, 251.

Gomez-Gonzalez, J. & Lequeux, J. (1975), 'On the interpretation of Copernicus observations of interstellar absorption lines in front of Xi Persei', *Astron. & Astrophys.* **38**, 29.

Gondhalekar, P. M., Phillips, A. P. & Wilson, R. (1980), 'Observations of the interstellar ultraviolet radiation field from the S2/68 sky-survey telescope', *Astron. & Astrophys.* **85**, 272.

Haffner, L. M. & Meyer, D. M. (1995), 'A search for interstellar C_3 in the translucent cloud toward HD 147889', *Astrophys. J.*

Helmich, F. P., van Dishoeck, E. F., Black, J. H., de Graauw, T., Beintema, D. A., Heras, A. M., Lahuis, F., Morris, P. W. & Valentijn, E. A. (1996), 'Detection of hot, abundant water toward AFGL 2591', *Astron. & Astrophys.* **315**(2), L173–L176.

Heyer, M. H., Carpenter, J. M. & Ladd, E. F. (1996), 'Giant molecular cloud complexes with optical HII regions: ^{12}CO and ^{13}CO observations and global cloud properties', *Astrophys. J.* **463**, 630.

Hindmarsh, A. C. (1972), Linear multistep methods for ordinary differential equations: Method formulations, stability and the methods of Nordsieck and Gear (UCRL-51186), Technical report, Lawrence Livermore Laboratory.

Hudson, R. L. & Moore, M. H. (1999), 'Laboratory studies of the formation of methanol and other organic molecules by water + carbon monoxide radiolysis: relevance to comets, icy satellites and interstellar ices', *Icarus* **140**, 451.

Jannuzi, B. T., Black, J. H., Lada, C. J. & van Dishoeck, E. F. (1988), 'The small molecular cloud toward HD 169454', *Astrophys. J.* **332**, 995.

Jones, A. P. & Williams, D. A. (1984), 'The 3 μm ice band in Taurus: implications for interstellar chemistry.', *Mon. Not. Roy. Astron. Soc.* **209**, 955–960.

Jones, A. P., Duley, W. W. & Williams, D. A. (1990), 'The structure and evolution of hydrogenated amorphous carbon grains and mantles in the interstellar medium', *Quart. J. Roy. Astron. Soc.* **31**, 567.

Jura, M. (1976), 'Cloud collapse and star formation', *Astron. J.* **81**, 178.

Lambert, D. L., Sheffer, Y. & Crane, P. (1990), 'CN, CH, and CH^+ toward Zeta Ophiuchi', *Astrophys. J.* **359**, 19L.

Lambert, D. L., Sheffer, Y., Gilliland, R. L. & Federman, S. R. (1994), 'Interstellar carbon monoxide toward Zeta Ophiuchi', *Astrophys. J.* **420**, 756L.

Le Teuff, Y. H., Millar, T. J. & Markwick, A. J. (2000), 'The UMIST database for astrochemistry 1999', *Astron. & Astrophys. Sup.* **146**, 147.

Léger, A., Klein, J., de Cheveigne, S., Guinet, C., Defourneau, D. & Belin, M. (1979), 'The 3.1 μm absorption in molecular clouds is probably due to amorphous H_2O ice', *Astron. & Astrophys.* **79**, 256–259.

Leitch-Devlin, M. A. & Williams, D. A. (1985), 'Sticking coefficients for atoms and molecules at the surfaces of interstellar dust grains', *Mon. Not. Roy. Astron. Soc.* **213**, 295.

Lepp, S., Dalgarno, A. & van Dishoeck, E. F. (1988), 'Large molecules in diffuse interstellar clouds', *Astrophys. J.* **329**, 418.

Liszt, H. & Lucas, R. (1994), 'Plateau de Bure observations of mm-wave molecular absorption from ^{13}CO, HCO^+, and HCN', *Astron. & Astrophys.* **282**, 5L.

Lucas, R. & Liszt, H. (1997), Millimeter-wave observations of diffuse clouds, *in* E. van Dishoeck, ed., 'Molecules in Astrophysics: probes and processes', p. 421.

Lucas, R. & Liszt, H. S. (2000), 'Comparative chemistry of diffuse clouds.I. C_2H and C_3H_2', *Astron. & Astrophys.* **358**, 1069.

Maier, J. P., Lakin, N. M., Walker, G. A. H. & Bohlender, D. A. (2001), 'Detection of C_3 in diffuse interstellar clouds', *Astrophys. J.* **553**, 267.

Meyer, D. M. & Roth, K. C. (1991), 'Discovery of interstellar NH', *Astrophys. J.* **376**, L49.

Millar, T., Farquhar, P. & Willacy, K. (1997), 'The UMIST database for astrochemistry 1995', *Astron. & Astrophys. Sup.* **121**, 139–185.

Millar, T., Rawlings, J., Bennet, A., Brown, P. & Charnley, S. (1991), 'Gas phase reactions and rate coefficients for use in astrochemistry—the UMIST ratefile', *Astron. & Astrophys. Sup.* **87**, 585.

Morton, D. C. (1975), 'Interstellar absorption lines in the spectrum of Zeta Ophiuchi', *Astrophys. J.* **197**, 85.

Nguyen, T. K., Hartquist, T. W. & Williams, D. A. (2001), 'Polyatomic species in diffuse cloud and clump interfaces', *Astron. & Astrophys.* **366**, 662.

O'neill, P. T. & Williams, D. A. (1999), 'Interstellar water and interstellar ice', *Astrophys. & Sp. Sci.* **266**, 539–548.

Pirronello, V., Liu, C., Roser, J. E. & Vidali, G. (1999), 'Measurements of molecular hydrogen formation on carbonaceous grains', *Astron. & Astrophys.* **344**, 681.

Rawlings, J. M. C., Hartquist, T. W., Menten, K. M. & Williams, D. A. (1992), 'Direct diagnosis of infall in collapsing protostarts–I. the theoretical identification of molecular species with broad velocity distributions', *Mon. Not. Roy. Astron. Soc.* **255**, 471–485.

Roberge, W. G., Jones, D., Lepp, S. & Dalgarno, A. (1991), 'Interstellar photodissociation and photoionization rates.', *Astrophys. J. Sup.* **77**, 287–297.

Sandell, G. & Mattila, K. (1975), 'Radiation density and lifetimes of molecules in interstellar dust clouds.', *Astron. & Astrophys.* **42**, 357–364.

Savage, B. D. & Sembach, K. R. (1996), 'Interstellar abundances from absorption-line observations with the Hubble Space Telescope', *Ann. Rev. Astron. Astrophys.*

Savage, B. D., Drake, J. F., Budich, W. & Bohlin, R. (1977), 'A survey of interstellar molecular hydrogen. I', *Astrophys. J.*

Smith, A. M., Bruhweiler, F. C., Lambert, D., Savage, B. D., Cardelli, J. A., Ebbets, D. C., Lyu, C. & Sheffer, Y. (1991), 'First results from Goddard High-Resolution Spectrograph—CI, SI, and CO toward Xi Persei and the physical conditions in diffuse clouds', *Astrophys. J.* **377**, 61L–64L.

Smith, R., Sellgren, K. & Brooke, T. (1993), 'Grain mantles in the Taurus dark cloud.', *Mon. Not. Roy. Astron. Soc.* **263**, 749.

Snow, T. P. (1977), 'Copernicus studies of interstellar material in the Perseus II complex. III—the line of sight to Zeta Persei', *Astrophys. J.* **216**, 724.

Snow, T. P. & Witt, A. N. (1996), 'Interstellar depletions updated: Where all the atoms went', *Astrophys. J.* **468**, L65.

Snow, T. P., Lamers, H. J. G. L. M. & Joseph, C. L. (1987), 'High-resolution ultraviolet observations of interstellar lines', *Astrophys. J.* **321**, 952–957.

Spitzer, L. (1978), *Physical Processes in the Interstellar Medium*, J. Wiley & Sons.

Turner, B. E. (1995*a*), 'The physics and chemistry of small molecular clouds in the galactic plane. 3: NH3', *Astrophys. J.* **444**, 708.

Turner, B. E. (1995*b*), 'The physics and chemistry of small translucent molecular clouds. V. SO and SO2', *Astrophys. J.* **455**, 556.

Turner, B. E. (1996*a*), 'The physics and chemistry of small translucent molecular clouds. VI. Organo-Sulfur species', *Astrophys. J.* **461**, 246–264.

Turner, B. E. (1996*b*), 'The physics and chemistry of small translucent molecular clouds. VII. SO^+ and H_2S', *Astrophys. J.* **468**, 694–721.

Turner, B. E. (1998), 'The physics and chemistry of small translucent molecular clouds. XI. Methanol', *Astrophys. J.* **501**, 731–748.

Turner, B. E. (2000), 'A common gas-phase chemistry for diffuse, translucent, and dense clouds?', *Astrophys. J.* **542**, 837.

Turner, B. E., Pirogov, L. & Minh, Y. C. (1997), 'The physics and chemistry of small translucent molecular clouds. VIII. HCN and HNC', *Astrophys. J.* **483**, 235–261.

Turner, B. E., Terzieva, R. & Herbst, E. (1999), 'The physics and chemistry of small translucent molecular clouds. XII. more complex species explainable by gas-phase processes', *Astrophys. J.* **518**, 699.

Umebayashi, T. & Nakano, T. (1980), 'Recombination of ions and electrons on grains and the ionization degree in dense interstellar clouds', *Pub. Astron. Soc. Japan* **32**, 405–421.

van Dishoeck, E. F. (1988), Photodissociation and photoionization processes., *in* T. J. Millar & D. A. Williams, eds, 'Rate Coefficients in Astrochemistry', Kluwer Academic Publishers, pp. 49–72. Proceedings of a conference held at UMIST.

van Dishoeck, E. F. (1998), The chemistry of diffuse and dark interstellar clouds, *in* T. W. Hartquist & D. Williams, eds, 'The molecular astrophysics of stars and galaxies', pp. 53–99.

van Dishoeck, E. F. & Black, J. H. (1986), 'Comprehensive models of diffuse interstellar clouds—physical conditions and molecular abundances', *Astrophys. J. Sup.* **62**, 109.

van Dishoeck, E. F. & Black, J. H. (1988), 'The photodissociation and chemistry of interstellar CO', *Astrophys. J.* **334**, 771.

van Dishoeck, E. F. & Dalgarno, A. (1984), 'Photodissociation of OH in interstellar clouds', *Astrophys. J.* **277**, 576–580.

van Dishoeck, E. F. & Helmich, F. P. (1996), 'Infrared absorption of H_2O toward massive young stars', *Astron. & Astrophys.* **315**(2), L177–L180.

van Dishoeck, E. F., Phillips, T. G., Black, J. H. & Gredel, R. (1991), 'CO J=3–2 observations of translucent and high-latitude molecular clouds', *Astrophys. J.* **366**, 141.

Vejby-Christensen, L., Andersen, L., Heber, O., Kella, D., Pedersen, H., Schmidt, H. & Zaifman, D. (1997), 'Complete branching ratios for the dissociative recombination of H_2O^+, H_3O^+ and CH_3', *Astrophys. J.* **483**, 531.

Vidali, G., Roser, J. & Pirronello, V. (1999), Experimental hydrogen recombination reactions on interstellar dust grain analogues, *in* F. Combes & G. Pineau des Forêts, eds, 'H_2 in Space', Cambridge University Press, p. E14.

Viti, S., Williams, D. A. & O'neill, P. T. (2000), 'Hydrocarbons in diffuse and translucent clouds', *Astron. & Astrophys.* **354**, 1062–1070.

Wagenblast, R. (1992), 'Interpretation of the level population distribution of highly rotationally excited H_2 molecules in diffuse clouds', *Mon. Not. Roy. Astron. Soc.* **259**, 155.

Wagenblast, R. & Williams, D. A. (1993), *in* T. J. Millar & D. A. Williams, eds, 'Dust and Chemistry in Astronomy', Institute of Physics Publishing Ltd.

Wagenblast, R. & Williams, D. A. (1996), 'Revised chemical models of ζ Oph based on HST data', *Astrophys. & Sp. Sci.* **236**, 257–265.

Wagenblast, R., Williams, D. A., Millar, T. J. & Nejad, L. A. M. (1993), 'On the origin of NH in diffuse interstellar clouds', *Mon. Not. Roy. Astron. Soc.* **260**, 420.

Watanabe, K. & Jursa, A. S. (1964), 'Absorption and photoionization cross sections of H_2O and H_2S', *J. Chem. Phys.* **41**(6), 1650.

Weingartner, J. C. & Draine, B. T. (1999), 'Interstellar depletion onto very small dust grains', *Astrophys. J.* **517**, 292–298.

Whittet, D., Bode, M., Longmore, A., Adamson, A., McFadzean, A., Aitken, D. & Roche, P. (1988), 'Infrared spectroscopy of dust in the Taurus dark clouds—ice and silicates.', *Mon. Not. Roy. Astron. Soc.* **233**, 321–336.

Williams, D. A. (1998), *in* 'Faraday Discussion 109', Royal Society of Chemistry, p. 1.

Williams, D. A., Clary, D. C., Farebrother, A., Fisher, A., Gingell, J. M., Jackman, R., Mason, N., Meijer, A., Perry, J., Price, S. D., Rawlings, J. M. C. & Williams, D. E. (1999), The energetics and efficiency of H_2 formation on surfaces of interstellar grain mimics, *in* F. Combes & G. Pineau des Forêts, eds, 'H_2 in Space', Cambridge University Press.

Williams, T., Adams, N., Babcock, L., Herd, C. & Geoghan, M. (1996), 'Production and loss of the water-related species H_3O^+, H_2O and OH in dense interstellar clouds.', *Mon. Not. Roy. Astron. Soc.* **282**, 413–420.

Willner, S. P., Gillet, F. C., Herter, T. L., Jones, B., Krassner, J., Merril, K. M., Pipher, J. L., Puetter, R. C., Rudy, R. J., Russell, R. W. & Soifer, B. T. (1982), 'Infrared spectra of protostars: composition of the dust shells', *Astrophys. J.* **253**, 174–187.

Chapter 2

Radiation

In which a method for calculating radiative transfer is presented. The influence of dust grain parameters on the radiation field is examined. A chemical representation of the cloud is described, and how abundances throughout the cloud can affect the chemistry through line radiation. Finally, a comparison is made between slab and sphere-shaped clouds: in radiation, and chemistry.

2.1 Introduction

As described in the last chapter, we wish to know the ultraviolet radiation field inside axisymmetric dust clouds illuminated only by a diffuse external field. This is a somewhat unusual problem, firstly because we need to evaluate the angle-averaged intensity received over a large region of space rather than at a particular point or in a particular direction. Secondly, we do not have a particular source for the radiation: the UV is incident from everywhere outside the cloud and in every direction. In addition we do not wish to develop a method tied to any particular geometry other than the axisymmetry we expect. This criterion is important because, as already mentioned, the nature of the cloud collapse—and hence cloud structure—depends on the chemistry which we desire to model.

Finally we want to be able to choose a dust model (albedo, scattering angle dis-

tribution, etc.) freely; and, because of the possibility that the dust properties may be affected by the environment, it would be helpful if the dust model can also be varied with position.

Monte Carlo techniques are, in principle, ideal for examining situations with very complex structure. However, such methods are usually only really efficient when either the radiation source or the output data can be restricted in position or direction. Thus we have developed a non-randomized iterative method, described in the following sections, which takes advantage of the symmetries assumed for the clouds but remains general with regard to all the dust parameters. Although the method can be specialized to some degree for particular problems, high accuracy is always liable to be computationally expensive for the code developed. But, as we will illustrate later in this chapter, the accuracy achievable by this method in reasonable time is enough to enable chemical models to reflect the global properties of the cloud.

2.1.1 How the radiative transfer model works

The radiative transfer code that has been developed has been called RTc, and is loosely based on a method developed by Efstathiou & Rowan-Robinson (1990). Because the dust grains in these clouds are cold there is no thermal emission in the ultraviolet from the dust which means that the radiative transfer model does not need to take the thermal balance into account. Furthermore, because most photoreaction rates are determined by the ultraviolet continuum we shall not be modelling line transfer, with the exception described in Section 2.3. Thus the problem of obtaining a suitable UV field can be reduced to a set of independent radiative transfer calculations at different wavelengths. In the description below we mainly refer to a single wavelength calculation and all the dust properties mentioned are wavelength dependent. To evaluate photoreaction rates we require several wavelengths spanning the region of interest.

RTc is an iterative process in which each iteration takes account of an additional scattering by dust. We begin with the "unscattered" radiation field which is determined at any point only by the extinction to the edge of the cloud, and include as many scatterings (iterations) as needed before convergence is obtained to within the level of accuracy required. The rate of convergence depends on the dust's optical properties.

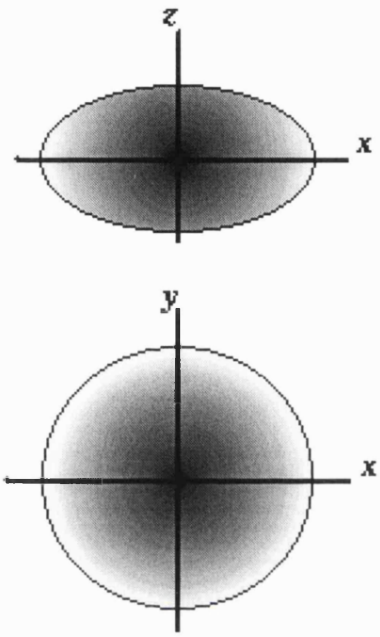

Figure 2.1: We model dust clouds which are axisymmetric about the z-axis and symmetric by reflection in the xy-plane.

For the dust model we use in the next chapter (§3.2.1.1), which has albedo 0.3–0.6, in clouds with low optical depth ($\lessapprox 5$ mag) only a few iterations are necessary to converge within the level of accuracy of the method.

The *specific intensity*, $I_\lambda(\mathbf{x}, \theta, \mu)\, d\lambda\, dA\, d\Omega\, dt$ is the number of photons with wavelength $\lambda \to \lambda + d\lambda$ passing through area dA in time dt at position $\mathbf{x}$, within solid angle $d\Omega$ of the direction (θ, μ).

The radiation field (at each wavelength) in the cloud is represented by a set of specific intensity values over a grid of angles and positions throughout the cloud. We will call the set of values representing the field after the i^{th} iteration $\mathcal{F}_i$, where $\mathcal{F}_0$ measures the light which penetrates the cloud without being scattered. Each value in $\mathcal{F}_0$ is calculated exactly in the "zeroth iteration" by calculating the extinction to the edge of the cloud for each grid point.

Iteration $i + 1$ calculates a set of values $\mathcal{S}_{i+1}$ representing the radiation resulting from a single scattering by dust of field $\mathcal{F}_i$, and the new field estimate after this itera-

tion is given by $\mathcal{F}_{i+1} = \mathcal{F}_0 + \mathcal{S}_{i+1}$. Thus $\mathcal{S}_1$ represents light which has been scattered exactly once and $\mathcal{F}_1$ represents light scattered zero or one times. $\mathcal{S}_2$ is then light scattered exactly one or two times, and $\mathcal{F}_2$ contains zero to two scatterings. So the field $\mathcal{F}_i$ after i iterations contains $0 \cdots i$ scatterings by dust.

The dust clouds which we want to model are axisymmetric (we call this the z-axis) and symmetric by reflection in the xy-plane through their centre. (See Figure 2.1.) The RTc code takes advantage of this symmetry by only calculating values for the radiation field on a cross-section in the xz-plane. Any values needed for $y \neq 0$ can be obtained by rotation into this plane. Furthermore, we only need to consider one quadrant of this plane: $x \geq 0$, $z \geq 0$. We divide this quadrant using grids in x (really radius in xy-plane) and z, each of which can be varied to be most appropriate for the cloud structure (see Figure 2.2 for example). The intersection points of the grid specify the points in the cloud at which RTc will calculate field values. At each point the specific intensity is calculated for a number of fixed directions (see Figure 2.3 for example). Thus the radiation field $\mathcal{F}_i$ is a set of values: $I_i(x, z; \theta, \psi)$, the specific intensity received at (x, z) from direction (θ, ψ). θ is the angle measured from the positive-z direction and ψ is the angle between the x-axis and the projection of the ray in the xy-plane.

The equation of radiative transfer along a ray is (Rybicki & Lightman 1979):

$$\frac{dI_\lambda}{ds} = -\alpha_\lambda I_\lambda + j_\lambda, \tag{2.1}$$

where α_λ is the absorption coefficient (cm^{-1}) representing the loss of intensity from a beam over distance ds, thus $dI_\lambda = -\alpha_\lambda I_\lambda ds$; and j_λ is the emission coefficient: intensity emitted per unit time per solid angle per unit volume. In general, the absorption and emission coefficients will be functions of position.

The optical depth from s_0 to s along a ray is defined as

$$\tau_\lambda(s) = \int_{s_0}^{s} \alpha_\lambda(s')\, ds'. \tag{2.2}$$

The medium we are modelling scatters but does not emit so we use the solution

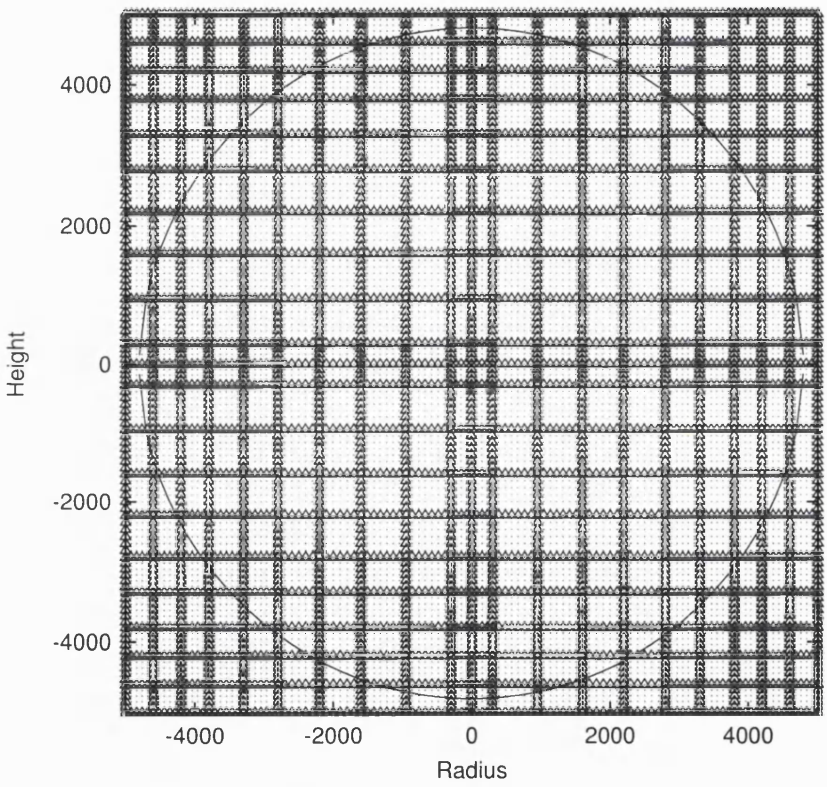

Figure 2.2: An example of the grids used in x and z. This set would be used for a spherical cloud with radius $\lessapprox 5000$. (The x (radius) and z (height) distances are in arbitrary units.) The complete cloud is shown, although only one quarter is calculated: the others are obtained by reflection. Points marked by triangles have calculated scattered intensities, other points have their scattered contributions interpolated at each iteration.

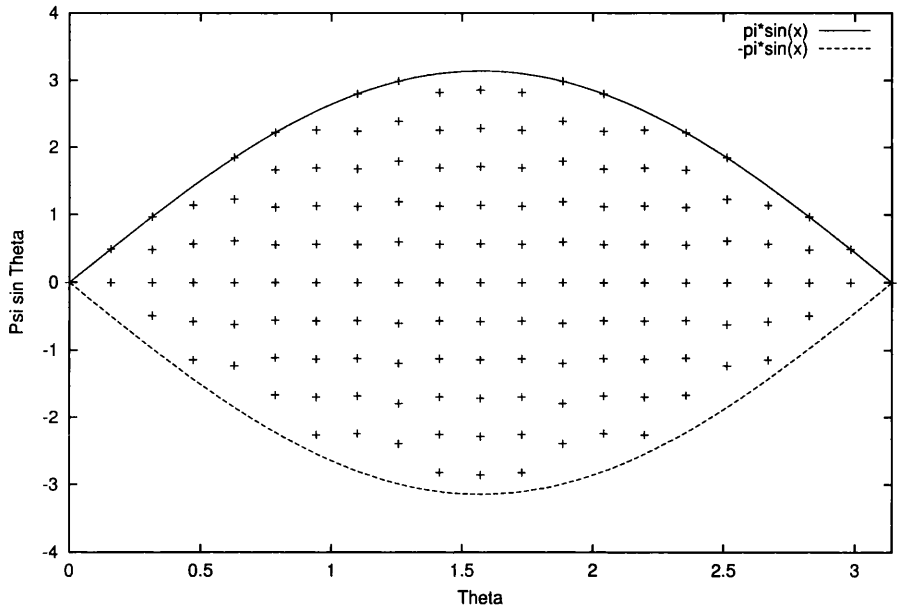

Figure 2.3: An example of the set of angular directions (θ, ψ) at which specific intensities are calculated by the RTc code. Each point plotted above corresponds to one of these directions, plotted on the graph as $(x = \theta, y = \psi \sin\theta)$. The surrounding curve is $y = \pm\pi \sin\theta$ so the enclosed area depicts the region containing all possible directions.

below:

$$I(x, z; \theta, psi) = e^{-\tau(\infty)} I(\infty; \theta, \psi) + \int_{s=0}^{\infty} e^{-\tau(s)} \cdot I^s(s)\, ds, \tag{2.3}$$

where s is the distance along the ray to (x, z) from direction (θ, ψ), and $\tau(s)$ the corresponding optical depth. In practice, ∞ is the edge of the cloud, so $I(\infty)$ is the incident intensity on the cloud (constant) and $\tau(\infty)$ the optical depth from the point to the cloud edge. The first term above is the "unscattered" intensity received at the point, and the second term represents the contribution from scattered light: $I^s(s)$ is the specific intensity of light scattered into the ray direction between s and $s + ds$.

$$I^s(s \to s + ds) = c_s \int_{\theta'=0}^{\pi} p(\Theta) \cdot \int_{\psi'=0}^{2\pi} I(s; \theta', \psi')\, d\psi'\, d\theta', \tag{2.4}$$

where $I(s; \theta, \psi)$ is the specific intensity from direction (θ, ψ) at distance s along the

ray, and $\Theta = \Theta(\theta, \psi, \theta', \psi')$ is the angle between (θ', ψ') and the ray direction. The properties of the dust determine the phase function $p(\Theta)$, which specifies the scattering angle distribution for light reflected from a dust grain, and the scattering coefficient c_s. The scattering coefficient specifies how much intensity passing through a unit distance will be scattered by the dust. This parameter is related to the albedo and the average dust cross-section per unit volume. For the models described in this work we take $c_s = \omega c_e$, where ω is the albedo, and c_e is the dust extinction per distance: $\tau(s) = \int c_e \, ds$. These parameters (c_e, c_s, p) represent the complete description of the dust cloud as required by the RTc model; they can all vary with position and wavelength.

Looking at Equation 2.3, we can see that the first term depends only on the geometrical position of the point and direction of the ray, the properties of the cloud, and the strength of the external field. That term can be calculated as precisely as desired just by evaluating the optical depth. So these only need to be computed once for each wavelength. The complete set of specific intensities given by only the non-scattering term constitute the $\mathcal{F}_0$ of the method.

The second term in Equation 2.3, however, depends on the specific intensities elsewhere in the cloud. In each iteration of the method we calculate for each point/direction $(x, z; \theta, \psi)$ an improved estimate of the scattering term in which we use the radiation field calculated in the previous iteration to provide $I(s; \theta', \psi')$. The integration along the ray is performed numerically using intersections of the ray with the spatial grid as integration points. Thus,

$$I_i(x, z; \theta, \psi) = I_0(x, z; \theta, \psi) + S_i, \tag{2.5}$$

where S_i is a numerical integral using intensities interpolated from the $I_{i-1}(x, z; \theta, \psi)$ already calculated.

These integrals are expensive computationally, therefore a compromise is used in the code. The number of grid intersections for a ray needs to be reasonably high in order to maintain accuracy and to sufficiently sample potentially changing cloud conditions. We can achieve this by only calculating the scattered intensities S_i for some of the points on the grid. The appropriate values for the other points are then interpolated

(along rays in the appropriate directions) from the calculated values at the end of each iteration. Figure 2.2 shows an example of a grid with shells having calculated values interspersed with shells whose values are interpolated. Constraints on the grid design and efficiency issues are discussed in slightly more detail in the appendix.

The next section describes a few tests of the method to demonstrate that it generates an acceptably accurate radiation field.

2.1.2 Validating RTc model

It is necessary to test the RTc code to ensure that it appears to give correct results and to gauge the accuracy of the method. The accuracy will be significantly affected by the size of the spatial and angular grids used to represent the radiation field. The size of the grids used will be a trade-off between desired accuracy and computation time available.

2.1.2.1 Non-scattering case

The simplest case to test for the RTc code is the case of non-scattering dust. The initial step for the code is to calculate the radiation field within the cloud neglecting scattered light: the $\mathcal{F}_0$ values. For the conditions we consider, this is the dominant element in the final result and therefore needs to be correct. There is an exact analytical solution for the one-dimensional spherical case (Bell & Williams 1983). We can therefore attempt to model a spherical cloud using RTc.

Because the code is two-dimensional, the field we obtain is two-dimensional and we need to "collapse" the results to give a 1D plot of mean intensity against radius. This collapse of points from different regions in the 2D grid to similar radii gives a scatter of results indicative of the basic numerical errors in the code. The distribution of these points around the analytical solution is determined by the inaccuracies in the optical depth calculation (insignificant for homogeneous clouds) and the numerical integration of specific intensities to find the mean intensity. The latter is dependent on the set of directions used. The errors in these results do not depend on the spatial grid used because the values for each point are calculated independently of the others.

Figure 2.4 shows a comparison between the analytical solution for penetration into

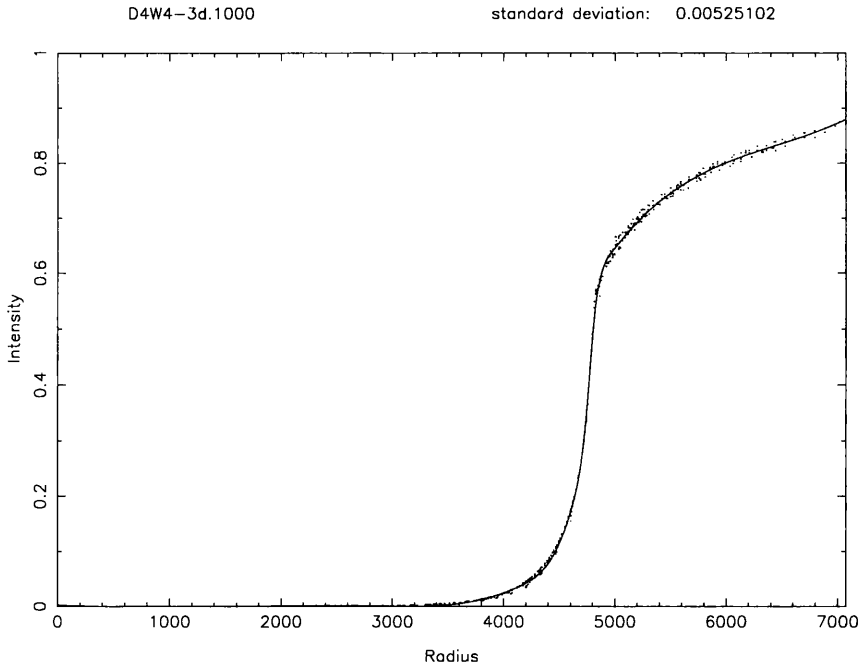

Figure 2.4: Model of a spherical cloud with optical depth to the centre of 12 mag and no scattering. The solid line is the analytical solution for the mean angle-integrated intensity relative to the incident intensity, and the dots represent values calculated by the RTc code. The standard deviation of the RTc results from the analytical solution is 0.005.

a non-scattering spherical cloud with values from an RTc model. The cloud has optical depth to the centre of 12 mag and radius 4800 (arbitrary units). This roughly corresponds to the intensity at 1000Å inside a cloud with visual extinction of 3 mag to the centre. The agreement is good, with the worst variation occurring outside the cloud (radius> 4800).

2.1.2.2 Purely forward scattering

The case of dust grains that scatter always directly forward is equivalent to a case of non-scattering grains but with a reduced extinction factor: $c_e^{\text{effective}} = c_e - c_s = (1 - \omega)c_e$. We could therefore also compare the theoretical non-scattering solution with results from the RTc code using scattering, but with purely forward scattering grains.

Unfortunately it is implicit in the method used that the RTc results will deteriorate with highly forward or backward scattering phase functions. This is because the 2D

g	0.8	0.9	0.95	0.97	0.99
Std. Dev.	0.0601	0.0557	0.0535	0.0531	0.0529

Table 2.1: Standard deviation of RTc model results using forward scattering in a cloud of optical depth 5 mag, with dust albedo 0.7, from the analytical solution for the non-scattering cloud with depth 1.5 mag. Various values are taken for the mean scattering cosine, g.

continuum of possible ray directions is approximated by a finite number of rays; when the important range of directions is confined to a small angular region the approximation used by the code becomes worse because only a few rays will lie in the important region. In fact, the method breaks down completely for strictly forward or backward scattering. However, we can examine cases of very high forward scattering and see how well they fit the theoretical curve, and test several different albedo values.

In these cloud models we use the Henyey-Greenstein phase function for the scattering (Equation 3.3). The wavelength-dependence appears in that function via the single parameter, g, the mean scattering angle cosine. Isotropic scattering occurs when $g = 0$, and $g = 1$ implies purely forward scattering.

Table 2.1 shows that the RTc model does converge slowly towards the purely forward scattering case, but the performance is not good. Even at $g = 0.99$, for example: this RTc model estimates the intensity in the centre of the cloud as 0.166 (relative to incident), whereas analytically the value should be 0.233.

To obtain good performance in the case of highly non-isotropic scattering would require a model with a very large set of angles, which would be prohibitively expensive computationally.

2.1.2.3 Reflectivity and central intensity

Another simple test is to measure the values of Reflectivity and the mean intensity at the centre of spherical clouds. Tiné et al. (1992) give values for a number of spherical cloud models, both homogeneous and inhomogeneous. We compare the results of RTc models for the homogeneous cases in Tables 2.2 and 2.3.

The reflectivity, $\mathcal{R}$, is the ratio of mean intensity of light leaving the cloud to the

τ_c	Scattering	Tiné et al. (1992)	RTc
1 mag	isotropic	0.542	0.574 ± 0.024
1 mag	HG: $g = 0.5$	0.535	0.569 ± 0.024
10 mag	isotropic	0.170	0.215 ± 0.053
10 mag	HG: $g = 0.5$	0.109	0.198 ± 0.055

Table 2.2: Reflectivity values from models of homogeneous spherical clouds with optical depth to the centre τ_c. The dust albedo in all models is 0.5, and the scattering phase function used is the Henyey-Greenstein function with $g = 0$, corresponding to isotropic scattering.

τ_c	Scattering	Tiné et al. (1992)	RTc
1 mag	isotropic	5.61×10^{-1}	5.83×10^{-1}
1 mag	HG: $g = 0.5$	5.86×10^{-1}	5.98×10^{-1}
10 mag	isotropic	3.64×10^{-4}	1.12×10^{-3}
10 mag	HG: $g = 0.5$	1.24×10^{-3}	2.43×10^{-3}

Table 2.3: Central mean intensity values (relative to incident) for homogeneous spherical clouds with a dust albedo of 0.5 and optical depth to the centre τ_c. The scattering phase function used in the models is the Henyey-Greenstein function with $g = 0$ corresponding to isotropic scattering.

incident intensity, I_0.

$$\mathcal{R} = (2/I_0) \int_0^1 I(R, \mu)\, d\mu, \tag{2.6}$$

where R is the radius of the cloud and μ is the sine of the angle to the surface normal.

Because RTc is a 2D method we can calculate multiple values for the reflectivity in our model at various points on the cloud edge. The scatter in these values is due to the inaccuracy in the method and we show the average and the standard error in Table 2.2. The RTc results do lie within these error bounds of the values quoted from Tiné et al. (1992) but the errors are quite large and so this measure can not distinguish between similar cloud cases.

2.1.2.4 Other published cases

Sandell & Mattila (1975) present results from Monte-Carlo models of homogeneous spherical clouds which we can also compare with to some extent. They test models with central optical depths up to 40 mag, which is well beyond the depths for which RTc is appropriate.

Albedo	Sandell & Mattila (1975)	RTc
0.2	-1.88	-1.84
0.4	-1.50	-1.47
0.6	-1.10	-1.06
0.8	-0.60	-0.43

Table 2.4: Log mean intensities relative to incident ($\log J/J_0$) at the centre of spherical dust clouds with various grain albedo values. The optical depth to the centre is 5 mag. The values from Sandell & Mattila (1975) are read from their graph with estimated accuracy around ± 0.06.

In Table 2.4 we show central intensities for clouds with optical depth 10 mag for a range of dust albedo. This is at the limit of the range RTc is intended for, nevertheless, the agreement is reasonable, at least for low albedo dust. This suggests that the main inaccuracy in our model is in the scattering.

Flannery et al. (1980) developed an analytical solution for plane-parallel and homogeneous spherical clouds using spherical harmonics. Their method is the technique used to calculate the radiation field for many of the photoreactions included in the UMIST database. Unfortunately, we have not managed to make comparisons with that method.

2.1.2.5 General accuracy

In Figure 2.5 we show RTc results for a homogeneous sphere with full scattering. That data corresponds to the cloud of Figure 2.4 but in this case six scatterings have been included. We have fitted a cubic spline through the model results and evaluated the standard deviation of the results from this line as 0.011. This gives an estimate of the overall inaccuracy in the method (which largely results from the scattering part of the calculation). The size of the scatter in the results depends very strongly on the size of the grids used to divide the cloud and how well they sample the optical depth. For these size grids the inaccuracy in the method appears larger than any discrepancy from the expected results.

In Figure 2.5 and, more clearly, in Figure 2.10 later it is possible to detect linear patterns in the scatter of values from RTc. These patterns arise mainly from the interaction of the spherical cloud and the rectangular spatial grids which do not sample the edge region well. The problem is exacerbated by the use of homogeneous clouds

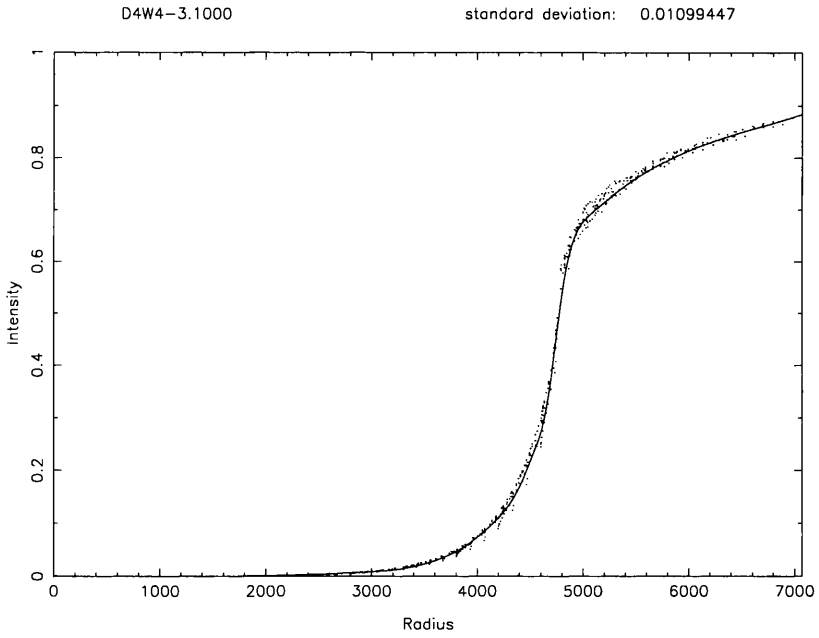

Figure 2.5: Mean intensity relative to incident intensity: data points from an RTc model of a homogeneous spherical cloud with optical depth to the centre of 12 mag. A best fit cubic spline (solid line) has been fitted to the data with standard deviation 0.011. The dust at this wavelength had albedo 0.7 and scattered isotropically.

whose density changes radially as a step function. The edge region of the cloud is very important for the scattered light intensity and we would expect better results for clouds with a gradual density decrease.

2.1.2.6 Summary

We hope to have shown that the method developed can produce radiative transfer results correct to within its level of accuracy.

This method is unsuited to very precise calculations since they would require a great deal of computation. However, the strength of the model is its generality: it can be used to model any axisymmetric cloud provided the grid spacings can practically be made small enough to sample whatever inhomogeneity is present.

2.2 Influence of dust grains

2.2.1 Dust optical properties

Let us briefly examine the effect of the dust properties on the radiation field inside the cloud. For simplicity we use the one-dimensional slab for this section. Figures 2.6 and 2.7 show how the mean intensity changes into various slab-shaped clouds with 6 mag of extinction in total. Radiation is incident isotropically on both sides of the cloud, and we consider a single wavelength with dust of constant density, albedo, ω, and scattering phase function throughout the cloud.

Albedo Figure 2.6 shows the effect of varying the dust albedo, keeping the phase function isotropic. The difference between the intensity for albedo 0.2 and 0.8 is around a factor of two or more within the cloud, and the change between different albedos does not appear to be linear. The dust model used by Roberge et al. (1991) to calculate many of the photo-rates in the UMIST database has an albedo that varies between 0.36 and 0.57 (see Figure 3.2). The effect of such a variation is relatively small compared to the potential variation; for example, with much higher albedo.

Phase function Figure 2.7 shows the effect of varying the preferred scattering direction. The albedo is fixed at 0.8 (high to emphasise effects), and the phase function asymmetry parameter is varied. The phase function used is the Henyey-Greenstein (Equation 3.3, which has asymmetry described by a single parameter, g. The scattering is isotropic for $g = 0$ and purely forward or backward scattering for $g = 1$ or $g = -1$ respectively. This parameter seems less significant than the dust albedo, but there is nonetheless a pronounced increase in the intensity within the cloud for the forward scattering case over the isotropic or backward scattering. The dust model of Roberge et al. (1991) has asymmetry varying from 0.46 to 0.64 (see Figure 3.3). The effect of this variation over wavelengths is likely to be small, but the fact that the dust scatters preferentially forward for all the wavelengths we consider is probably significant.

Convergence The radiative transfer method used is iterative, including an extra scattering at each iteration. The number of iterations required to converge the calculated

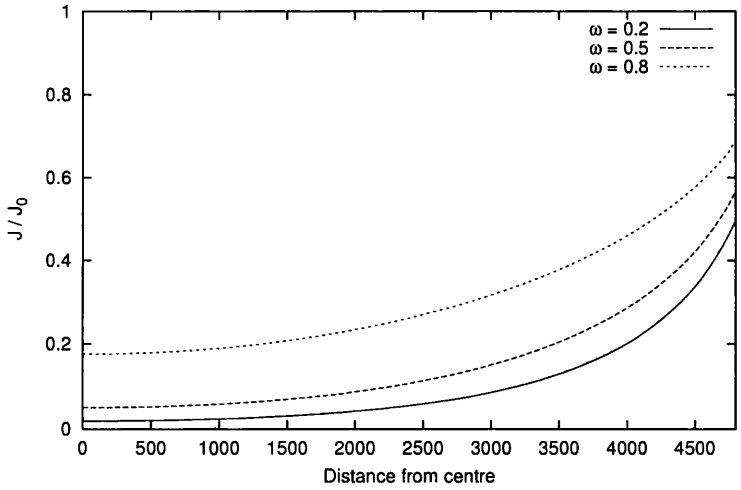

Figure 2.6: Mean, angle integrated intensity relative to incident intensity inside a slab-shaped cloud of half-width 4800 (arbitrary units). Optical depth 0–4800 is 3 mag, the dust scatters isotropically.

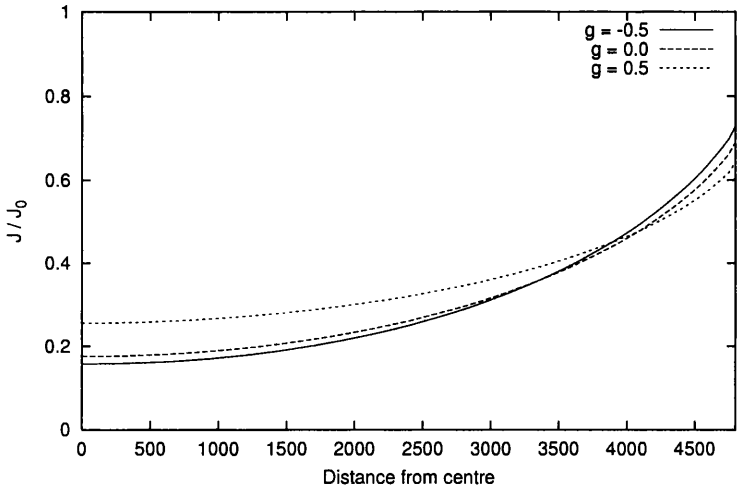

Figure 2.7: Mean, angle integrated intensity relative to incident intensity inside a slab-shaped cloud of half-width 4800 (arbitrary units). Optical depth 0–4800 is 3 mag, the dust has albedo 0.8.

g	ω		
	0.2	0.5	0.8
−0.5	2	4	9
0.0	2	4	9
0.5	2	4	9

Table 2.5: Number of iterations required before the specific intensities calculated for a plane parallel cloud of 3 mag of extinction to the centre converge such that the 2-norm of the change is less than 1.0×10^{-4}. Variation with changing dust properties is shown.

radiation field to within desired accuracy therefore depends on the dust properties. Table 2.5 shows the number of scatterings required before the 2-norm of the difference in calculated specific intensities drops below 1.0×10^{-4} for each of the models represented in the figures of this section.

As can be seen the number of scatterings required depends mainly on the albedo. (In fact, there is a slight dependence on the phase function parameter but it is insignificant in comparison.) Over the ranges in the Roberge et al. (1991) dust model it seems that 3 or 4 scatterings are likely to be sufficient.

2.2.2 Cosmic-ray induced photons

As was mentioned in Section 1.1.2, the optical properties of the dust also influence the effectiveness of photoreactions from UV emitted by H_2 following excitation by a cosmic ray. Because the radiation is generated evenly throughout the cloud—to the depths we are interested in—these reactions are not significantly influenced by the overall shape of the cloud and so the traditional UMIST approach will still suffice. In this approach, from Gredel et al. (1989), the rate coefficient for such reactions is given by

$$k = \xi\gamma/(1-\omega), \tag{2.7}$$

where ξ is the rate of cosmic ray incidence, γ is the efficiency of the reaction provided in the UMIST database, and ω is the albedo of the dust grains in the appropriate wavelength range (approximately 800–1800Å).

We merely note that the value chosen for the albedo needs to correspond to the dust model used for the continuum radiative transfer calculation. If the dust albedo varies

through the cloud then these reactions may have some positional dependence.

2.3 Influence of chemistry

As was mentioned in Chapter 1 the gas in the interstellar medium does not have a large effect on the passage of UV radiation (at least in comparison to the dust). One notable exception is the CO molecule.

The photodissociation of CO is dominated by line absorption rather than the continuum. Thus CO molecules in the outer region of an interstellar cloud can absorb radiation and protect molecules further inside the cloud: a process known as 'self-shielding'.

The rate of photodissociation of CO at a point within a cloud depends, therefore, on the column density of CO to the UV source. And hence, on the abundance of CO in the rest of the cloud. This means that we cannot represent the chemistry of this species properly without modelling its abundance throughout the cloud.

In addition, H_2 dissociation has some dependence on line radiation, including some overlap with the CO dissociation lines. So we also need to know the H_2 column density to evaluate the level of shielding for CO. The molecular hydrogen can be dealt with in the same manner as CO described below.

2.3.1 A multipoint chemical model

The chemical model we use in the rest of this work mirrors the previously described radiative transfer model. The symmetries of the clouds under consideration mean that we only need to model the chemistry in a two-dimensional fashion: considering only a single quadrant of a cross-section through the cloud along the axis of symmetry.

As before, we neglect any dynamical mixing of gas within the cloud, so that the chemistry at any point only depends on other points through the CO shielding. In particular, we run independent single-point chemical models over a grid of points within the cloud, complemented by a small number of points around the edge of the cloud. (Figure 2.8 shows the simple arrangement of points used for spherical clouds in the next chapter. The spheroidal clouds use an appropriately 'flattened' version.) Abundances at any point within the cloud can be interpolated trivially within the grid. The points around the edge of the cloud can be used separately to interpolate abundances

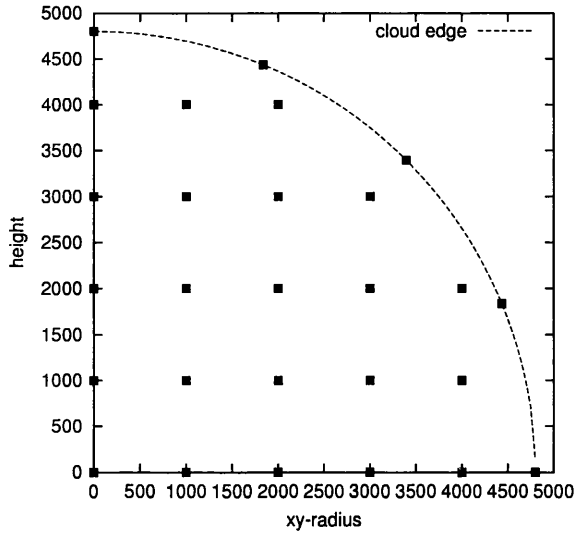

Figure 2.8: Positions of points within a spherical cloud of radius 4800 at which the gas-phase chemistry is modelled. The units of distance are arbitrary.

along the cloud's edge: thus enabling interpolation between the grid and the edge of the cloud. By rotating the cross-section about the axis we can estimate column densities through the cloud arbitrarily.

2.3.2 Modelling CO self-shielding

The self-shielding efficiency is complicated by the different behaviour of the different isotopes of CO and by the fact that H_2 can also affect the penetration of some of the appropriate lines. The UV spectrum which produces the photodissociation is now fairly well understood (van Dishoeck & Black 1988), and Mamon et al. (1988) have shown that it can be simplified to a limited number of bands, each with different behaviour and importance. However, a line transfer technique is needed to calculate the photodissociation rate correctly, and the method described earlier in this chapter is insufficient.

There is a fast approximation available for the plane-parallel, slab-shaped cloud case (van Dishoeck & Black 1988). That method involves comparing the shielding column-density of CO to a table of values precomputed for slabs of various CO and H_2 densities. As a first step towards modelling of the CO photodissociation we will

adopt this method, but attempt to adjust for the non-planar shape of our clouds. We will do this by using the average column density of CO to the edge of the cloud, $\overline{N_{\rm CO}}$. Using the average shielding as a parameter means that the photodissociation rate will depend on the shape of the cloud and position of the point within it.

However, we cannot simply equate $\overline{N_{\rm CO}}$ with the column density into a slab-shaped cloud as that would substantially overestimate the level of shielding. Instead we attempt to match against the average column density in the slab case. If we, arbitrarily, assume that most of the dissociating radiation at a point inside a slab is received from lines of sight with column densities not more than an order of magnitude more than the minimum (perpendicular) column density to the surface, $N_{\rm CO}^{\perp}$, then the effective average column density within a semi-infinite slab is $N_{\rm CO}^{\perp} \ln 10$. We assume, for simplicity, that all lines of sight to a point in the non-planar cloud contribute to the dissociating field (reasonable for low optical depth clouds). And so we approximate the CO dissociation rate by the corresponding rate at a depth $N_{\rm CO}^{\perp} = \overline{N_{\rm CO}}/\ln 10$ into a plane-parallel slab. We calculate the rate using software developed by Wagenblast (1992).

For efficiency we do not perform the column depth calculations in parallel with the chemical models for the points. Rather, we take an iterative approach whereby the abundances are initially calculated without self-shielding and then at each subsequent iteration the value of $\overline{N_{\rm CO}}$ is calculated from the abundances of the previous iteration.

This use of the total average column density of CO leads to a significant overestimation of the self-shielding near the edge of the cloud. Close to the cloud edge the minimum column of CO is more representative of the level of shielding provided. If CO self-shielding is to be calculated by reference to the slab-case in future work then this approximation should be replaced, perhaps by an average of column densities within an order of magnitude of the minimum column.

2.4 Effect of cloud shape

The main use for the radiative transfer method described in this chapter is examining the conditions inside interstellar clouds with shapes other than the plane-parallel slab. In this section we will briefly illustrate why this is useful by comparing slab-shaped clouds with spherical clouds of the same visual extinction.

Both the slab and the sphere are one-dimensional shapes and neither requires a two-dimensional radiative transfer code to evaluate the ultraviolet field strength within. However, the sphere is probably the next simplest cloud model to use, and illustrates the fact that all shapes other than the slab offer less UV shielding for a given optical depth.

In the next chapter a dust model (albedo and mean scattering angle) is described which is then used to calculate the radiation field suitable for use in chemical models of spheroidal clouds with radial optical depths ranging from 0.5 to 5 mag. In the following we will examine the UV intensity inside clouds which are modelled using that dust model (Section 3.2.1.1). We will also use the chemical model from the next chapter to briefly examine the size of the resulting effect on the chemistry.

2.4.1 Radiation field in planar and spherical clouds

Figures 2.9 and 2.10 compare the radiation fields inside plane parallel clouds and spherical clouds at a wavelength of 1040Å. In the dust model of Section 3.2.1.1 this wavelength corresponds to a dust albedo of about 0.38 and a mean scattering angle cosine of 0.54: somewhat forward scattering. The ratio of extinction at this wavelength to the visual extinction, A_V, is about 4.4.

When calculating the radiation field inside the spheres, we use a 2D approach and the inaccuracies of the method produce the spread of data points for the spherical case in the figures. For the high level of visual extinction in Figure 2.9, the cloud shapes have distinct intensity levels: the intensity is higher inside the sphere; but the difference is comparable to the spread in results from RTc, so we cannot distinguish very well between the two.

For the low extinction clouds of Figure 2.10, however, the difference in the radiation

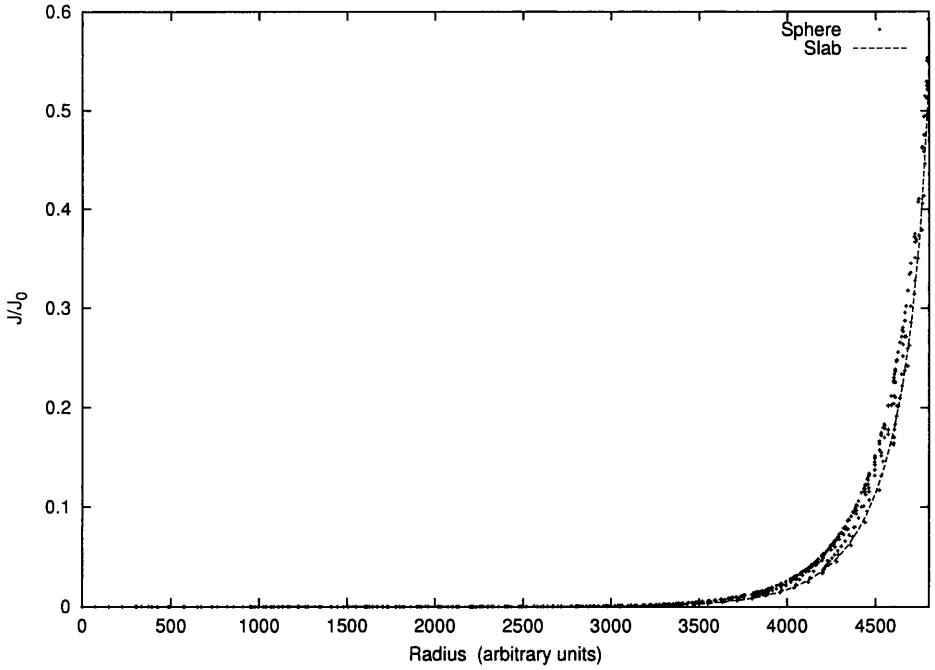

Figure 2.9: Mean intensity relative to incident at 1040Å inside slab shaped and spherical clouds with radius 4800 (arbitrary units) and optical depth to the centre of 5 mag.

fields is more pronounced. For clouds with this level of A_V the use of the RTc model as an alternative to the plane-parallel case appears justified despite the large scatter in results. This is reinforced below when we examine the resulting effect on chemical abundance.

2.4.2 Chemistry in planar and spherical clouds

In Figures 2.11 and 2.12 we display the fractional abundance of C^+ inside slab-shaped and spherical clouds. C^+ is a good tracer of the effect of radiation on the chemistry because at these levels of extinction it is produced primarily from photoionization of neutral carbon by interstellar UV. The relevant cross-section of C is narrow, 912 $\sim$ 1100Å. The chemistry of the sphere is modelled as described in the next chapter; the slab chemistry uses the same reaction set but the CO self-shielding is calculated using the method for plane parallel clouds mentioned in Section 2.3.2 directly.

As expected, in Figure 2.11, although the abundances of C^+ in the sphere all lie above the values for the slab the difference is small for the high optical depth clouds.

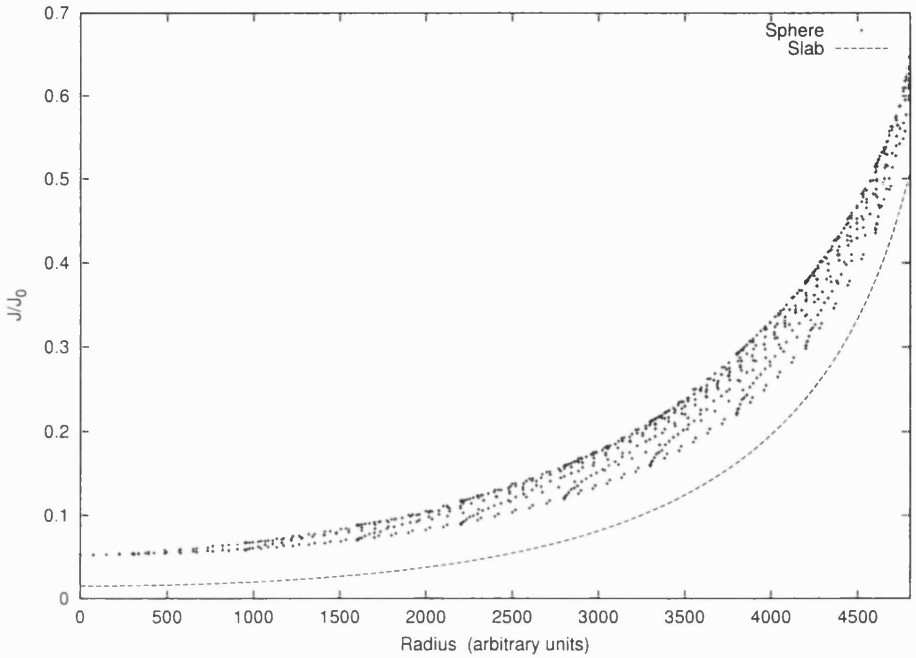

Figure 2.10: Mean intensity relative to incident at 1040Å inside slab shaped and spherical clouds with radius 4800 (arbitrary units) and optical depth to the centre of 1 mag.

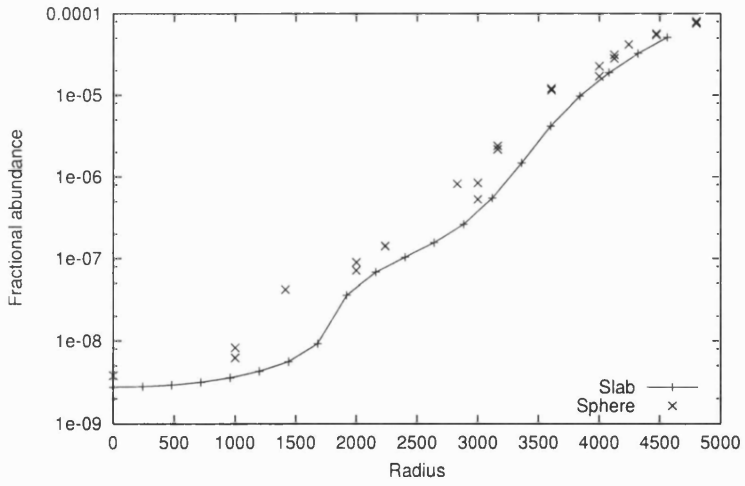

Figure 2.11: Fractional abundance of C^+ in slab and sphere shaped clouds with optical depth to the centre of 5 mag. The radius of the clouds is 4800 in arbitrary units. The y-axis of the plot uses a log-scale to exaggerate features of the graph.

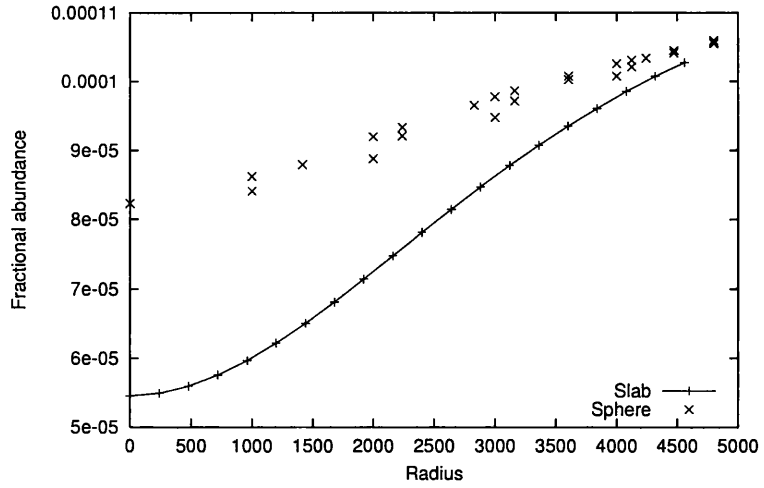

Figure 2.12: Fractional abundance of C^+ in slab and sphere shaped clouds with optical depth to the centre of 1 mag. The radius of the clouds is 4800 in arbitrary units.

For the low optical depth (0–1 mag) case, shown in Figure 2.12 the difference is marked. Though small in absolute terms the fractional abundances of C^+ are noticeably higher in the spherical cloud: well above the scatter in the results. Whether these changes will lead to any observable differences will depend on other details, but this example demonstrates that the shape of the cloud can be significant for the chemistry at a level detectable by the RTc code, even for simple one-dimensional clouds.

Bibliography

Bell, K. L. & Williams, D. A. (1983), 'The radiation field and the molecular hydrogen photodissociation rate within spherically symmetric inhomogeneous clouds.', *Mon. Not. Roy. Astron. Soc.* **202**, 407–416.

Efstathiou, A. & Rowan-Robinson, M. (1990), 'Radiative transfer in axisymmetric dust clouds.', *Mon. Not. Roy. Astron. Soc.* **245**, 275–288.

Flannery, B. P., Roberge, W. & Rybicki, G. B. (1980), 'The penetration of diffuse ultraviolet radiation into interstellar clouds.', *Astrophys. J.* **236**, 598–608.

Gredel, R., Lepp, S., Dalgarno, A. & Herbst, E. (1989), 'Cosmic ray–induced photodissociation and photoionization rates of interstellar molecules.', *Astrophys. J.* **347**, 289–293.

Mamon, G. A., Glassgold, A. E. & Huggins, P. J. (1988), 'The photodissociation of CO in circumstellar envelopes', *Astrophys. J.* **328**, 797–808.

Roberge, W. G., Jones, D., Lepp, S. & Dalgarno, A. (1991), 'Interstellar photodissociation and photoionization rates.', *Astrophys. J. Sup.* **77**, 287–297.

Rybicki, G. B. & Lightman, A. P. (1979), *Radiative Processes in Astrophysics*, John Wiley & Sons.

Sandell, G. & Mattila, K. (1975), 'Radiation density and lifetimes of molecules in interstellar dust clouds.', *Astron. & Astrophys.* **42**, 357–364.

Tiné, S., Aiello, S., Belleni, A. & Cecchi Pestellini, C. (1992), 'A solution to the prob-

lem of radiation transfer in inhomogeneous media using the SHM', *J. Quant. Spec. Rad. Trans.* **47**(2), 95–102.

van Dishoeck, E. F. & Black, J. H. (1988), 'The photodissociation and chemistry of interstellar CO', *Astrophys. J.* **334**, 771.

Wagenblast, R. (1992), 'Interpretation of the level population distribution of highly rotationally excited H_2 molecules in diffuse clouds', *Mon. Not. Roy. Astron. Soc.* **259**, 155.

Chapter 3

Cloud shape

In which some mechanisms by which interstellar clouds may collapse or be prevented from collapsing are discussed, and a simple 2D model for exploring changes through the collapse process is introduced. The radiation field inside these 2D spheroidal models is examined, and the results of chemical models of the clouds are presented. The effect of collapse, represented by flattening of the spheroids, on the chemistry is discussed, with some tentative suggestions of implications for the collapse process.

3.1 Introduction

One major application of a 2-dimensional model of interstellar clouds is to examine how the chemistry might change in a collapsing cloud.

There are several competing theories describing how an interstellar cloud can collapse, from the 'inside-out' spherical model of Shu (1977) to fully hydrodynamic numerical simulations suggesting that protostars do not form independently (Bhattal et al. 1998), and that clouds may collapse primarily because of the influence of shocks.

Simulations of the hydrodynamic collapse of interstellar gas are beyond the scope of this work, but we hope to show that the radiative transfer code described in the previous chapter, combined with currently existing chemical models can be used to

explore some of the questions regarding collapse mechanisms.

3.1.1 Dynamics of collapse

The basic difficulty in understanding how clumps in the interstellar medium collapse is to do with the rate. There are many regions in the interstellar medium with masses well above their Jeans mass, where thermal pressure cannot support the gas against its own gravity. The free-fall collapse of such a region would proceed quite quickly. Indeed the rate of collapse of such clouds is too high to be consistent with the levels of star formation that have been observed (Zuckerman & Palmer 1974).

There has, therefore, to be some mechanism providing support against gravity to slow collapse of self-gravitating regions of a cloud; possibly coupled with some other factor, such as shock waves, which assist or trigger collapse. This mechanism needs to be sufficient to slow down collapse but not sufficient to prevent the eventual formation of protostars.

For the sake of simplicity we will only consider homogeneous clouds of gas, which, left to their own devices would collapse in a smooth, spherical manner. Clouds with pronounced (asymmetric) density structure would have to be modelled numerically.

3.1.1.1 Support mechanisms

There are three popular candidates to offer support within an interstellar gas cloud. Both the first and last described below would result in a homogeneous region of gas collapsing in a two-dimensional, axisymmetric fashion. The chemistry of such regions could be examined using the methods described in this work.

Rotation If material in the cloud has a net rotation then centrifugal force will clearly offer some support perpendicular to the axis of rotation. However, observations of the interstellar medium have not revealed significant levels of rotation (Goldsmith & Arquilla 1985).

Turbulence If the gas is dynamically turbulent then support against gravity can be provided isotropically. But if turbulence were the main support mechanism in a cloud

we would expect the magnetic fields within the cloud to be quite tangled.

Magnetic fields with long-range order There is some evidence from polarization observations that fields in interstellar clouds can be ordered over very large distances (Vrba et al. 1976). The field may be approximately co-linear over the whole of the collapsing region. Such regions are, presumably, not being supported by turbulence.

The magnetic field can itself provide support through its effect on the charged components of the medium. Ions and electrons (and charged dust grains) are resisted in their motion across the field lines, and support can be provided along the field lines by Alfvén waves (see next section).

The field specifies a preferred axis through the cloud and the rate of collapse will differ perpendicular and parallel to this axis because the support mechanisms are different.

3.1.1.2 Magnetic support

The Lorentz force provides resistance to ions moving across the magnetic field lines. Neutral components do not experience this force, but nonetheless will be given some support through collisions with ions. The process of neutral molecules drifting past the ions is known as *Ambipolar diffusion* and its rate is determined by the ionization fraction.

Under the Lorentz force, thermal pressure and gravity alone, however, clumps in the interstellar medium would be expected to become very highly flattened. This degree of flattening is not observed.

Alfvén waves are transverse waves of charged particles travelling along the field lines. Mouschovias (1987) has shown that these can provide support in the field direction. With this mechanism it has been suggested that the degree of flattening obtained would be more in line with observations.

The rate of dissipation of the Alfvén waves also depends on the ionization fraction. Thus magnetic support by these mechanisms will not only lead to an axisymmetric collapse, but one in which the ongoing rate of collapse depends on the chemistry within the cloud, which we have already demonstrated may depend on the cloud's overall

shape. We hope to demonstrate that the axisymmetric radiation and chemistry models outlined in Chapter 2 are well suited to examining this kind of situation.

3.1.2 Flattened homogeneous sphere models

To examine the qualitative effect of axisymmetric collapse on the chemistry of a gas cloud we need a simple model of how the cloud might change. For this purpose we will introduce the 'flattened-sphere' model, which we will analyse for clouds of varying optical thickness.

Cloud shape We will consider clouds with spheroidal shape at several stages of 'flattening'. More precisely, the cross-section (parallel to the axis) of the clouds will be an ellipse; equation: $x^2 + y^2 + (z/\zeta)^2 = R^2$ in normal Cartesian coordinates.

We will consider clouds of fixed xy-radius, R, but with three different 'shape parameters' $\zeta = 1.0, 0.5, 0.25$ corresponding to a spherical cloud flattened to half and then a quarter of its initial height.

This is an arbitrary model for the change of shape. The collapse, while intrinsically axisymmetric, need not maintain a spheroidal shape. Furthermore, some contraction in the xy-plane is likely. However, we are interested in the general nature of the effect of changing shape so we use clouds from a common family.

Density For simplicity, we consider clouds which are all of uniform density throughout. However, to fit in with the idea of flattening the cloud, the density is varied with the shape parameter so that density, ρ_ζ for shape ζ, is given by $\rho_{0.5} = 2\rho_{1.0}$, and $\rho_{0.25} = 4\rho_{1.0}$. This corresponds to maintaining constant column density through the cloud in the z-direction, and hence also constant total mass, appropriate to a collapsing cloud.

The value of $\rho_{1.0}$ will be chosen in concert with the optical depth through the cloud.

Optical depth Part of the complication of dealing with a non-slab shaped cloud is that it is no longer so meaningful to speak of the optical depth to the surface. Nonetheless, we will parameterize our cloud models using the optical depth to the centre in the spherical case, τ_c. For $\zeta \neq 1.0$ this is still the optical depth to the surface along the

z-axis, but in all other directions the visual extinction changes. We will consider clouds with central optical depths: $\tau_c = 0.5, 1.0, 3.0, 5.0$ mag.

3.1.2.1 Density as the link between RT and chemistry models

Finally, we should note that the number density which is important for the purposes of radiative transfer is the number density of the interstellar dust grains; the gas density (for the environments we consider) being largely irrelevant regarding UV continuum transfer. However, in our models of the chemistry it is the gas density which is most important.

Except for the ratio of gas to dust the chemical and UV radiation models are independent. In fact, since the RTc method uses arbitrary distance units, the dust density is also arbitrary and the radiation results could be applied to any cloud with that shape and central optical depth. The ratio of gas column density to optical depth, $\Gamma = N_H/A_V$, should be chosen to be consistent with any assumptions made about the dust in the chemical model and this will then fix the physical size of the clouds as below:

$$\text{radius} = \Gamma \cdot \tau_c / n_H, \tag{3.1}$$

where n_H is the number density of hydrogen nuclei.

Throughout the rest of this chapter we will use the dimensionless units of distance for spatial coordinates within the cloud. The radiative transfer is performed for the region $0 \leq x \leq 5000$, $0 \leq z \leq 5000\zeta$, and the xy-radius of the clouds, R, is 4800.

In order to transform to physical distance, for example, to calculate column densities, a value for the gas:extinction ratio, Γ, is required. Estimates for this value can be obtained from measurements of $B-V$ colour excess given a model of the dust's properties and values for the column density on the line of sight, as shown in Jenkins & Savage (1974) and earlier papers. In this work we use the ratio $\Gamma = 1.6 \times 10^{21}\,\mathrm{cm}^{-2}/\,\mathrm{mag}$.

3.2 Radiation field inside spheroidal clouds

3.2.1 Radiative Transfer model

The radiative transfer model depends on the properties of the dust and the incident UV field. In this work we attempt to be as consistent as possible, data-wise, with previous work conducted with the UMIST rate file: varying only the calculation method wherever possible.

3.2.1.1 Dust properties

Many of the photo-rate coefficients in the UMIST rate file are taken from Roberge et al. (1991) and other works which use similar assumptions about the dust. Therefore, we have used the same optical dust model as that paper, which is credited to (Draine & Lee 1984). Because the clouds modelled are homogeneous there is no variation of the dust properties in space, the only dependence is in the wavelength.

Extinction coefficient The overall extinction of the dust is described relative to the extinction in the visible. Thus the dust model specifies X_λ, such that $\tau(\lambda) = X_\lambda A_V$, where $\tau(\lambda)$ is the optical depth at wavelength λ, and A_V is the visual extinction.

We have defined the size of the flattened-sphere clouds by τ_c, the A_V along the x-axis to their centre. Since the density is constant, the extinction coefficient, $c_e = d\tau/dx$ mentioned in Section 2.1.1 is given by the following relation:

$$c_e(\lambda) = X_\lambda \cdot \tau_c/\zeta R, \tag{3.2}$$

where R is the geometric radius of the cloud in the xy-plane, and ζ is the shape parameter (as in Section 3.1.2).

The extinction ratio, X_λ, is probably the most important dust property regarding variation of intensity with wavelength because it determines the optical depth which is related to the specific intensity by an inverse exponential. Figure 3.1 shows the interstellar extinction curve used by Roberge et al. (1991) and in this work.

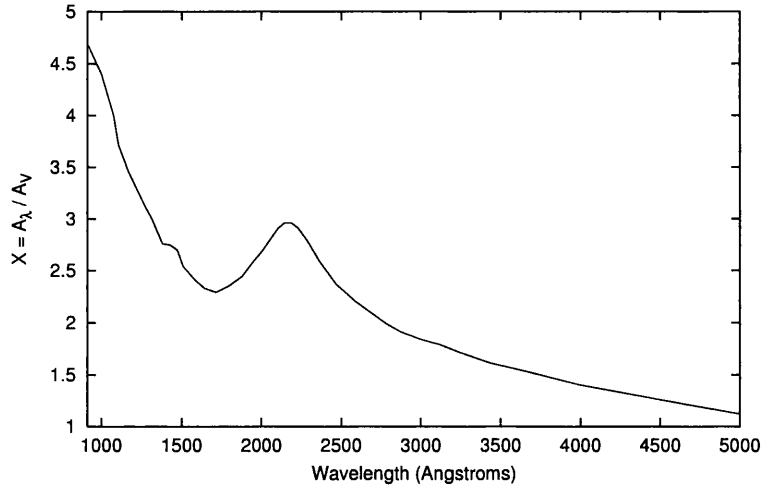

Figure 3.1: The ultraviolet extinction relative to the visible. This graph is based on that given in Roberge et al. (1991).

Albedo As described in Section 2.1.1, the albedo, ω, of the dust describes the ratio of scattered intensity to the total intensity intercepted by the dust. The scattering coefficient is: $c_s = \omega \cdot c_e$. The wavelength dependence of the albedo used is shown in Figure 3.2.

Phase function The scattering angle distribution for light reflecting from dust grains is described in this model by the Henyey-Greenstein phase function:

$$p(\cos\theta) = \frac{1 - g^2}{(1 + g^2 - 2g\cos\theta)^{3/2}}, \tag{3.3}$$

where the parameter $g = g(\lambda)$ is the mean scattering angle cosine. It describes the asymmetry of the distribution: $g = 0$ is isotropic scattering, $g = -1$ is purely backward scattering, and $g = 1$ is purely forward scattering.

The variation of g_λ depends on the nature of the dust grains: the values for the Draine & Lee model are shown in Figure 3.3.

3.2.1.2 Incident interstellar UV radiation field

The incident background UV field used is that described in van Dishoeck (1988). The field is an analytical fit to observations due to Draine (1978) below 2000Å, with an

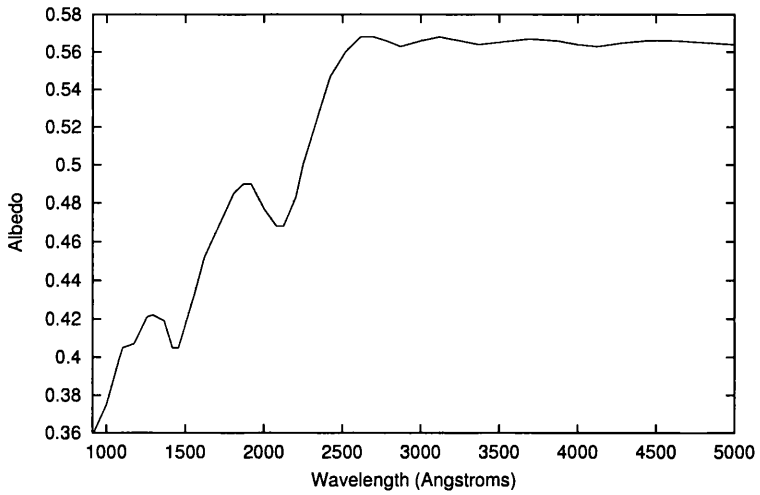

Figure 3.2: The albedo of the dust grains used in the RT model in this chapter; this describes the ratio of light which is scattered to the total light intercepted by the grains. This graph is based on that given in Roberge et al. (1991).

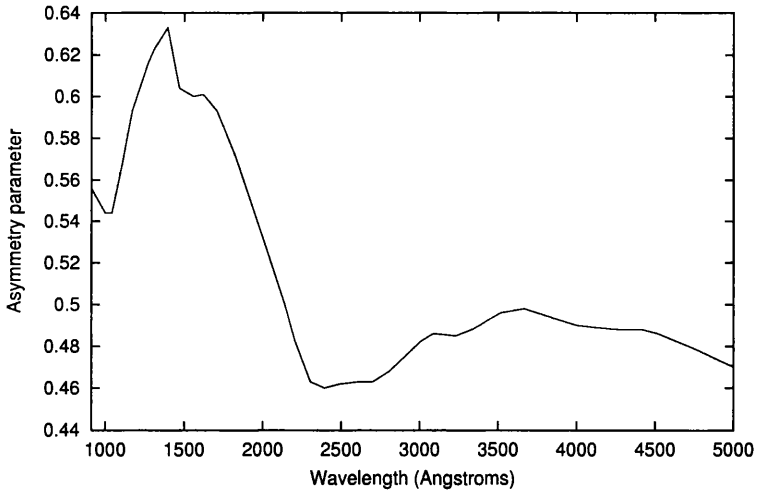

Figure 3.3: The phase function parameter, g_λ, which describes the shape of the scattering angle distribution for incident light of wavelength λ. This graph is based on that given in Roberge et al. (1991), appropriate for the Henyey-Greenstein phase function. The value of g_λ is the mean scattering angle cosine.

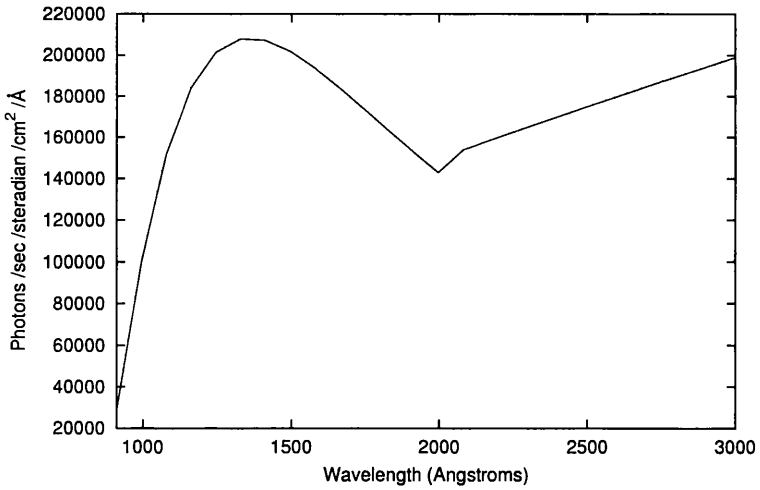

Figure 3.4: The mean, angle-averaged intensity of the interstellar radiation field, as described in van Dishoeck (1988).

extension (van Dishoeck & Black 1982) above.

$$I_0(\lambda) = \begin{cases} 3.2028 \times 10^{15} \cdot \lambda^{-3} - 5.1542 \times 10^{18} \cdot \lambda^{-4} + 2.0546 \times 10^{21} \cdot \lambda^{-5} \\ \qquad\qquad\qquad\qquad\qquad\qquad\qquad\qquad \text{when } \lambda \leq 2000\text{Å}, \\ 7.32 \times 10^{2} \cdot \lambda^{0.7} \qquad\qquad\qquad\qquad\qquad\qquad \text{when } \lambda > 2000\text{Å}. \end{cases} \tag{3.4}$$

The expression for I_0 above is in photons s^{-1} cm^{-2}Å^{-1} steradians^{-1}, and the wavelength dependence is illustrated in Figure 3.4.

3.2.2 Effect of collapse on the field

For the purposes of modelling the photochemistry within the clouds the change in the UV intensity over a range of intensities is important. To simplify examining the effect of the cloud shape on the radiation field we will plot just two wavelengths: 1040 and 2980Å. The latter is beyond the range of wavelengths that significantly affect most photoreactions but these two exemplify the extremes of the dust model: at 1040Å the extinction is high and the albedo low, while at 2980Å the reverse is the case.

3.2.2.1 Change in optical depths

Extinction levels in the z-direction do not change with the shape of the cloud, although a given optical depth will occupy less physical distance. Because the density increases inversely proportional to the shape parameter, ζ, optical depths in other directions do increase. For directions in the xy-plane, the extinction increases inversely proportional to ζ. So the quarter-height clouds have four times the optical depth along the x-axis as the equivalent spherical clouds.

3.2.2.2 Change in field shape

Figures 3.5 and 3.6 show contour maps of the mean, angle-averaged intensity within two families of clouds. (Measuring intensity relative to the incident intensity that would exist if there were no cloud at all). Only one quadrant needs to be shown because the cloud is symmetric in the x and z axes.

The obvious change in the shape of the field is the collapse in the z-direction. This is a trivial feature since the field is only attenuated within the cloud. However, because of the disproportionate increase in extinction on lines of sight off the z-direction, the mean intensity received at points within the cloud also decreases. The flattening causes the darkest region in the centre to grow: particularly along the xy-plane, which is illustrated by the contours meeting the x-axis at greater radii for more flattened clouds.

Figure 3.5 shows how the field drops within clouds of $A_V = 1$ along z-axis for wavelengths 1040 and 2980Å. The outer contour (for both wavelengths) is at 0.8 (relative to incident intensity) and, as expected, with the lower extinction at 2980Å, the intensity is much higher within the cloud than for 1040Å. For 1040Å the intensity in the centre is < 0.3, dropping below 0.2 as $\zeta > 1$; whereas for 2980Å the central intensity is < 0.7, dropping below 0.5 at $\zeta = 0.25$.

Figure 3.6 shows the change in mean intensity for clouds with $A_V = 6$ mag along the z-axis, for 1040 and 2980Å. Again, the cloud is darker inside at 1040Å than at 2980Å; because of the greater optical depth, the relative intensity drops by over three orders of magnitude to the centre at 1040Å. The greater optical depth is also responsible for the increased unevenness in the contours compared with the $A_V = 1$ mag clouds. A finer grid would need to be used in the radiative transfer model to maintain accuracy.

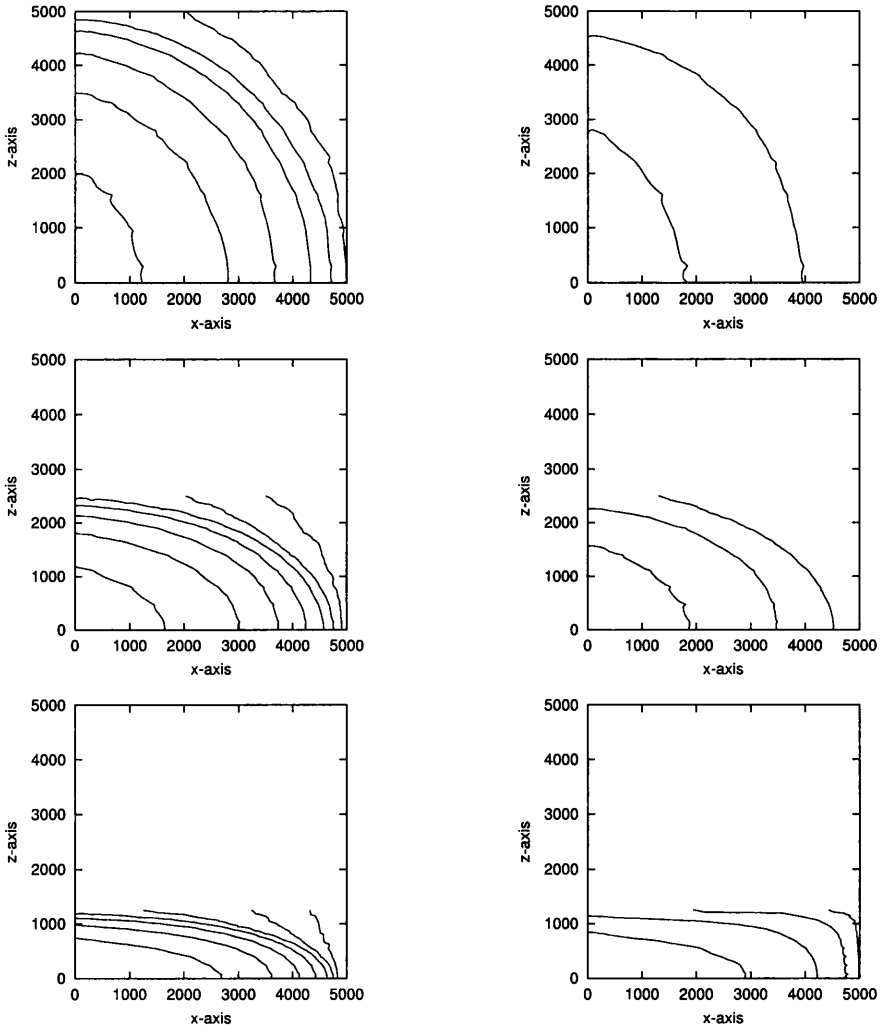

Figure 3.5: Contour maps of the mean intensity relative to incident intensity (J/J_0) inside clouds with total A_V (along z-axis) of 1.0 mag. The shape parameter of the clouds is $\zeta = 1.0, 0.5, 0.25$, by row from the top, and the two columns show intensities at wavelengths 1040Å on the left and 2980Å on the right. Contour levels are (from the outside, $x = 5000$) at: 0.8, 0.7, 0.6, 0.5, 0.4, 0.3, 0.2; though not all the lower (inner) levels are reached in all cases, particularly at 2980Å.

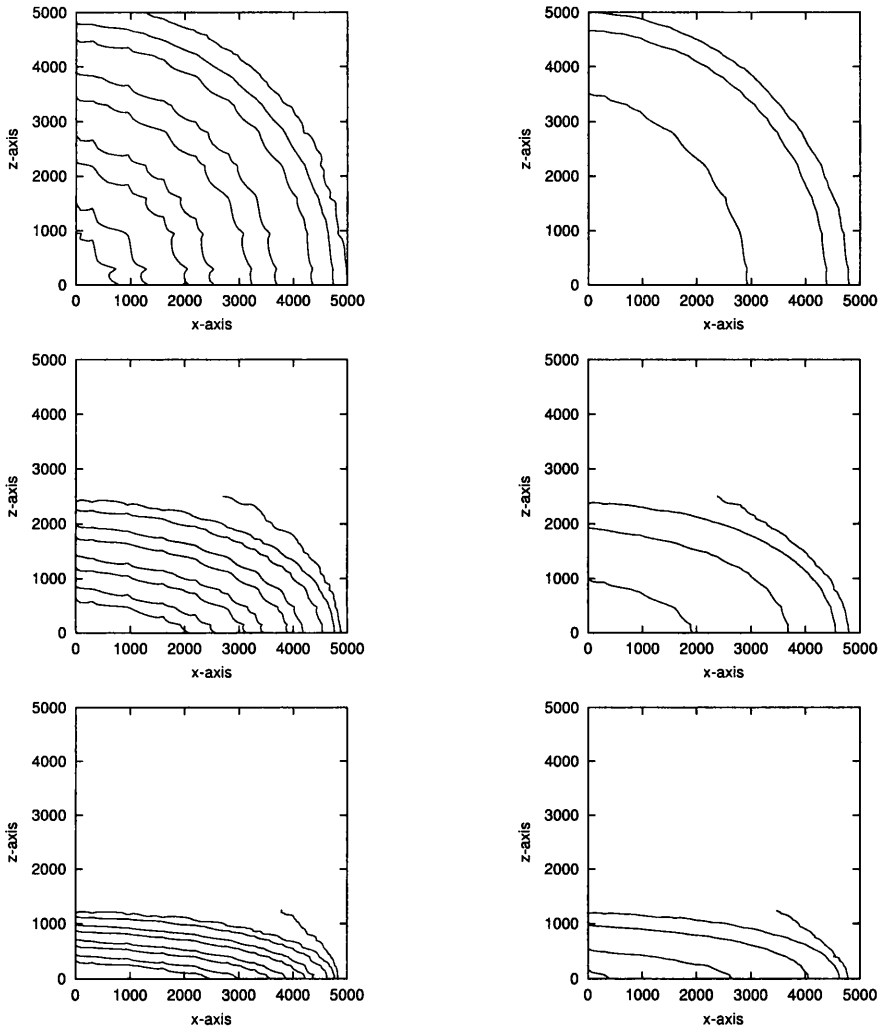

Figure 3.6: Contour maps of the mean intensity relative to incident intensity (J/J_0) inside clouds with total A_V (along z-axis) of 6.0 mag. The shape parameter of the clouds is $\zeta = 1.0, 0.5, 0.25$, by row from the top, and the left and right columns show the intensities at wavelengths 1040Å and 2980Å respectively. Contours are (from the outside) at: 0.7, 0.5, 0.2, 0.05, 0.02, 0.005, 0.002, 0.0005, 0.0002; but many of the inner contours are not reached for 2980Å.

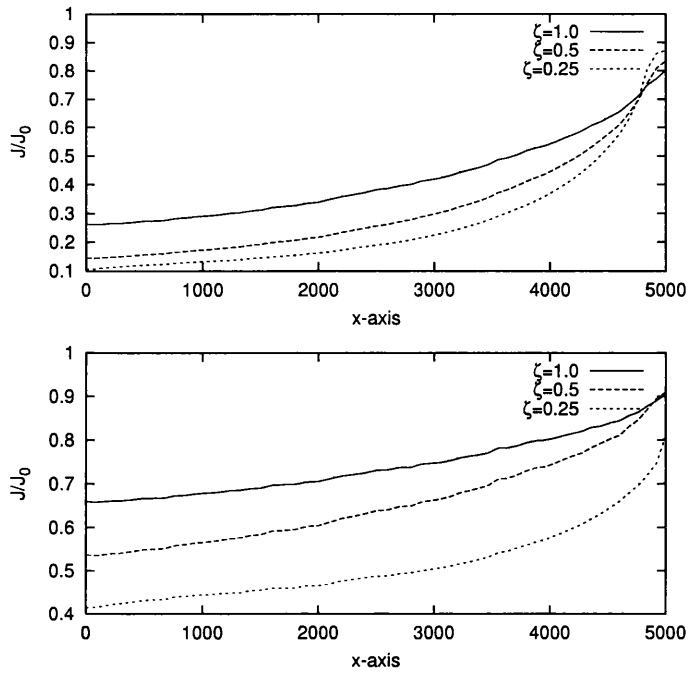

Figure 3.7: Mean intensity relative to incident intensity (J/J_0) along the x-axis in a cloud with total A_V (along z-axis) of 1.0 mag. The upper plot is for 1040Å, and the lower for 2980Å.

3.2.2.3 Magnitude of effect

The amount of darkening can be more clearly estimated if we examine the mean intensities along the x-axis, as shown in Figures 3.7 and 3.8.

Figure 3.7 shows the mean intensities in the 1.0 mag clouds for 1040 and 2980Å respectively. The intensities are, of course, higher for 2980Å than for 1040Å. They both show, however, that as the cloud collapses (ζ decreases) the field is significantly darkened over most of the central plane.

Figure 3.8 shows the relative intensity in the central plane for the thicker clouds ($A_V = 6$ mag). The effect is similar to that of the thin clouds, but because the intensity falls so low towards the centre of the clouds, the darkening due to collapse is most noticeable in the outer regions.

On many of these graphs the intensity just outside the cloud (4800–5000) can be seen to increase as the cloud collapses. This is simply because, with a smaller cloud, a point outside has a larger unobstructed view of the UV background.

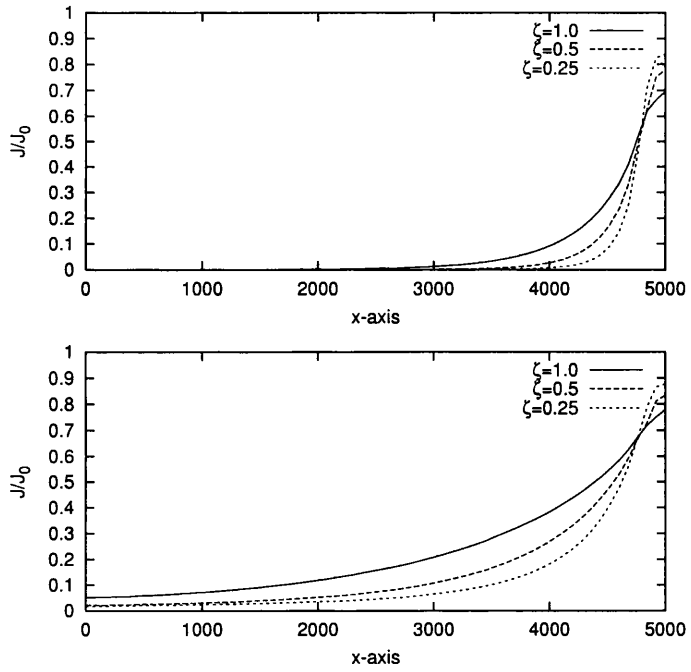

Figure 3.8: Mean intensity relative to incident intensity (J/J_0) along the x-axis in a cloud with total A_V (along z-axis) of 6.0 mag. The upper plot is for 1040Å, and the lower for 2980Å.

3.3 Chemistry inside spheroidal clouds

We model the gas phase chemistry inside the clouds using the multipoint model described in Section 2.3. The position of points at which we obtain chemical abundances are shown in Figure 2.8 for the spherical case. The positions for the clouds with $\zeta \neq 1$ are equivalent but with the z coordinates scaled by ζ.

The chemistry at each point is based on the UMIST database (Millar et al. 1997) using a reduced species set of 212 species. In particular, we have omitted all molecules containing P, Si, Cl, Fe, Mg or with more than four carbon atoms. The reactions are all as presented in the UMIST rate file with the exception of the interstellar UV photoreactions which are calculated using the radiation field previously obtained. Most of the photoreactions are modelled with approximate cross-sections as described in Section 1.3.3.2: using a flat cross-section with a cut-off determined from the interstellar extinction curve. We have also obtained genuine cross-section data for a small number of reactions. Most important is probably the photoionization of C atoms since C^+ dominates the ionization fraction.

The initial abundances used are the same as for the models described in Section 1.2.3.1, although in these models we do not have any freeze-out reactions. The cosmic-ray ionization rate is the same also, at $1.3 \times 10^{-17}\,s^{-1}$. The temperature is taken to be 10 K throughout, and, for reference, we summarize the densities used in Table 3.1.

3.3.1 How chemistry changes with collapse

We use the 'flattened sphere' models as an example of some of the effects of an axial collapse. In this section we will examine the chemistry by reference to the steady-state

ζ	τ_z			
	0.5	1.0	3.0	5.0
1.0	100	100	300	1000
0.5	200	200	600	2000
0.25	400	400	1200	4000

Table 3.1: Gas number densities (in cm^{-3}) for cloud models with τ_z mag of visual extinction along the z-axis to the centre, and shape parameter ζ.

abundances of C^+ and CS.

3.3.1.1 Explanation of the graphs and tables

Vertical-column graphs These graphs show the column density of species through the cloud. The columns are parallel to the z-axis at increasing xy-radius. Note that since the total gas columns parallel to the z-axis do not change with ζ, any difference between clouds in these graphs is caused by the differing chemistries.

Central-plane abundance graphs These graphs plot the fractional abundance (relative to H-nuclei) along the x-axis of the cloud. That is, in the central plane, increasing with radius. These values contribute to the vertical columns above.

Perpendicular-column tables In the tables that appear later we present the column densities through the clouds along both the z-axis (N^z: the 'vertical column' from above) and the x-axis (N^x). The overall gas column on any line through the cloud centre is equal to that along the z-axis for $\zeta = 1$, but all except N^z increase as ζ decreases. The increase is most pronounced in the xy-plane, where the column is increased by $1/\zeta$. The N^z and N^x columns represent therefore the minimum and maximum columns through the centre of the cloud.

3.3.1.2 C^+ ions

In Figure 3.9 we present the fractional abundance in the central plane of the $A_V(z) = 1$, 6 clouds. At the edge of all the clouds the abundance is very high, falling off towards the centre. In the $A_V = 6$ clouds, of course, the abundance falls to much lower levels than in the $A_V = 1$ clouds, which conceals the change which occurs as a result of flattening.

In the more flattened clouds, as shown earlier, the UV radiation field is less intense and hence the carbon ionization level is lower. This is most pronounced in the low optical depth clouds, but is also easily seen in the outer regions of the thicker clouds. In both cases the fractional abundance drops by a factor of around two between the spherical and quarter-height ($\zeta = 0.25$) clouds.

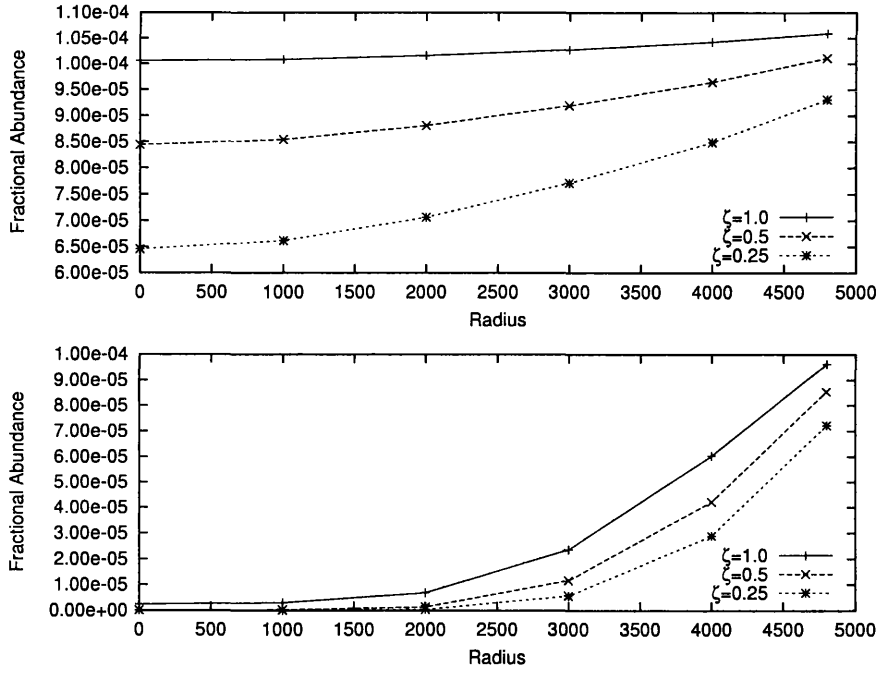

Figure 3.9: The fractional abundance of C^+ in the central plane of the flattened sphere models. The upper graph shows the abundances in the family of clouds with total A_V (along z-axis) 1.0 mag while the lower has $A_V = 6.0$ mag. Each family consists of the three spheroids with $\zeta = 1, 0.5, 0.25$ corresponding to increasing flattening.

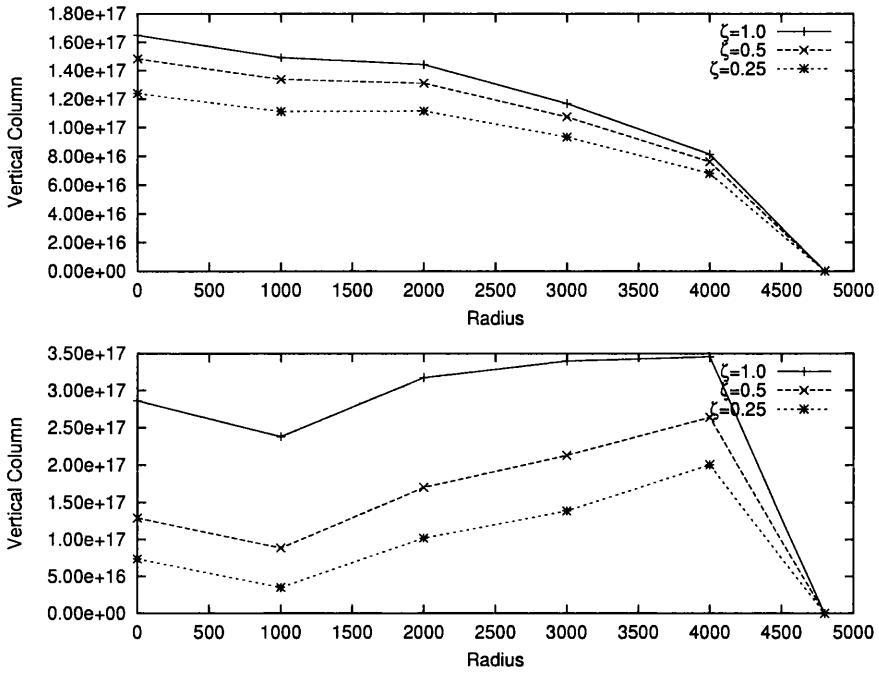

Figure 3.10: The vertical column density of C^+ through the flattened sphere models. The upper graph shows the family of clouds with total A_V (along z-axis) of 1.0 mag; the lower: 6.0 mag.

In Figure 3.10 we show the vertical column densities for C^+ corresponding to the abundances in Figure 3.9. As expected the columns in both families decrease as the clouds are flattened. In this case the effect is most pronounced in the high optical depth case. The column density of C^+ in those clouds is probably largely due to the outer regions of the clouds, the abundance being very low in the centre.

The peculiar radial dependence of the C^+ column in the $A_V = 6$ case—peaking in the outer regions and dipping off-centre—can be explained by the combination of total gas column density increasing towards the centre, and abundance of the ion falling off and then remaining low in the region around the centre.

3.3.1.3 The CS molecule

In Figure 3.11 we present the fractional abundance of CS in the central plane of the $A_V(z) = 1$, 6 clouds. Unlike C^+, CS is destroyed by ultraviolet radiation (and in reactions with ions), so its behaviour is largely the opposite. CS needs shielding from

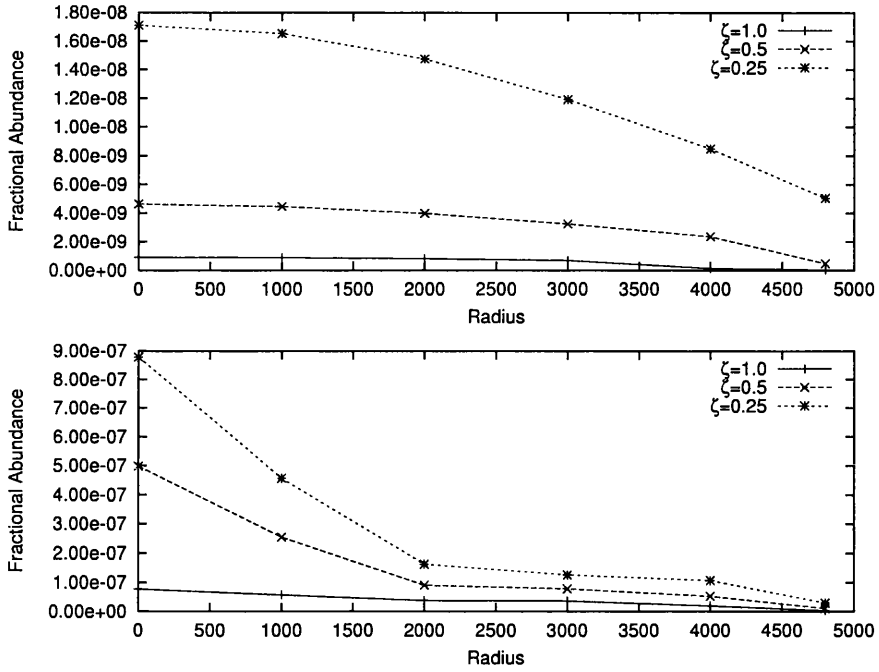

Figure 3.11: The fractional abundance of CS in the central plane of the flattened sphere models. The upper graph shows the abundances in the family of clouds with total A_V (along z-axis) 1.0 mag while the lower has $A_V = 6.0$ mag. Each family consists of the three spheroids with $\zeta = 1, 0.5, 0.25$ corresponding to increasing flattening.

the incident interstellar ultraviolet to be produced in any quantity. The abundances are low for all the low optical depth clouds, and even in the 6 mag case the spherical cloud also produces only low abundance.

However, the effect of flattening is quite pronounced, raising the abundance by at least an order of magnitude between the spherical and most flattened case. For the high optical depth clouds the abundance rises dramatically in the central region, suggesting that a minimum level of shielding is required before CS can become plentiful.

In Figure 3.12 we show the vertical column densities for CS corresponding to the abundances in Figure 3.11. The column density increases with flattening in a predictable manner. For both thickness of clouds the column density through the centre increases by about an order of magnitude between $\zeta = 1$ and $\zeta = 0.25$. In the case of the thin clouds this could potentially make the difference between an unobservable and observable level. (However, we cannot consider comparison with actual observations because these models do not include freeze-out onto dust grains. It was shown

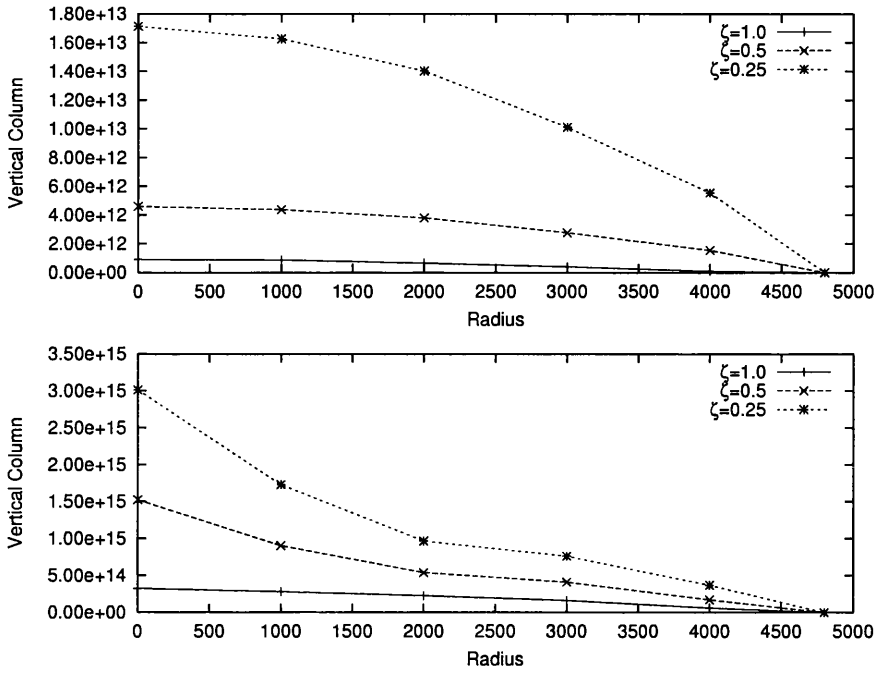

Figure 3.12: The vertical column density of CS through the flattened sphere models. The upper graph shows the family of clouds with total A_V (along z-axis) of 1.0 mag; the lower: 6.0 mag.

in Section 1.2.3 that interactions with the dust may dominate the abundance of this species.)

3.3.1.4 Overall effect

For neither C^+ nor CS shown above is the effect of flattening especially large in absolute terms. However, they do demonstrate the flavour of an axisymmetric collapse: the effect on the chemistry due to darkening as a result of changing shape occurs over a region around the central plane of the cloud, extending through much of the cloud's xy-radius.

To illustrate the general effect on the chemistry, in Tables 3.2 to 3.4 we show the column densities along both the x and z-axes for a variety of species.

Table 3.2 shows the two column densities for the spherical models. In principle, for the spherical case, both columns should be equal. The discrepancy between them, as seen in this table, is a result of the inaccuracy in the radiative transfer. The resulting

Species	$\tau_z = 1.0$		$\tau_z = 6.0$		$\tau_z = 10.0$	
	N^z	N^x	N^z	N^x	N^z	N^x
H_2	7.8(20)	7.8(20)	4.8(21)	4.8(21)	8.0(21)	8.0(21)
CO	3.8(13)	4.1(13)	1.8(16)	2.1(16)	6.4(17)	6.9(17)
C^+	1.6(17)	1.6(17)	2.8(17)	2.5(17)	1.7(17)	1.5(17)
e^-	1.9(17)	1.9(17)	4.0(17)	3.7(17)	2.9(17)	2.6(17)
CH	5.3(13)	5.5(13)	3.4(14)	3.2(14)	3.7(14)	3.4(14)
CH_3	9.2(10)	9.4(10)	1.2(12)	1.2(12)	1.2(12)	1.2(12)
CH_3OH	3.2(5)	3.5(5)	1.0(10)	1.2(10)	5.0(12)	4.8(12)
C_2H	2.5(12)	2.6(12)	2.6(13)	2.5(13)	2.8(13)	2.5(13)
C_2H_2	1.3(10)	1.4(10)	1.1(12)	1.2(12)	1.9(12)	1.9(12)
C_3H_2	2.0(10)	2.2(10)	1.2(12)	1.3(12)	1.8(12)	1.7(12)
H_2CO	5.1(9)	5.5(9)	1.8(12)	2.0(12)	2.0(13)	2.1(13)
CS	9.0(11)	9.9(11)	3.3(14)	3.8(14)	2.3(16)	2.6(16)
S	2.1(14)	2.2(14)	8.2(15)	9.1(15)	6.7(16)	6.8(16)
S^+	2.1(16)	2.1(16)	1.2(17)	1.2(17)	1.1(17)	1.0(17)
SO	6.1(9)	6.6(9)	5.7(12)	6.5(12)	5.5(15)	7.0(15)
H_2S	8.8(7)	9.4(7)	1.9(10)	2.1(10)	1.3(12)	1.6(12)
H_2S^+	9.9(8)	1.0(9)	2.7(10)	2.9(10)	6.0(10)	5.9(10)
NH	4.9(10)	5.1(10)	6.7(12)	7.6(12)	4.6(12)	4.5(12)
NH_3	3.3(7)	3.5(7)	6.4(11)	7.5(11)	4.6(13)	5.7(13)
HCO	4.6(8)	4.7(8)	7.7(9)	7.8(9)	1.6(10)	1.7(10)
HCN	2.6(9)	2.8(9)	9.2(11)	1.1(12)	5.6(12)	5.5(12)
HNC	2.4(9)	2.6(9)	1.5(12)	1.8(12)	8.8(12)	9.1(12)
CN	6.8(10)	7.6(10)	6.8(13)	7.8(13)	1.7(14)	1.6(14)
H_2O	8.3(11)	8.6(11)	5.1(14)	5.9(14)	4.4(16)	4.9(16)
OH	6.2(12)	6.4(12)	4.1(14)	4.5(14)	2.5(15)	2.7(15)
H_3^+	4.8(12)	4.8(12)	4.1(13)	4.4(13)	6.9(13)	7.3(13)
H_3O^+	2.0(9)	2.0(9)	1.6(11)	1.8(11)	4.6(12)	5.6(12)

Table 3.2: Column densities along the x and z axes for the spherical cloud models with τ_z mag of visual extinction along the z-axis.

Species	$\zeta = 1.0$		$\zeta = 0.5$		$\zeta = 0.25$	
	N^z	N^x	N^z	N^x	N^z	N^x
H_2	7.8(20)	7.8(20)	7.9(20)	1.6(21)	7.9(20)	3.2(21)
CO	3.8(13)	4.1(13)	1.3(14)	3.1(14)	3.9(14)	1.8(15)
C^+	1.6(17)	1.6(17)	1.5(17)	2.9(17)	1.2(17)	4.8(17)
e^-	1.9(17)	1.9(17)	1.7(17)	3.3(17)	1.5(17)	5.6(17)
CH	5.3(13)	5.5(13)	8.6(13)	1.8(14)	1.1(14)	4.7(14)
CH_3	9.2(10)	9.4(10)	1.3(11)	2.7(11)	1.5(11)	6.4(11)
CH_3OH	3.2(5)	3.5(5)	5.2(5)	1.2(6)	7.3(5)	3.4(6)
C_2H	2.5(12)	2.6(12)	6.1(12)	1.3(13)	9.7(12)	4.3(13)
C_2H_2	1.3(10)	1.4(10)	5.2(10)	1.2(11)	1.4(11)	6.6(11)
C_3H_2	2.0(10)	2.2(10)	8.9(10)	2.1(11)	2.3(11)	1.1(12)
H_2CO	5.1(9)	5.5(9)	1.3(10)	2.8(10)	2.4(10)	1.0(11)
CS	9.0(11)	9.9(11)	4.6(12)	1.1(13)	1.7(13)	8.2(13)
S	2.1(14)	2.2(14)	3.2(14)	6.8(14)	4.1(14)	1.7(15)
S^+	2.1(16)	2.1(16)	2.0(16)	4.1(16)	2.0(16)	8.1(16)
SO	6.1(9)	6.6(9)	2.5(10)	5.7(10)	7.3(10)	3.4(11)
H_2S	8.8(7)	9.4(7)	2.0(8)	4.4(8)	3.8(8)	1.7(9)
H_2S^+	9.9(8)	1.0(9)	1.1(9)	2.3(9)	1.3(9)	5.5(9)
NH	4.9(10)	5.1(10)	3.8(10)	8.0(10)	2.6(10)	1.1(11)
NH_3	3.3(7)	3.5(7)	3.8(7)	8.4(7)	4.2(7)	1.9(8)
HCO	4.6(8)	4.7(8)	7.5(8)	1.6(9)	1.1(9)	4.7(9)
HCN	2.6(9)	2.8(9)	4.6(9)	1.0(10)	6.8(9)	3.0(10)
HNC	2.4(9)	2.6(9)	3.8(9)	8.3(9)	5.0(9)	2.2(10)
CN	6.8(10)	7.6(10)	2.9(11)	6.8(11)	8.6(11)	3.9(12)
H_2O	8.3(11)	8.6(11)	7.5(11)	1.6(12)	6.6(11)	2.9(12)
OH	6.2(12)	6.4(12)	5.3(12)	1.1(13)	4.3(12)	1.8(13)
H_3^+	4.8(12)	4.8(12)	2.7(12)	5.6(12)	1.6(12)	6.7(12)
H_3O^+	2.0(9)	2.0(9)	1.3(9)	2.7(9)	9.5(8)	4.1(9)

Table 3.3: Column densities along the x and z axes for the spheroidal cloud models with 1 mag of visual extinction along the z-axis.

error for these models seems to be in the second significant digit. If more exact values were needed then the radiative transfer model used would need to have finer grids, and be tailored more closely to the different cloud conditions.

Tables 3.3 and 3.4 show the column densities for the 1 mag and 6 magcloud families. It must be remembered when examining these tables that the overall N^x column density increases with decreasing ζ. To examine the effect of collapse on the chemistry it is best to compare the N^z columns. Such effects generally seem to be fairly small. For the low optical depth cloud (Table 3.3), by comparing $N^z(\zeta = 1)$ with $N^z(\zeta = 0.25)$, CS seems to show more sensitivity to the flattening than the other species presented. In the higher optical depth case CS seems less special: other species,

Species	$\zeta = 1.0$		$\zeta = 0.5$		$\zeta = 0.25$	
	N^z	N^x	N^z	N^x	N^z	N^x
H_2	4.8(21)	4.8(21)	4.8(21)	9.6(21)	4.8(21)	1.9(22)
CO	1.8(16)	2.1(16)	8.9(16)	1.5(17)	1.6(17)	5.0(17)
C^+	2.8(17)	2.5(17)	1.3(17)	3.4(17)	7.4(16)	4.9(17)
e^-	4.0(17)	3.7(17)	2.3(17)	5.5(17)	1.5(17)	8.6(17)
CH	3.4(14)	3.2(14)	2.5(14)	6.2(14)	1.9(14)	1.2(15)
CH_3	1.2(12)	1.2(12)	1.0(12)	2.1(12)	7.8(11)	3.5(12)
CH_3OH	1.0(10)	1.2(10)	3.1(11)	4.8(11)	7.3(11)	2.1(12)
C_2H	2.6(13)	2.5(13)	1.7(13)	4.8(13)	1.1(13)	9.0(13)
C_2H_2	1.1(12)	1.2(12)	1.0(12)	2.8(12)	8.6(11)	6.1(12)
C_3H_2	1.2(12)	1.3(12)	1.0(12)	2.9(12)	7.5(11)	6.2(12)
H_2CO	1.8(12)	2.0(12)	5.4(12)	8.6(12)	6.5(12)	1.9(13)
CS	3.3(14)	3.8(14)	1.5(15)	2.9(15)	3.0(15)	1.0(16)
S	8.2(15)	9.1(15)	2.9(16)	4.5(16)	4.5(16)	1.3(17)
S^+	1.2(17)	1.2(17)	9.5(16)	2.0(17)	7.7(16)	3.6(17)
SO	5.7(12)	6.5(12)	1.9(13)	3.2(13)	2.6(13)	7.9(13)
H_2S	1.9(10)	2.1(10)	6.1(10)	9.9(10)	1.0(11)	3.0(11)
H_2S^+	2.7(10)	2.9(10)	4.1(10)	7.1(10)	4.6(10)	1.6(11)
NH	6.7(12)	7.6(12)	7.0(12)	9.9(12)	3.7(12)	9.5(12)
NH_3	6.4(11)	7.5(11)	1.9(12)	2.6(12)	1.8(12)	4.3(12)
HCO	7.7(9)	7.8(9)	8.5(9)	1.9(10)	9.4(9)	4.4(10)
HCN	9.2(11)	1.1(12)	1.9(12)	3.0(12)	2.6(12)	7.3(12)
HNC	1.5(12)	1.8(12)	4.0(12)	5.9(12)	3.9(12)	1.0(13)
CN	6.8(13)	7.8(13)	1.4(14)	2.1(14)	1.2(14)	3.3(14)
H_2O	5.1(14)	5.9(14)	3.3(15)	4.9(15)	5.3(15)	1.4(16)
OH	4.1(14)	4.5(14)	5.6(14)	8.7(14)	4.3(14)	1.2(15)
H_3^+	4.1(13)	4.4(13)	3.6(13)	6.1(13)	2.4(13)	7.6(13)
H_3O^+	1.6(11)	1.8(11)	2.5(11)	4.0(11)	2.3(11)	6.5(11)

Table 3.4: Column densities along the x and z axes for the spheroidal clouds with 5 mag of visual extinction to the centre along the z-axis.

such as H_2O show comparable changes.

More realistic models? In a realistic collapse model the effects might well be larger. Some compaction in the xy direction would increase the density further, and we do not expect, in general, that clouds will collapse in a smooth manner, maintaining constant density throughout. Most likely, different regions will behave differently during collapse and more complicated structures will emerge than presented here. Such structures may well have a more variable chemistry than the simple, static models tested here.

Furthermore, we have presented steady-state results for each of these clouds because to associate clouds of each family otherwise requires a full collapse model, including the time taken to transition from one to the next. It may be that the 'early-time' chemistry would be more susceptible to changes in the cloud shape.

3.4 Effects of chemistry on cloud shape

If a region of the interstellar medium has well ordered magnetic fields providing support against gravitational collapse then the evolution of its shape will depend on the chemistry through the ionization fraction

As already mentioned, the ions provide general support across the direction of the field lines by collision with other species in the gas. The efficiency with which they can do this depends directly on the relative abundance of ions to neutral species.

Gammie & Ostriker (1996) showed that non-linear hydrodynamic waves can provide support in the other direction, along the field lines. However, the damping rate of these waves is inversely proportional to the number density of ions. When the ionization is too high the waves will be damped too quickly for support to continue.

Thus the chemistry in the cloud influences the rate of collapse in two directions separately, determining how the density structure will evolve. Through the effect of density structure on the chemistry this provides a feedback mechanism whereby a change of shape might 'regulate' itself: A cloud without support from Alfvén waves could collapse along the field lines to a point where the ionization fraction drops far enough for the Alfvén waves to become important and for the collapse to continue across the field lines by ambipolar diffusion. We could use our flattened sphere models for a simple examination of the first stage of such a collapse.

Ruffle et al. (1998) considered the fractional ionization in a 1D case with regard to the apparent association found by Williams et al. (1995) of star-forming clumps with a critical column density of CO They showed that the fractional ionization, and hence magnetic support, of a 1D clump would diminish significantly when the radial visual extinction was about 2.5 mag. (The ionization fraction drops steeply—about an order of magnitude—between A_V 2–3.) We will attempt to relate this critical level of extinction (A_V^c) to our models, bearing in mind that the effective level of shielding is less than for the same optical depth inside a slab.

Figure 3.13 shows the ionization fraction in the central plane of our models. The magnitude of the effect flattening has on the ionization fraction is generally small for these models. How might the results be interpreted?

Considering the extreme cases first: much of the interior of the thickest cloud

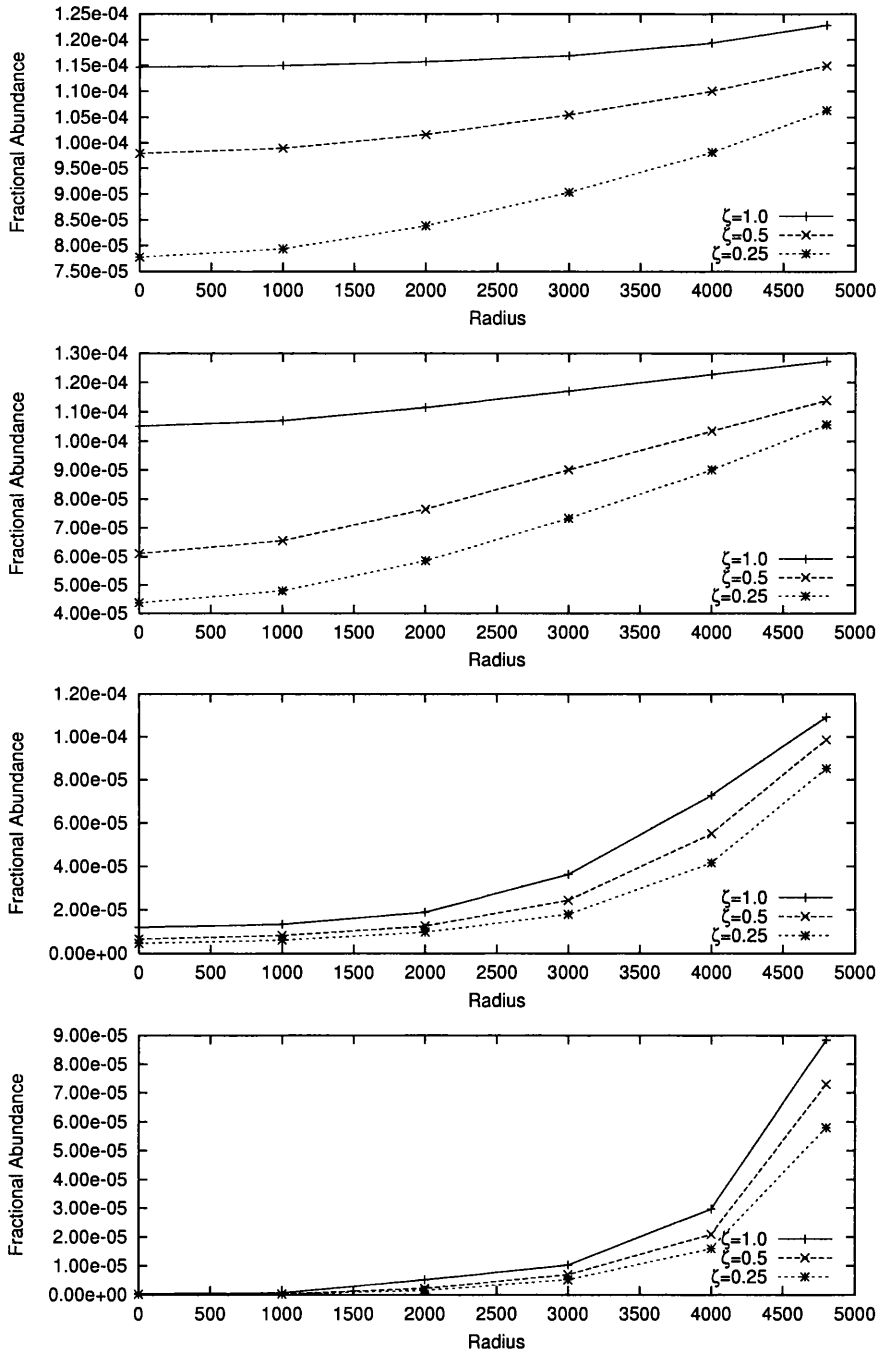

Figure 3.13: The fractional abundance of ions in the central plane of clouds with total A_V (along z-axis) of 1.0, 2.0, 6.0 and 10.0 mag from top plot down.

(5 mag radially) is already well above the level of shielding present at 2.5 mag into a slab-shaped cloud. The decrease in ionization fraction that occurs as a result of the flattening is small compared to the decrease with depth into the cloud. So it appears that the collapse rate of such a cloud will not be very sensitive to changes in its shape.

For the thinnest cloud (0.5 mag radially) the decrease in ionization fraction with flattening is small. However, at $\zeta = 0.25$ the extinction along the x-axis to the centre is still only 2 mag, so we would not expect a large drop in the ionization. This cloud would also keep collapsing in the same manner.

The 2 mag diameter sphere collapses to give a radial extinction of 4 mag in the xy-plane. The level of extinction in the central region of the cloud changes from well below A_V^c when spherical to become comparable for $\zeta = 0.25$. We can see the ionization fraction drop by half an order of magnitude for the central region; so perhaps a slightly larger sphere undergoing this degree of flattening would pass through the critical point and reach a level of ionization where Alfvén waves can provide support, halting the flattening.

Indeed, these results could be taken as tentatively suggesting a relation between the initial optical thickness and the degree of flattening whereby the thinner the initial sphere, the more flattening will be undergone before Alfvén waves can provide support.

The case of the 6 mag diameter sphere is significantly more complicated. With 3 mag of extinction to the centre the centre of this cloud has a level of shielding close to that at A_V^c. The ionization fraction drops by an order of magnitude over the radius of the sphere. So clouds of this size may have Alfvén wave support in their centre but not elsewhere. A hand-waving argument could be made to suggest that flattening may help the Alfvén wave supported region to grow, but what seems clear is that this depth cloud does not fall cleanly into either the sub-critical or super-critical categories and that modelling its collapse will require a proper, two-dimensional, magneto-hydrodynamic (MHD) model.

3.4.1 Conclusion

Overall, we suggest that the modelling techniques used in this chapter do provide an important alternative to approximating complex clouds with plane-parallel models.

Although the model results presented here do not show very large effects on the chemistry due to flattening, they suggest that other cases with low optical depths ($\tau_c < 3$) warrant further investigation with regard to possible effects on the dynamical support mechanisms. Furthermore, the use of more realistic models, in particular with inhomogeneous density structures, may well exaggerate the chemical changes such that species such as CS can be used to interpret observational data.

Bibliography

Bhattal, A. S., Francis, N., Watkins, S. J. & Whitworth, A. P. (1998), 'Dynamically triggered star formation in giant molecular clouds', *Mon. Not. Roy. Astron. Soc.* **297**, 435.

Draine, B. T. (1978), 'Photoelectric heating of interstellar gas.', *Astrophys. J. Sup.* **36**, 595–619.

Draine, B. T. & Lee, H. M. (1984), 'Optical properties of interstellar graphite and silicate grains', *Astrophys. J.* **285**, 89.

Gammie, T. F. & Ostriker, E. C. (1996), 'Can nonlinear hydromagnetic waves support a self-gravitating cloud?', *Astrophys. J.* **466**, 814.

Goldsmith, P. F. & Arquilla, R. (1985), Rotation in dark clouds, *in* D. C. Black & M. S. Matthews, eds, 'Protostars and Planets II', University of Arizona Press, p. 137.

Jenkins, E. B. & Savage, B. D. (1974), 'Ultraviolet photometry from the orbiting astronomical observatory. XIV. An extension of the survey of Lyman-α absorption from interstellar hydrogen', *Astrophys. J.* **187**, 243–255.

Millar, T., Farquhar, P. & Willacy, K. (1997), 'The UMIST database for astrochemistry 1995', *Astron. & Astrophys. Sup.* **121**, 139–185.

Mouschovias, T. (1987), *in* G. E. Morfill & M. Scholer, eds, 'Physical Processes in Interstellar Clouds', D. Reidel Publishing Company.

Roberge, W. G., Jones, D., Lepp, S. & Dalgarno, A. (1991), 'Interstellar photodissociation and photoionization rates.', *Astrophys. J. Sup.* **77**, 287–297.

Ruffle, D. P., Hartquist, T. W., Rawlings, J. M. C. & Williams, D. A. (1998), 'Ionization structure and a critical visual extinction for turbulent supported clumps.', *Astron. & Astrophys.* **334**, 678–684.

Shu, F. H. (1977), 'Self-similar collapse of isothermal spheres and star formation', *Astrophys. J.* **214**, 488.

van Dishoeck, E. & Black, J. H. (1982), 'The excitation of interstellar C_2', *Astrophys. J.* **258**, 533.

van Dishoeck, E. F. (1988), Photodissociation and photoionization processes., *in* T. J. Millar & D. A. Williams, eds, 'Rate Coefficients in Astrochemistry', Kluwer Academic Publishers, pp. 49–72. Proceedings of a conference held at UMIST.

Vrba, F. J., Strom, S. E. & Strom, K. M. (1976), 'Magnetic field structure in the vicinity of five dark cloud complexes.', *Astron. J.* **81**, 958–969.

Williams, J. P., Blitz, L. & Stark, A. A. (1995), 'The density structure in the Rosette Molecular Cloud: Signposts of evolution', *Astrophys. J.* **451**, 252.

Zuckerman, B. & Palmer, P. (1974), 'Radio radiation from interstellar molecules.', *Ann. Rev. Astron. Astrophys.* **12**, 279–313.

Chapter 4

Dust grains

In which the dust properties are discussed and a method for evaluating the electric charge is described. The basic behaviour of the grain charge in simple cloud shapes is evaluated. The charge in the spheroidal clouds is also calculated, and the implications for grain surface chemistry are discussed.

4.1 Introduction

The importance of dust grains in the interstellar medium has already been illustrated with regard to the radiation field and gas phase chemistry. Let us recap the ways in which dust interacts with the gas.

4.1.1 Optical properties

The optical properties of the dust determine how well ultraviolet radiation can penetrate clouds in the interstellar medium. In Section 2.2 we saw that although small changes in the dust's optical properties are of low significance the overall character (highly reflective or absorbing, forward or backward scattering) can make quite a difference to the radiation field inside a cloud.

Unfortunately calculating the way in which a dust grain interacts with radiation is intrinsically complicated, depending on the size, shape and composition of the dust

grain. Typically dust grains are modelled as spheres, often of two materials arranged as an inner kernel and an outer mantle with different refractive indices. The behaviour of such a grain can be evaluated relatively easily. However, the exact nature of the grains in the interstellar medium is still uncertain and the effect of the grain population as a whole depends strongly on the size distribution.

Modelling the optical properties of the dust grain population from first principles remains difficult and there are more free parameters than observational constraints.

Changing the properties Another complication is the idea that the dust may evolve through time (Cecchi-Pestellini & Williams 1998). The ultraviolet field incident on the dust grains may, over time, help to alter the nature of the dust material, changing the refractive index and hence the overall optical properties. Depending on the time-scale for this process this may add an additional time-dependence to the collapsing cloud problem of Chapter 3, wherein the changing shape alters the radiation field which in turn may alter the propagation of radiation.

4.1.2 Surface properties

Gas phase species collide with the dust grains and thereby alter the nature of the gas phase chemistry. Even if atoms and molecules merely stick to the grains and remain inert then this 'freeze out' process dramatically alters the gas phase over time, as we saw in Section 1.1.3.

In Section 1.2 we discussed the possibility of surface reactions on the dust grains. If such reactions are followed by ejection of species from the surface then the dust grains can contribute to the gas phase chemistry directly, and the simple models explored in Section 1.2.3 showed that these contributions may be significant.

The composition of the dust grains will be important in these processes, for example, in determining how tightly bound incident species will become. Again, however, the size distribution is critical. The grain size not only determines the cross-section and hence likelihood of impact for species, but also the surface area of the grains. The surface area determines how many molecules may be available on each dust grain which will be important for any reactions where one or both reactants are mobile. In fact, for

small grains, the number of molecules available on the surface of an individual grain can be so low that it seems there may be no analytical way to model these processes and stochastic techniques may be necessary (Caselli et al. 1998, Green et al. 2001).

Changing the properties The accumulation of gas phase species on the surface of dust grains will affect their properties. For large grains the change in optical properties may well not be significant, but the incident species do significantly affect the electric charge of the dust grains. The electric charge of each grain influences the rate of accretion of ions from the gas as described in Section 1.2, and it is also very sensitive to the size of the grain.

However, in addition to the assumptions about the dust needed to model the radiation and chemistry in the interstellar medium, the results of both models are needed to evaluate the grain charge. In the next section we will describe one method for calculating the charge distribution of dust grains.

4.1.3 Grain charge

The electric charge on a dust grain in the interstellar medium is influenced by both the gas phase chemistry, through collisions with ions and electrons, and by the ultraviolet radiation field through the photoelectric effect. Taylor et al. (1991) calculated the grain charge distribution for two basic kinds of dust, using a simple chemistry in a plane-parallel cloud, approximating the decline in photoelectric charging with depth by a decaying exponential. Using the chemical and radiation models presented in earlier chapters we can re-evaluate the charge distributions and examine non-planar clouds. In the rest of this section we present the method of calculation.

4.1.3.1 Collisional contribution

The collisional charging rate, $\dot{Z}_g^c$ of a dust grain is the sum of the charging rates due to all the gas phase species, X:

$$\dot{Z}_g^c = \sum_X Z_X A_X^c S_X, \tag{4.1}$$

where Z_X is the electric charge of species X, here measured in units of positive electron charges. A_X^c is the rate of collision of species X with the dust grain and S_X is the sticking probability. If there is any factor in S_X which depends on the impact velocity or any variable other than the species identity then it can be subsumed by the grain's effective cross-section to species X: σ_X, used to calculate the collision rate.

The number of particles of species X hitting a grain per second is:

$$A_X^c = \int_0^\infty \sigma_X v_X n_X p(v_X)\, dv, \tag{4.2}$$

where n_X is the number density of species X, and the velocities, v_X, are distributed according to $p(v)$.

The effective cross-section, σ_X, depends on the average geometric cross-section and the interaction potential between the grain and the incident ion. Thus the current grain charge and the velocity of the ion both influence the cross-section. To evaluate further we need to make some assumptions.

Velocity distribution Dropping the subscript X, we shall take the gas velocities to follow a Maxwell distribution:

$$p(v)\, dv = 4\pi v^2 \left(\frac{m}{2\pi kT}\right)^{3/2} e^{-mv^2/2kT}\, dv \tag{4.3}$$

where m is the mass of the species, k is the Boltzmann constant, and T the gas temperature (which may also vary with species X). Then, in terms of

$$u = \frac{mv^2}{2kT} \tag{4.4}$$

the collision rate can be written as:

$$A^c = \sqrt{\frac{8kT}{\pi m}}\, n \int_0^\infty \sigma u e^{-u}\, du \tag{4.5}$$

Grain cross-section For spherical dust grains, Spitzer (1978) gives the expression below for the effective cross-section:

$$\sigma_X = \sigma_{\text{geometric}} \left(1 - \frac{2Z_X e U_g}{m_X v_X^2}\right), \tag{4.6}$$

where the geometric cross-section is, of course, πa^2 for spherical grains with radius a. The other factor accounts for the reduction or increase due to the grain potential, $U_g = Z_g e/a$, (in e.s.u.). This factor is only appropriate when $mv^2 > 2Z_X e U_g$; otherwise the incident ion does not have sufficient energy to overcome the Coulomb repulsion and the effective cross-section is zero. The cut-off can be represented with a non-zero lower bound on the integral in Equation 4.5 corresponding to the minimum energy. In addition, for perfectly conducting grains, there will be a contribution from 'image charges' (Draine & Sutin 1987) but we will not consider that here.

Sticking coefficients To evaluate the collisional charging rate the only remaining assumption required is for the sticking probabilities, S_X.

As with the freeze-out rate we will make the assumption that the sticking probability is 1 for all ions. However, in this case we also need a sticking probability for electrons which is more uncertain. Following Taylor et al. (1991) we will assume a value of $S_e = 0.5$.

4.1.3.2 Photoelectric charging

Taylor et al. (1991) specify the charging rate due to the photoelectric effect (the photoelectric current) as below, for spherical grains of radius a:

$$A^{pe} = \pi a^2 \int_{E_{\min}}^{E_{\max}} Q_{abs} F(h\nu) Y(h\nu)\, dE \tag{4.7}$$

where $E_{\min}$ is equal to E_{pe} when the grain is negatively charged, or $E_{pe} + eU_g$ when the grain is positively charged with potential U_g. E_{pe} is the energy below which photoemission from the grain is negligible. Like the yield, $Y(h\nu)$, and the absorption efficiency, Q_{abs}, the value of E_{pe} is an intrinsic property of the dust. The $F(h\nu)$ term in the expression above is the mean, angle-averaged ultraviolet intensity. The ultravi-

$Y_\infty = 0.5$,	$E_{pe} = 8\,\mathrm{eV}$	for polymeric or diamond-like carbon,
$Y_\infty = 0.05$,	$E_{pe} = 7\,\mathrm{eV}$	for graphitic carbon,

Table 4.1: Grain properties for two kinds of possible dust material. Y_∞ is the photoelectron yield for high photon energies, and E_{pe} is the cut-off energy for photoelectric emission to begin.

olet radiation field determines the value of $E_{\max}$, which in the interstellar medium we take to be 13.6 eV, the result of H_α absorption below 912Å.

Incident radiation Taylor et al. (1991) used the standard interstellar background UV field due to Draine (1978) and scaled the overall rate A^{pe} by a factor $e^{-2.5A_V}$ to account for attenuation with depth into a cloud. In the following sections we will retain the assumption of the Draine radiation field, but we will use values of $F(h\nu)$ calculated using the radiative transfer code of Chapter 2.

Yield function The yield, $Y(h\nu)$, is the average number of electrons ejected for each photon of energy $h\nu$ absorbed by the dust. The expression used by Taylor et al. (1991) was that of Draine (1978):

$$Y(h\nu) = Y_\infty(1 - E_{pe}/h\nu). \tag{4.8}$$

The values of Y_∞ and E_{pe} characterize the dust material. Taylor et al. (1991) adopted the values given in Table 4.1, which we too will use.

Absorption efficiency We will also make the assumption that $Q_{abs} = 1$. This is only valid for large grains ($a > 100$Å); for small grains more detailed knowledge of their composition is necessary.

4.1.3.3 Charge distribution

If we assume a single dust population (in size and composition), or at least that the population is separable into non-interacting parts, then, using the above, we can evaluate the steady-state charge distribution on grains of a given size and material.

The rate of positive charging for dust grains with electric charge i is given by I_i

below, while D_i is the corresponding rate of negative charging:

$$\begin{aligned} I_i &= A^{pe}(i) + \sum_{X:\ Z_X>0} Z_X A^c_X(i) S_X, \\ D_i &= \sum_{X:\ Z_X<0} (-Z_X) A^c_X(i) S_X. \end{aligned} \tag{4.9}$$

If the proportion of the dust grains with electric charge i is P_i, then the steady state obeys:

$$I_i \cdot P_i = D_{i+1} \cdot P_{i+1} \tag{4.10}$$

So the charge distribution for grains of a given size and composition can be calculated using the formulae above and the chemical abundances and UV intensities within the cloud.

4.1.3.4 Approximating the charge distribution

Since the grain charge affects the freeze-out rate of ions in the gas we need to know the charge in order to represent freeze-out in chemical models. However, keeping track of the actual proportions of grains with each charge level may be unnecessary. In Section 1.2.3 we used the assumption that all grains have charge -1 in order to calculate freeze-out rates. This assumption is appropriate when the majority of dust grains have this charge because the rest of the distribution can alter the freeze-out rates for ions by at most a factor of two.

In the rest of this chapter we will examine the charge distribution in a variety of interstellar clouds. Of particular interest is the question of how widely valid the uniform grain charge assumption is, and what alternative assumptions may be preferable?

4.2 Grain charge in one-dimensional clouds

Taylor et al. (1991) calculated the grain charge distribution within a plane-parallel, slab-shaped cloud with 5 mag of visual extinction (A_V) to the centre. Most models of interstellar dust material include a significant fraction in the form of solid carbon; the graphitic and diamond-like dust types mentioned in the previous section were used by Taylor et al. because they represent the two forms of amorphous carbon present in the grain model of Duley et al. (1989). The grain charge was calculated for grains of both types with 0.1 μm radius. The general behaviour of the charge distribution was similar for each, although the graphitic grains are much less positively charged due to their lower photoelectric yield. The underlying trend for the average (mean) grain charge was found to be positive at very low A_V with a slow drop towards a value close to -1 at $A_V = 5$. The proportion of grains with negative charge was greater than half below about 2.5 mag. Taylor et al. also found a sharp positive peak in the average charge—dominating the results for diamond—around $A_V = 1$. They accredited this to the peak in H^+ abundance at that A_V in their chemical model.

We will use the method of the previous section to re-examine the charge distribution of dust grains in the interstellar medium. Unlike Taylor et al. (1991) we can use the results of a radiative transfer calculation to estimate the photoelectric charging rates. We begin, therefore, by re-examining the conditions outlined above.

4.2.1 Comparison with Taylor et al. (1991)

We attempt to reproduce the conditions of Taylor et al. using a plane-parallel, slab-shaped cloud with the dust properties described in Section 3.2.1.1. The optical depth to the centre is 5 mag and the gas number density is 1000 cm^{-3} throughout. We model the chemistry with the reduced version of the UMIST database described in Section 3.3 and calculate the grain charge for the steady-state abundances.

The chemical model used by Taylor et al. (1991) used the exponential approximation for the photoreaction rates as well as for the photoelectric current from grains. The chemical abundances they obtained are, therefore, different to the abundances found for our model. Figure 4.1 shows the abundances in our model of the species used by Tay-

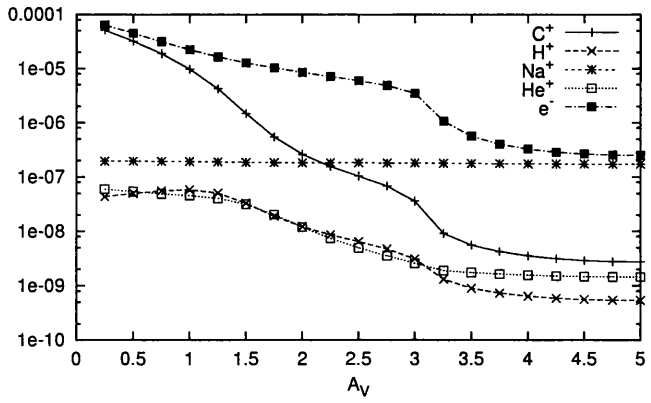

Figure 4.1: Fractional abundances in a slab-shaped cloud 10 mag thick. We measure A_V increasing into the cloud.

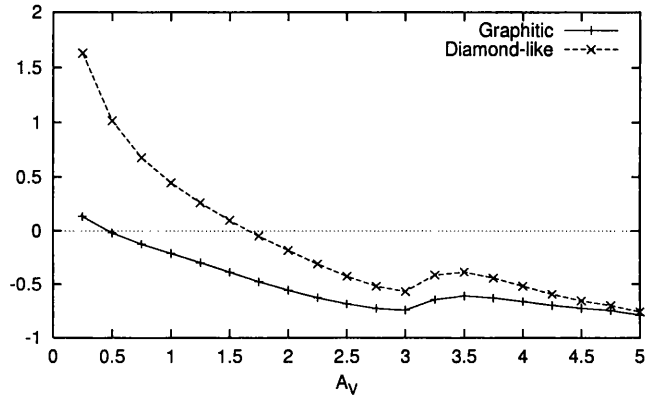

Figure 4.2: Average grain charge within a slab-shaped cloud 10 mag thick. We measure A_V increasing into the cloud.

lor et al., using Na^+ to represent their 'generic metal ion'. By comparison with the abundances of Taylor et al., the level of ions and electrons remains high slightly further into our cloud model than theirs. This is probably due to our use of a finite-depth cloud for the radiative transfer, rather than the semi-infinite slab to which the exponential approximation is suited.

More significantly, in our model C^+ remains the dominant ion throughout; H^+ is an order of magnitude less abundant than in the model of Taylor et al.. Hence we do not reproduce the sharp peak in the average grain charge at $A_V = 1$ which they obtain, and our charge is less positive overall. The variation of average grain charge with depth is shown in Figure 4.2.

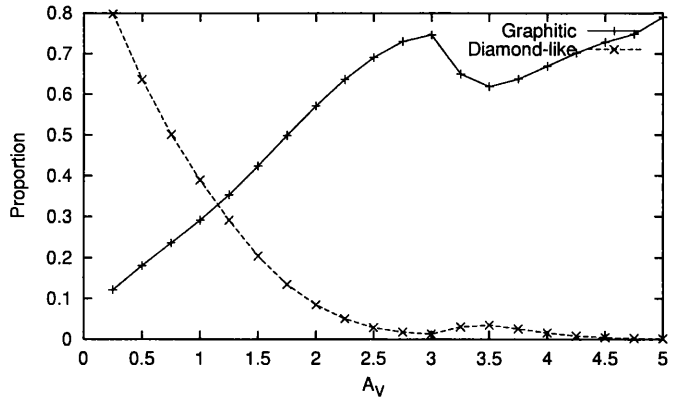

Figure 4.3: Proportion of time graphite grains spend negatively charged and the proportion of time diamond grains spend positively charged, within a plane-parallel cloud 10 mag thick. We measure A_V increasing into the cloud.

Just as in Taylor et al.'s model the two grains converge to a value close to -1 at high optical depth. (The two grains will always converge towards each other because the main difference between them is their photoelectric response which becomes less important with increasing depth.)

The proportion of time which grains spend with negative or positive charge is shown in Figure 4.3. The equivalent results from Taylor et al. were dominated by their positive peak at $A_V = 1$–2 which temporarily reversed the trends shown. In our models, however, the distributions progress more or less smoothly towards increasing proportion of negative charges with increasing depth.

Summary We do not reproduce the large positive peak of Taylor et al. (1991) but otherwise our results, obtained with the use of a radiative transfer calculation, largely follow theirs. More than half of the grains have negative charge below about $A_V = 2$ for either grain model.

4.2.2 Mean charge in spherical clouds

High optical depth Figure 4.4 shows the average grain charge at the chemical model points within the 10 mag diameter spherical cloud from the last chapter compared with the grain charge in the 10 mag thickness slab. The average grain charges for the points in the sphere do generally lie slightly above (more positive) the mean charge in the slab

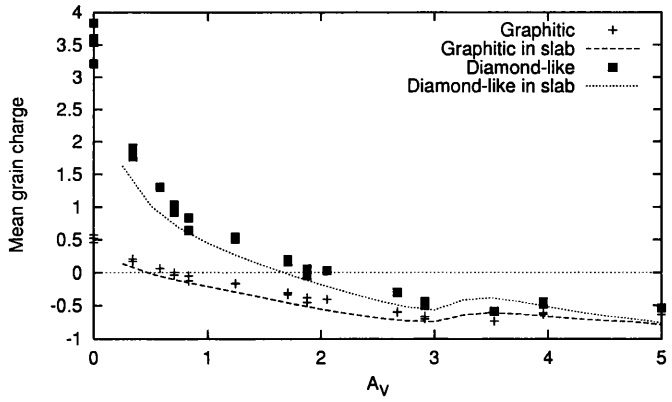

Figure 4.4: Average grain charge within a spherical cloud with 10 mag optical depth along a diameter. We measure A_V increasing into the cloud.

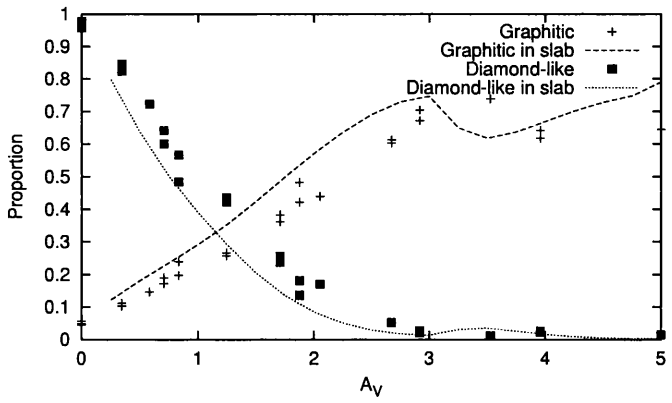

Figure 4.5: Proportion of time graphite grains spend negatively charged and proportion diamond grains spend positively charged, within a spherical and a slab-shaped cloud with 10 mag optical depth along a diameter. We measure A_V increasing into the cloud.

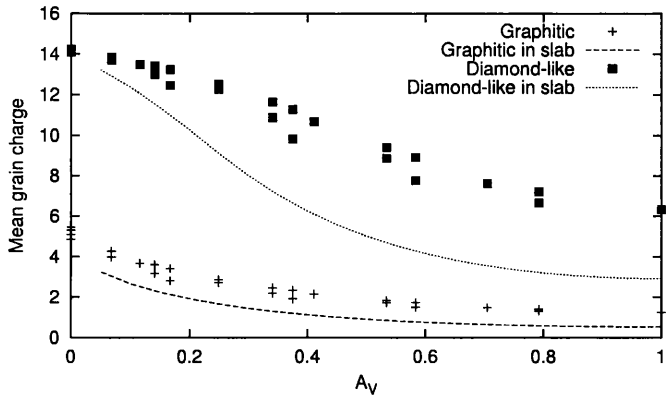

Figure 4.6: Average grain charge within a spherical cloud with 2 mag optical depth along the diameter. We measure A_V increasing into the cloud.

cloud. As seen in Figure 4.5, the diamond-like/graphitic grains also spend slightly more time positively/negatively charged in the sphere than in the slab. But the difference is small and the assumption of uniform charge (-1) appears valid over much the same region of the sphere as for the slab.

Low optical depth Since the grains at the edge of the 10 mag depth clouds tend to be positively charged, we expect to find only a low proportion of negative grains anywhere within clouds with low optical depth. Figure 4.6 displays the mean grain charge for a spherical cloud with 2 mag of visual extinction along the diameter. Both kinds of grain are highly positive throughout the cloud.

Even in the centre of this cloud ($A_V = 1$) the graphitic grain model still has less than 5% of grains with negative charge so we do not expect to be able to approximate the grain charge to -1 in such models. Figure 4.7 shows the proportion of dust grains with charge -1, 0 or $+1$ inside a 2 mag thick slab. The diamond-like grains, even at maximum depth, are largely positively charged. For such grains, at low temperatures, the best assumption we could make would be that positive ions do not freeze out. The neutral species will freeze out, of course, at their normal rate. The graphitic grains also have only a very small proportion with negative charge, but do have a significant fraction of neutral grains. Ions will freeze out onto the neutral grains at the same rate as other species, so in the graphitic case we might make the approximation that ions freeze out at a lower rate than neutral species according to the proportion of grains which are

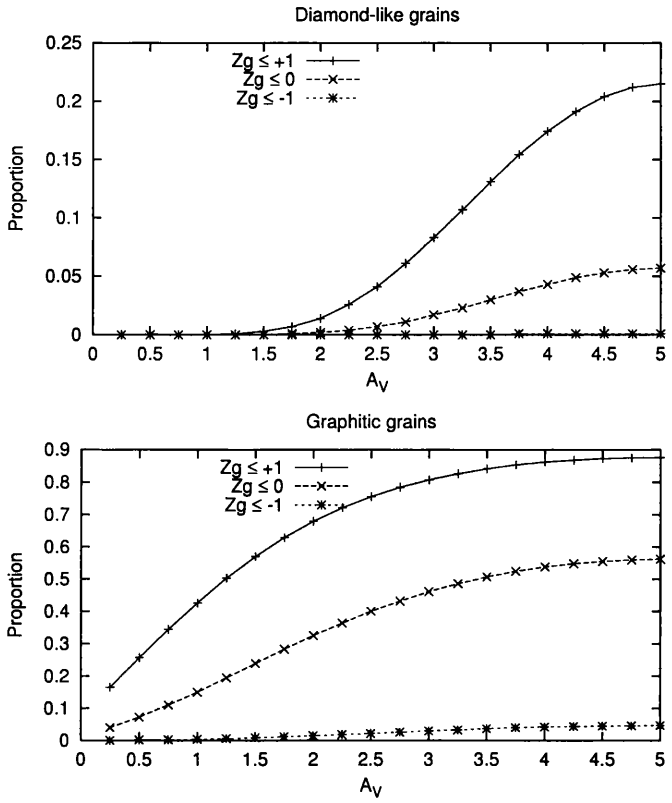

Figure 4.7: The proportion of dust grains with charges -1, 0 and $+1$ inside a slab-shaped cloud with total optical depth 2 mag. The upper plot is for diamond-like grains and the lower for graphitic.

neutral (50% at $A_V = 1$). Certainly, chemical models with freeze-out should not have an enhanced freeze-out rate for ions in low optical depth clouds.

4.3 Spheroidal clouds

From above, traditional dust grains inside low optical depth cloud models tend to have positive charges. However, in Chapter 3 we demonstrated a simple collapsing-cloud model in which the visual extinction in the central region was increased as a result of the cloud becoming flattened. We shall now consider the flattened sphere models of that chapter to see whether the collapse can have any significant effect on the grain charge.

For simplicity, we will not examine the two-dimensional variation in grain charge through the cloud, but concentrate on the variation with radius in the xy-plane of the clouds. The clouds collapse along the z-axis, their shape determined by $x^2 + y^2 + z^2/\zeta^2 = R^2$ with ζ changing from 1 to $1/2$ to $1/4$. The density of the clouds increases in proportion, changing the visual extinction in non-z-directions, so we cannot plot the variations against A_V for these clouds. The following graphs, therefore, use the dimensionless units of radius in which the edge of the cloud lies at $R = 4800$. In the spherical cases the visual extinction 0–4800 along the x-axis is equal to half the total optical depth along the z-axis, τ_z, which characterizes the families of flattened clouds that we use. We evaluate models with τ_z of 1, 2, 6 and 10 mag.

4.3.1 High optical depth

Figure 4.8 shows the average grain charge in the xy-plane of the high optical depth (10 mag along z-axis) flattened sphere models. The flattening, which increases the level of UV shielding within the cloud, does not greatly affect the average grain charge for this family of clouds. Indeed they seem to largely follow the behaviour of the slab and spherical clouds regarding the grain charges.

As shown in Figure 4.9, the majority of grains become negative around radius 2000 for diamond-like grains or 3300 for graphitic. In the spherical case these radii correspond to optical depths around 3 and 1.5 mag respectively. So the high extinction clouds of all shapes—slab, sphere and spheroid—can be treated equally well with the same grain-charge approximation.

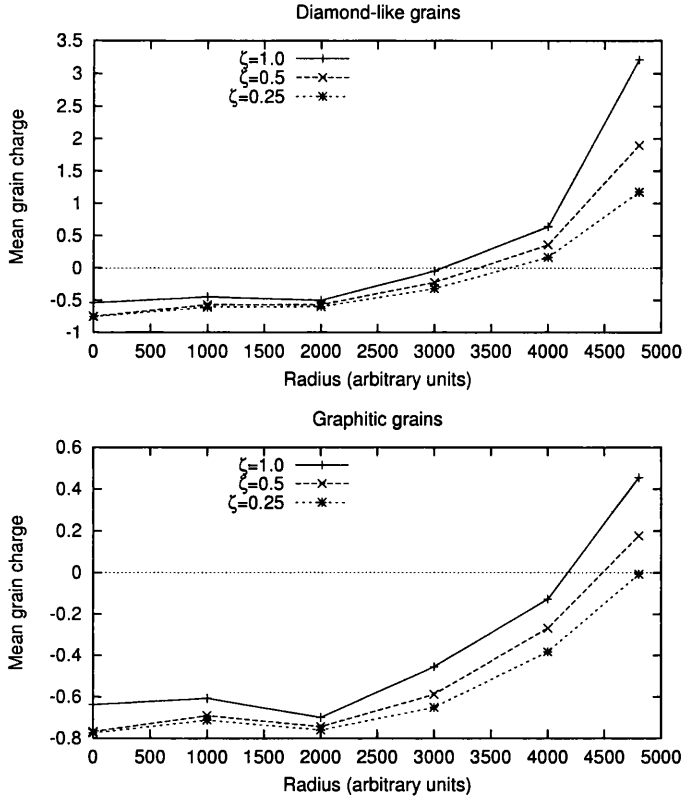

Figure 4.8: Average grain charge at points along the x-axis of spheroidal cloud models with total optical depth along z-axis of 10 mag. The upper plot is for diamond-like grain material, and the lower plot is for graphitic grain material. The clouds have shape $x^2 + z^2/\zeta^2 = 4800^2$.

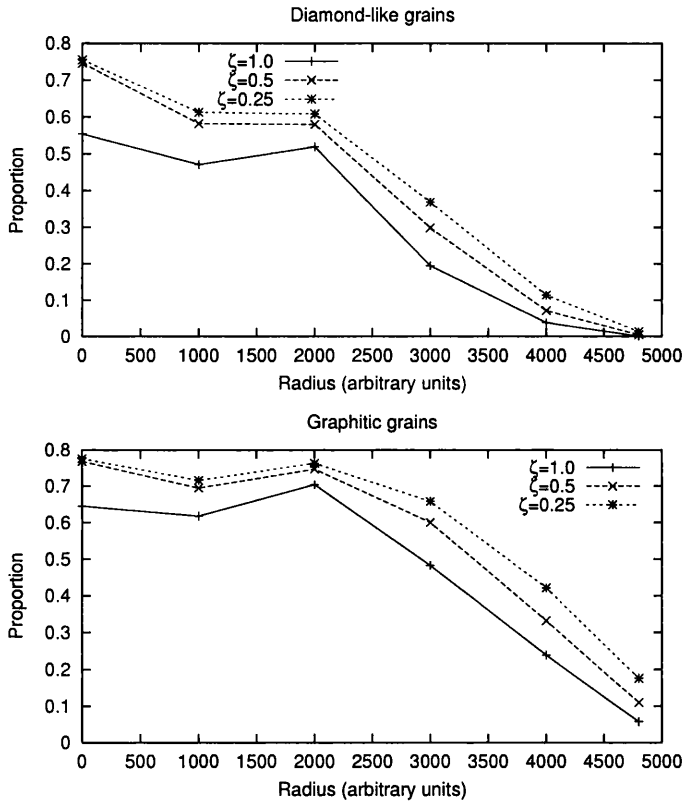

Figure 4.9: Proportion of diamond-like grains (upper) and proportion of graphitic grains (lower) which have charge -1. The values plotted are for the xy-plane inside a family of spheroidal clouds with 10 mag of extinction along the z-axis. The clouds have shape $x^2 + z^2/\zeta^2 = 4800^2$.

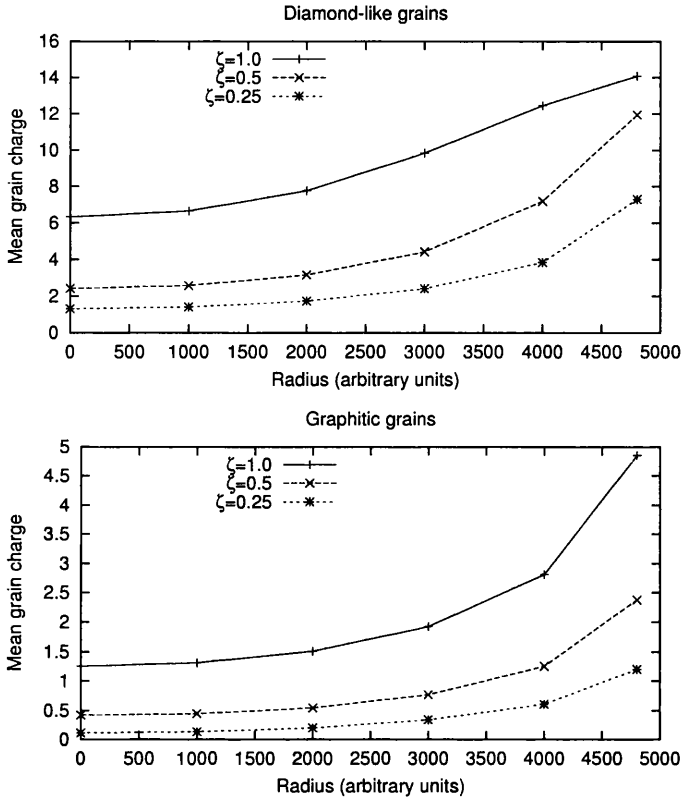

Figure 4.10: Average grain charge at points along the x-axis of spheroidal cloud models with total optical depth along z-axis of 2 mag. The upper plot is for diamond-like grain material, and the lower plot is for graphitic grain material. The xy-radius of the clouds is 4800.

4.3.2 Low optical depth

Figure 4.10 shows how the average grain charge in the central plane of a cloud with total optical depth along the z-axis of 2 mag changes with flattening. The effect on the mean charge is quite pronounced; from spherical to quarter-height ($\zeta = 0.25$) the mean charge drops by around a factor of three. However, the average grain charge is still always positive within these clouds. (Note that the mean is skewed in the outermost part of the clouds because we have arbitrarily truncated the charge distribution at $+15$.)

Figure 4.11 shows the mean charge inside thicker clouds with 6 mag of visual extinction along the z-axis. In this case, for the sphere the average charge drops to just below zero at the very centre of the cloud. The progressive flattening of the cloud then increases the size of the region within which the mean charge is less than zero.

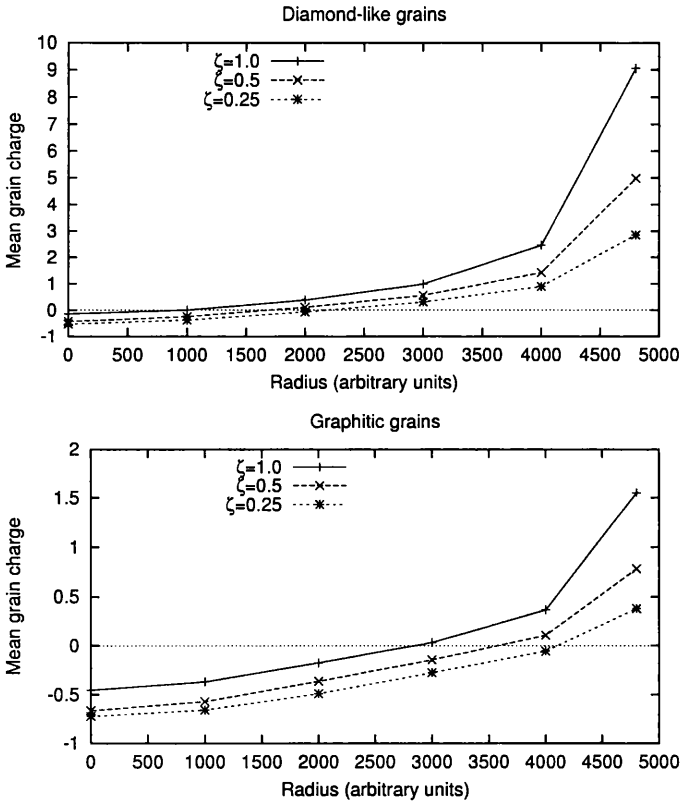

Figure 4.11: Average grain charge at points along the x-axis of spheroidal cloud models with total optical depth along z-axis of 6 mag. The upper plot is for diamond-like grain material, and the lower plot is for graphitic grain material. The xy-radius of the clouds is 4800.

For the purposes of approximating the grains with a single charge the proportion of grains with negative charge is more important than the average charge. It is also worth noting that grains with charge -1 make up the majority of all grains with negative charge. This is because the only means of negative charging for a grain is by collisions with electrons (negative ions are rare), and the probability of collision is greatly reduced for a negatively charged grain. In the terms of Section 4.1.3, D_{-1} is extremely small. Hence, in all our models the proportion of grains with charge -2 is at least six orders of magnitude less than the proportion with -1.

The proportion of grains that have charge -1 for the 6 mag cloud family is shown in Figure 4.12. For the diamond-like grains the proportion is generally small except in the very centre of the clouds. Even in the most highly flattened case, the negative grains only become dominant in the centre. However, due to the large enhancement in freeze-out rate for ions on negative grains, even 10% can be significant, and the flattening increases the size of the central region where negative grains need to be considered. For graphitic grains, the flattening produces a central region (to radius $\sim$ 2000) within which negatively charged grains are dominant.

Summary For the lowest optical depth clouds the degree of flattening we have examined is insufficient to significantly change the grain charge distribution for the purposes of our chemical models. However, when the initial depth to the centre is 3 mag, the flattening did make a difference. In the centre of our flattened sphere models, the approximation of grain charge by a uniform -1 becomes valid for graphitic grains. For diamond-like grains the proportion of negative grains becomes large enough to give ions some enhancement in freeze-out over the neutral species.

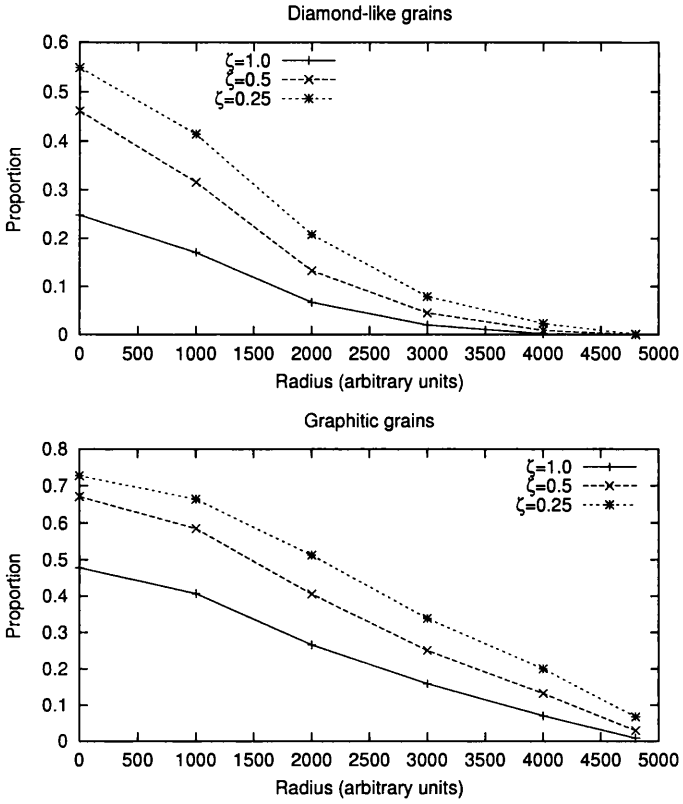

Figure 4.12: Proportion of diamond-like grains (upper) and proportion of graphitic grains (lower) which have charge -1. The values plotted are for the xy-plane inside a family of spheroidal clouds with 6 mag of extinction along the z-axis. The clouds have shape $x^2 + z^2/\zeta^2 = 4800^2$.

4.4 Conclusion

We have evaluated the charge distribution for dust grains inside the spheroidal cloud models of Chapter 3 with particular reference to the appropriate calculation of freeze-out rates. We used the full chemistry to evaluate collisional charging rates, and the radiation field obtained from a radiative transfer calculation to evaluate the photoelectric charging. The dust grains were modelled as large (0.1 μm) spheres of either graphitic or polymeric (diamond-like) carbon. These two grain types represent components present in many interstellar dust models.

The charge distributions we obtain for the high optical depth cloud models, A_V = 0–5 mag, indicate that, regardless of cloud shape, above optical depths around 2 mag the grain charge can be represented by a uniform value of -1 in Equations 1.7 and 1.8 used to evaluate freeze-out rate. This approximation breaks down above $A_V \approx 2$ as the proportion of grains with negative charge falls. However, for these thick clouds there remains a significant fraction of negative graphite grains even at $A_V = 0.25$, so ions may well still have slightly enhanced freeze-out rates. For the calculations of Section 1.2.3 the freeze-out of ions onto negative grains was enhanced by a factor of 17.71 over the neutrals so the proportion of negative grains would have to drop to less than five percent before ions achieved equality with neutral species.

For very low optical depth clouds, A_V = 0–1 mag, by contrast, the proportion of grains with negative charge is low throughout. We expect a very large degree of flattening would be required in order to change this. In such clouds the grains would be better represented as positive with some fraction of neutral grains in the graphitic case. Ions will therefore freeze out at a rate reduced from that of neutral species.

Intermediate depth clouds, A_V = 0–3 mag, represent the most complicated case. The outer regions of these clouds follow the behaviour of the thin clouds above, but the inner regions contain a significant fraction of negatively charged grains. Furthermore, a degree of compression of these clouds can radically affect the charge distribution in the central region, potentially equating them with the high optical depth clouds.

We conclude that the grain charge and hence freeze-out rate of ions in diffuse and translucent clouds is quite sensitive to the overall geometry of the cloud. If freeze out and surface reactions such as those examined in Section 1.2.3 are to be included in

non-slab shaped models then the grain charge distribution will need to be evaluated with regard to the particulars of the model.[1] The simple approximations for dark and bright clouds—all negative or all positive—may give freeze-out rates over an order of magnitude wrong for ions.

The situation, however, may be quite different for grains of significantly different size.

[1] We suggest that a simple, three-component (positive, negative & neutral) dust model introduced alongside the gas phase chemistry may suffice; though this will almost treble the number of freeze-out reactions required.

Bibliography

Caselli, P., Hasegawa, T. I. & Herbst, E. (1998), 'A proposed modification of the rate equations for reactions on grain surfaces', *Astrophys. J.* **495**, 309.

Cecchi-Pestellini, C. & Williams, D. A. (1998), 'Evolving interstellar extinction', *Mon. Not. Roy. Astron. Soc.* **296**, 414–418.

Draine, B. T. (1978), 'Photoelectric heating of interstellar gas.', *Astrophys. J. Sup.* **36**, 595–619.

Draine, B. T. & Sutin, B. (1987), 'Collisional charging of interstellar grains', *Astrophys. J.* **320**, 803–817.

Duley, W. W., Jone, A. P. & Williams, D. A. (1989), 'Hydrogenated amorphous carbon-coated silicate particles as a source of interstellar extinction', *Mon. Not. Roy. Astron. Soc.* **236**, 709.

Green, N. J. B., Toniazzo, T., Pilling, M. J., Ruffle, D. P., Bell, N. & Hartquist, T. W. (2001), 'A stochastic approach to grain surface chemical kinetics', *Astron. & Astrophys.* **375**, 1111.

Spitzer, L. (1978), *Physical Processes in the Interstellar Medium*, J. Wiley & Sons.

Taylor, S. D., Williams, D. A. & Bennett, A. (1991), 'Electric charge on grains in diffuse clouds', *Mon. Not. Roy. Astron. Soc.* **248**, 148–152.

Summary

In the first chapter we discussed the basic chemistry of the interstellar medium and its dependence on interstellar dust in particular.

With two simple models of processes in the interstellar medium we illustrated firstly by omission that processes on the surface of dust grains may be necessary to produce the levels of some species observed in the interstellar medium. Secondly we modelled the effects of some simple surface processes and showed that the results could improve matches with observational data. The efficiency of these processes is influenced by the electric charge present on dust grains because it affects the rate of freeze-out of ions.

The dust also affects the transfer of interstellar ultraviolet raditiation within the interstellar medium. At low visual extinctions this radiation is the major ionizing force, and provides a powerful mechanism for destruction of other molecules. Traditional chemical models, however, do not evaluate the intensity within the medium in an accurate manner. The lack of full treatment leads not only to inflexibility regarding new estimates of the interstellar background UV flux and the dust's optical properties, but also prevents the rate of photoreactions from varying in the correct manner.

In Chapter 2 we described a method for evaluating the UV intensity within two-dimensional models of the interstellar medium. The axisymmetric clouds which this method allows us to model are of interest because we expect the collapsing interstellar medium to have a favoured direction resulting from the presence of large-scale magnetic fields. We illustrated the difference between the simplest models of the interstellar medium: the slab and sphere; the sphere providing much less shielding from the interstellar UV.

We then demonstrated the potential of such a combined model of radiation and chemistry in the interstellar medium for exploring the dependence of gas phase abundances on the global properties of the medium. We used a set of spheroidal cloud models to represent clouds of various sizes at different stages of collapse.

The results of these simple models suggest that for thin clouds a very high degree of flattening may need to occur before it would affect the conditions inside the cloud enough to change the nature of the collapse. For thicker clouds the flattening mainly affects conditions in the outer regions, and the initial collapse would probably be quite different from the form modelled here.

There is a range of intermediate thickness clouds which show the potential for very complex behaviour even in these simple models. We suggest that slightly more realistic models may well provide an interesting means of placing limits on the interaction of parameters such as degree of collapse and ionization level within clouds.

The results also suggest that some species, such as CS can be very sensitive to the changing shape of interstellar clouds.

Finally, we examine the electric charge on the dust in the non-slab shaped clouds which this method enables modelling of. We re-evaluate the charge on the large, classical grains which we previously assumed may be responsible for chemical reactions supplementing the gas phase. There is a clear difference between the high optical depth cases and low optical depth, each of which can be modelled relatively easily. In between, our models indicated that the grain charge can also be sensitive to the shape of the cloud. Thus if surface reactions are to be included in chemical models of collapsing clouds they too will have an additional dependence on the stage of collapse, which surely increases the likelihood that chemical models may one day provide good tracers for collapse in the interstellar medium.

Appendix A

Using the RTc code

This is a brief guide to using the RTc code for calculating the UV radiation field inside an axisymmetric cloud. The intention of this guide is not to give a detailed technical description: the best way to utilize the software is to develop one of the existing implementations. Rather, this provides some additional information and guidelines which are not obvious from either the description of the method from Chapter 2 or the code itself.

A.1 Overview

The basic requirements for using the RTc code are as follows:

1. A description of the cloud (§A.2) such that the dust properties can be determined at any wavelength and position.

2. Grids of shells and angles (§A.3) detailed enough to sample the structure of the cloud.

3. Sufficient disk space to store the temporary 'list' files (§A.4.1) created during the calculation. One of these may be reused from a previous run if available.

A.1.1 Units of measurement

The code works in arbitrary units of both intensity and distance. The code appears to behave better numerically if the incident intensity value is less than one. The intensity can be scaled to the correct values after the calculation is complete.

Some idea of the relation of RTc-distance to physical distance may be helpful when setting up the calculation: particularly the requirements of Sections A.2 and A.3.2 (See also Section 3.1.2.1).

A.2 The cloud module

The first step is to create a description of the cloud for the purposes of radiative transfer in the `rt_cloud` module. This requires specification of the extinction and scattering coefficients and the phase function parameter for any point in the cloud. The incident intensity from outside the cloud is also specified in this module.

The cloud is described mainly by means of the `cloud_properties` function which returns the value of the parameters at a specified point and wavelength. In addition to the physical parameters, the code also needs a 'scale length' value which describes the size of the region around the specified point within which the dust parameters are approximately constant.

The position inside the cloud is described in general three-dimensional terms by Cartesian coordinates x, y and z. The symmetry of the cloud assumed by the code requires that the cloud properties depend on the cylindrical radius, $\sqrt{x^2 + y^2}$, rather than on the particular values of x or y, and that the properties are the same for $z = a$ and $z = -a$.

Any initialization code required should be placed in `init_cloud`, with clean-up in `done_cloud`.

A.2.1 Density

Both the extinction coefficient and scattering coefficient depend on the density of the dust. The easiest way to represent this may be by calculating the cloud density based on the position requested. The density is then multiplied by the dust cross-section

to find the extinction coefficient or by the cross-section and albedo for the scattering coefficient.

A.2.2 Dust cross-section and albedo

The dust cross-section and albedo are the density-independent parameters of the dust. Unless a different dust model is used in different regions of the cloud these values will depend only on wavelength and not position.

The cross-section describes the likelihood of interception of a photon by a dust grain. However, the cross-section should be an average value representing the whole grain population. Furthermore it is wavelength dependent and may be defined relative to the visual by means of the interstellar extinction curve.

The dust albedo (0–1) is the proportion of intercepted photons which are re-emitted (i.e., ratio of scattered to absorbed). This is also wavelength dependent.

A.2.3 Scale length

The scale length describes the minimum distance in the cloud over which the extinction parameter is approximately unchanged. It can therefore be defined by reference to the first derivative of the density or the mean path length for photons. However, this is a very time-critical routine for the method so a complicated calculation is inappropriate: a small constant value would probably be more useful. The two features that the scale length must have are: (1) Be smaller than the distance to the edge of the cloud or, perhaps, another region in which a different dust model applies—except under the next condition. (2) Not become arbitrarily small; there must be some minimum value for the scale length, otherwise the optical depth calculation may not terminate.

For homogeneous clouds the scale length can be defined entirely by reference to the cloud edge, with a minimum cut-off.

A.2.4 Phase function and parameter

The code is currently set up to use the Henyey-Greenstein phase function to determine the likelihood of photons being scattered by a particular angle. The phase function

is modified by a single parameter, g, describing the preferred direction of scattering (forward or backwards).

The value of g, the mean scattering angle cosine, is an intrinsic property of the dust and varies with wavelength. If a different phase function is required then the `phase` function in the `rt_phase.f90` module should be replaced. However, if the phase function needs to vary with position, or have more than one parameter, then they will need to be encoded into the value of g somehow or require the code to be rewritten.

A.3 Shell and Angle grids

The positions within the cloud at which the radiation intensity is evaluated, and the directions of specific intensities and integration points along lines of sight are defined in the shell and angle grids. These grid specifications should each be identified by unique two-character identifiers.

A.3.1 Angle grids

The angle grid defines the directions in which the specific intensity is calculated at each point. The directions are listed as a number of psi-values (0–2) at each theta value (0–0.5). The specified values are multiplied by π to obtain the angles in radians. The theta values represent the angle down from the positive z-direction, and angles less than $\pi/2$ (horizontal) are duplicated between $\pi/2$ and π. The psi-values represent the angles from the x-axis in the $\theta = \pi/2$ plane

The set of (θ, ψ) directions should be distributed evenly around the sphere (0–π,0–2π). The total number of directions determines the accuracy of the mean angle-averaged intensity received from unscattered light. For this purpose the directions only need to be numerous enough such that the resulting lines of sight from each point explore any major features of the density structure. However, for highly forward or backward scattering dust the density of directions over the sphere will also affect the accuracy of the scattering calculation. The runtime required for a calculation is approximately linear in the total number of directions used.

A.3.2 Shell grids

The shell grid used by the code defines the x and z-coordinates which are used to determine either points at which the intensity is calculated —the *essential* shells—or integration points along lines of sight—*inessential* shells. Shell lists are specified separately for cylindrical radii (R-shells) and height (Z-shells). The general intention in deciding the spacing for the shells should be to have a higher density of shells in regions of the cloud where the dust properties change most rapidly. For homogeneous clouds, or other clouds whose density does not decrease gradually, the edge region needs particular attention. Indeed, better accuracy would be expected for more smoothly varying clouds.

In addition, the following rules should be observed:

1. For both Z and R-shells the innermost shell must be at $z = 0$ or $x^2 + y^2 = 0$ and must be essential.

2. The outermost Z-shell must be essential and lie beyond the edge of the cloud, where there is no dust.

3. The previous rule also applies for the outermost R-shell, except that if there is only a single R-shell at $x^2 + y^2 = 0$ then a one-dimensional calculation is performed as for a slab-shaped cloud. (In which case the cloud module should return properties depending only on the z-coordinate.)

4. Because the innermost R-shell is merely the z-axis it will be intersected by only a few lines of sight. The gap between the central R-shell and the next smallest essential R-shell should therefore be smaller than between other essential R-shells. (All other things being equal, the first off-centre R-shell should have radius less than a third of the radius of the next.)

The run-time required for a calculation varies approximately in proportion to

$$(N_R^e N_Z + N_Z^e N_R) \times \max(N_R, N_Z), \tag{A.1}$$

where $N_{R/Z}^e$ is the number of essential R/Z-shells and $N_{R/Z}$ is the total number of R/Z-shells. To simplify, if the R and Z-shells are specified identical and there are N

essential shells of each kind, with n inessential shells between each pair of essential shells then the run-time is $O(n^2N^3)$.

A.4 Files generated at run-time

A.4.1 Calculation data: Q and T-lists

The RTc code generates two large files during a calculation. These files, called the 'Q' and 'T-list' contain the geometric and dust information for the lines of sight used in the calculation.

The contents of the Q-list depend only on the shell and angle grids used so this file can be retained between calculations. The code attempts to re-use a Q-list file which is based on the grids currently in use. If the Q-list was only partly generated due to an incomplete previous run, or if either the angle or the shell grid has changed but kept the same identifier then this use will fail or be incorrect.

The contents of the T-list, however, depend on the particular cloud model in use and are wavelength specific so this file is regenerated during the initialization of each calculation.

The disk space available for these files provides the main limitation—other than run-time—on the size of shell and angle grids that can be used. If the code is to be used on a machine with a large quantity of RAM then the code could easily be modified to store these lists in memory. A significant speed increase might be achieved from holding the T-list in memory. At the least, the T-list should be stored on the disk with fastest access time possible for the machine making the calculation.

A.4.2 Status information: the log file

In addition, the code also writes a stream of information describing the progress of the calculation to the 'log-file'. The file should be attached to the unit of `log_U` from the `rt_base` module before any other part of the code is used. However, standard output can usually be safely used.

Error messages are written to the log-file prefixed with an exclamation mark or asterisk. Messages indicating a possible error in the code are prefixed with a question

mark.

A.5 Making a calculation

The radiation field within the cloud is calculated using the `calculate_field` routine from the `rt_calc` module, specifying the maximum number of scatters (≥ 0) to include and the name of the file to use for the T-list. That routine also requires a `wronk_intensities` type structure in which to store the field; the structure must be allocated beforehand with the `allocate_field` routine from the `rt_field` module and have the desired wavelength specified. The `rt_field` module provides the routines `store_intensities` and `load_intensities` to write or read these structures to or from files for use following calculation.

Before anything from the `rt_field` module can be used it must be initialized with the names of the shell and angle grid files using the `init_field` routine. Once that module is initialized the `rt_calc` module must similarly be initialized using `init_calc`.

The code will calculate the field after the specified number of scatterings have occurred unless the difference between consecutive iterations falls below a certain limit. This limit is defined in the `rt_field` module by the `min_field_diff` variable, set to 10^{-10} by default. When the infinity norm of the difference between sets of specific intensities for consecutive iterations (i.e., the biggest difference in specific intensity from one scattering) is less than the value of `min_field_diff` the calculation terminates. The cut-off may be set to another value after `init_field` has been called.

Finally, before a calculation can be carried out the `rt_cloud` module must be initialized with `init_cloud`. The parameters required for this initialization depend on the particulars of the cloud model that has been defined. In the case of the spheroidal models, for example, the cloud is parameterized by the optical depth to the centre and the ellipticity of the cross-section. When the calculation is complete for the cloud the module should be terminated by calling the `done_cloud` routine. A new cloud can then be analysed.

Similarly the `rt_calc` and `rt_field` modules should be terminated by calling

the `done_calc` and `done_field` routines when no longer required.

Some other program can then be used to transform the calculation results into the format required by the chemical model in use.

Acknowledgements

I am grateful for the receipt of a postgraduate research studentship from PPARC which funded this PhD.

In addition, I would like to thank all the people who have offered me help, encouragement or chocolate during the last few years.

For practical help in particular, I would like to thank: the referees on the papers presented in Chapter 1; Andreas Efstathiou and Stefano Tiné for assistance regarding radiative transfer; and Jeremy Yates for conversations about radiation and its relation to the chemistry, and also for answers to stupid questions. I owe some thanks also to Jonathan Rawlings for somehow always being illuminating. And especially to my supervisor, David Williams, for explanations, justifications, motivations, trying to prevent me starting a sentence with a conjunction, and for his great patience in the face of spiralling incompetence.